Control of ferroelectric domains in epitaxial BiFeO$_3$ thin films and submicron structures

Dissertation

zur Erlangung des
Doktorgrades der Naturwissenschaften (Dr. rer. nat.)

der Naturwissenschaftlichen Fakultät II − Chemie und Physik

der Martin-Luther-Universität Halle Wittenberg

vorgelegt

von Herrn Dipl.-Phys. Florian Johann

geboren am 21.12.1982 in Kirchheimbolanden

Gutachter/in:

1. Prof. Dr. Dietrich Hesse
2. Prof. Dr. Kathrin Dörr
3. Prof. Dr. J. Marty Gregg

Halle (Saale), Oktober 2012   verteidigt am 22. Mai 2013

Contents

List of Figures

List of Tables

List of Abbreviations

α_{c}	Pseudocubic angle
α_{rh}	Rhombohedral angle
ϵ	Strain
λ	Wavelength
ν	Poisson's ratio
ρ	Resistivity
σ	Mechanical stress
$\Theta, \omega, \phi, \Psi$	Angles for X-ray diffraction measurements
A	Area
a	In-plane lattice constant
$a_{\mathrm{c}}, b_{\mathrm{c}}, c_{\mathrm{c}}$	(Pseudo)cubic lattice constants
$a_{\mathrm{o}}, b_{\mathrm{o}}, c_{\mathrm{o}}$	Orthorhombic lattice constants
a_{rh}	Rhombohedral lattice constant
A_{eff}	Effective area
C	Capacitance
c	Out-of-plane lattice constant
d	Electrode separation
d	Etch depth
d	Inter-plane spacing
d	Piezoelectric tensor

E	Electric field
f	Frequency
F_e	Elastic energy
F_w	Domain wall energy
F_b	Force performing a buckling of cantilever
F_d	Depolarization energy
F_n	Force performing a normal deflection of cantilever
F_t	Force performing a torsion of cantilever
G	Shear modulus
H	Magnetic field
h	Film thickness
I	Current
I	Power density
l	Length of electrode
M	Magnetization
m	Misfit
P	Polarization
p	Pyroelectric coefficient
$P^{\pm}_{1,\dots,4}$	Polarization variants of BFO
P_S	Spontaneous polarization
P_net	Net polarization
Q	Charge
r	Etch rate
$r_{1,\dots,4}$	Structural variants of BFO
T	Temperature
t	Time
T_C	Curie temperature
T_N	Néel temperature
V	Voltage

x

V	Volume
$V_{\mathrm{C}}^{\pm}$	Positive and negative coercive voltage
V_{ac}	Alternating voltage
x_{ij}	Strain
AFM	Atomic force microscopy
BFO	Bismuth ferrite ($BiFeO_3$)
BTO	Barium titanate ($BaTiO_3$)
DSO	Dysprosium scandate ($DyScO_3$)
FIB	Focused ion beam
GSO	Gadolinium scandate ($GdScO_3$)
HF	Hydrofluoric acid
HRTEM	High resolution transmission electron microscopy
KAI	Kolmogorov-Avrami-Ishibashi
LPFM	Lateral piezoresponse force microscopy
LSMO	Lanthanum strontium manganite ($La_{0.7}Sr_{0.3}MnO_3$)
PFM	Piezoresponse force microscopy
PLD	Pulsed laser deposition
RE	Rare-earth
RSM	Reciprocal space map
SEM	Scanning electron microscopy
SRO	Strontium ruthenate ($SrRuO_3$)
SSO	Samarium scandate ($SmScO_3$)
STEM	Scanning transmission electron microscopy
STO	Strontium titanate ($SrTiO_3$)
TEM	Transmission electron microscopy
VPFM	Vertical piezoresponse force microscopy
XRD	X-ray diffraction

1

Introduction

Multiferroics, materials which posses more than one ferroic order parameter, have been intensively studied in the last decades [1, 2]. In particular, multiferroic materials which exhibit simultaneous electric and magnetic order are of interest, because not only they combine the two properties in one material, but they also may have additional functionalities due to a coupling between these order parameters, such as a magnetoelectric effect [3,4]. At room temperature, however, not many single phase multiferroic materials exist, which is a consequence of competing electronic properties [5]. One exception is bismuth ferrite, $BiFeO_3$ (BFO), which is a strong ferroelectric material with antiferromagnetic order at room temperature. Hence, it has been in the focus of many studies and it is till today subject of many investigations [6]. BFO has a rhombohedral symmetry which allows to form a total of four different ferroelastic domains and eight different ferroelectric domains in thin films. Naturally, many different complex domain patterns can form in thin BFO films, for instance so called 71° and 109° stripe domain patterns, which may be challenging to control.

Recently domain wall properties of multiferroics have moved into the focus of research [7–12]. It has been observed that domain walls and particular domain patterns can have properties of their own, dissimilar to the bulk domain properties [13]. The volume fraction of domain walls in thin films can reach a substantial amount, and the overall functional properties may therefore be dominated by the domain wall properties. Moreover, domain walls are in general mobile and can be manipulated for instance by an electric field. Thus, they may become promising for active memory devices [14,15].

In particular the 71° and 109° stripe domains of BFO have been studied intensively in the last years. A first report about novel functionalities at the domain walls was given by Seidel *et al.* [7, 8], showing that 109° and 180° domain walls are conductive, in contrast to the surrounding bulk domain. Although first the 71° domain walls of BFO were reported to be insulating by Seidel *et al.*, recently, conductivity was found in these domain walls for films grown with different growth parameters as well [9, 16]. In addition, it has been shown that the conductivity in the 109° domain walls exhibits a strong magnetoresistive effect [10]. A further peculiar effect is an above band gap photovoltaic effect featured by a particular 71° stripe domain pattern [11]. Above all, the reversal of a magnetization by an electric field, one of the early motivations to study multiferroics, has been demonstrated recently by Heron *et al.* [12] for the first time at room temperature with the help of a 71° stripe domain pattern of BFO.

In this thesis the formation of the ferroelectric domain patterns in epitaxial BFO thin films, the switching properties of the 71° stripe domains, and a new method for the fabrication of epitaxial submicron structures of BFO are shown. The detailed outline of the thesis is as follows.

In Chapter 2, first an introduction to ferroelectrics and multiferroics is given, followed by the materials used in this thesis and their properties. In particular the properties of BFO, the main material of investigation, will be presented.

Chapter 3 will describe the employed experimental techniques, such as the pulsed laser deposition method for film fabrication and the atomic force microscope with its special operation mode, piezoresponse force microscopy, for ferroelectric domain visualization.

In Chapter 4 the ferroelectric domain formation in the as-grown epitaxial BFO thin films on four different substrates ($SrTiO_3$, $DyScO_3$, $GdScO_3$ and $SmScO_3$) are discussed. It will be shown in which way the boundary conditions, e.g. the substrate symmetry, the applied epitaxial in-plane strain of the substrates or the substrate surface termination, influence the domain formation. With these boundary conditions the domain patterns can be controlled to a certain extend, which will be employed during the further investigations. In particular the formation of different 71° stripe domain patterns is presented.

Chapter 5 will focus on the ferroelectric switching properties and stability of these 71° stripe domain patterns of BFO upon repeated electrical switching. The ferroelectric polarization in the individual domains add up in these pattern to a net polarization, which has a component in the sample plane and a component out of the sample plane. Both components can be switched in two different configurations, though it will be shown that the behavior is very different.

In Chapter 6 the differential etch behavior of BFO will be addressed, which refers to different etch behaviors for its ferroelectric domains. It is shown that a high differential etch ratio exists in BFO, which can be employed to fabricate epitaxial submicron structures. Furthermore, a new effect with simultaneous light illumination while etching is presented, which allows further fabrication methods.

Finally, Chapter 7 will conclude with a summary of the results shown in this work and a brief outlook for further investigations.

Basics

2.1 Ferroelectrics

Ferroelectric crystals form a subgroup of the pyroelectric crystals, which are a subgroup of the piezoelectric crystals. In a piezoelectric crystal an applied mechanical stress σ generates an electric polarization P of the material. The components of the polarization vector and the applied mechanical stress tensor are linearly coupled by the piezoelectric third rank tensor d in the following way [17]

$$P_j = d_{jkl}\sigma_{kl} \tag{2.1}$$

Conversely, an externally applied electric field E causes a deformation ϵ of the crystal, called the converse piezolelectric effect. The relation between the strain tensor and the components of the electric field is given as

$$\epsilon_{ij} = d_{ijk}E_k \tag{2.2}$$

The first experimental proof of piezoelectricity was given by J. Curie and P. Curie in 1880 and 1881, respectively [18, 19]. From Neumann's law it follows that only 20 of the 32 existing crystal point groups can exhibit a piezoelectric effect [17]. The main exclusion criterion is that in all centrosymmetric crystals a piezoelectric effect is forbidden.

Pyroelectric materials have a spontaneous polarization, even without an applied mechanical stress or an applied electric field. Due to an isotropic change of temperature δT an anisotropic deformation of the unit cell is induced, resulting in a change of the spontaneous polarization P given by

$$P_i = p_i \delta T \tag{2.3}$$

where p_i are the components of the first rank pyroelectric tensor. Already in the 18th century Aepinus investigated a change of polarization of Tourmaline by changing the temperature [20]. Again, from symmetry arguments it follows, that only 10 point groups of the 20 piezoelectric point groups can show a pyroelectric effect [17].

Ferroelectrics have the additional property that their spontaneous polarization can be switched between two or more stable states by an externally applied electric field. Ferroelectricity was discovered in 1921 in Rochelle salt by Valasek [21], and got its name because of its similarities to ferromagnetism. The relationship between the polarization and the applied electric field has a hysteretic behavior, similar to the dependence of the
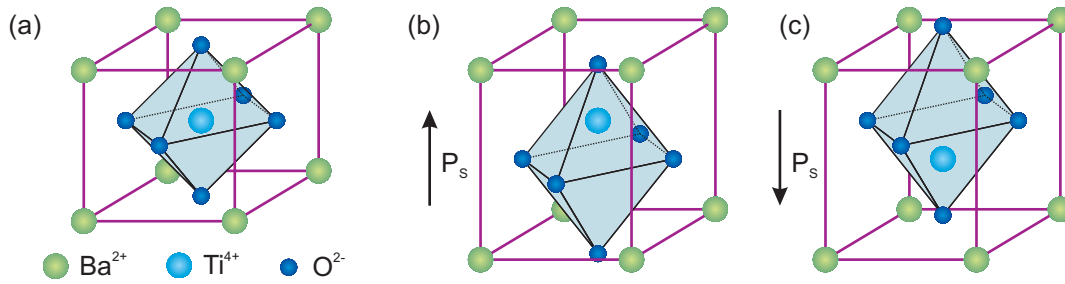
Figure 2.1: (a) Crystal structure of $BaTiO_3$ above its Curie temperature. In its tetragonal phase below the Curie temperature the oxygen octahedron and the titanium ion are shifted in opposite directions with respect to the barium ions, resulting in a spontaneous polariztion P_S pointing (b) upwards or (c) downwards, respectively.

magnetization on the magnetic field in ferromagnets (see Fig. 2.2(a) below). The number of possible polarization directions depends on the crystal symmetry and structure, but as well on the ferroelastic properties discussed later. For example, the trigonal crystal system of $LiNbO_3$ allows two stable ferroelectric states [22], whereas in the tetragonal $BaTiO_3$ (BTO) six different polarization directions are possible [23]. Continuous regions with the same direction of spontaneous polarization are called "domains". All ferroelectrics have a phase transition at their Curie temperature T_C, above which they become paraelectric. The phase transition is usually accompanied by a structural phase transition as well, most often to a cubic phase.

The microscopic origin of conventional ferroelectricity is a result of ion shifts within the unit cell, so that the center of negative and positive charges separate. In case of BTO this can be descriptively seen in the following way. BTO has a cubic perovskite structure in the paraelectric phase above its Curie temperature (Fig. 2.1(a)). It consists of Ba^{2+} ions at the corner of the cube and a Ti^{4+} ion in the middle. The Ti^{+4} ion is surrounded by O^{2-} ions, which sit on the cube face centers forming an octahedron. The center of positive charges as well as the center of negative charges fall in the center of the cubic unit cell.

Below the Curie temperature at 120°C the originally cubic perovskite structure of BTO becomes tetragonally distorted [23]. In addition, the oxygen ions and the titanium ion are shifted along the long axes of the tetrahedron, but in opposite directions with respect to the fixed barium ions [24]. Due to symmetry reasons there are two equivalent shift directions possible, which are displayed in Fig. 2.1(b) and 2.1(c) respectively. As a result of this shift, the centers of negative and positive charges do not coincide in the middle of the unit cell anymore, but they are separated by a certain distance d. The resulting dipole moment is the origin of the spontaneous polarization P_S. The spontaneous polarization P_S is defined to point from the negative center to the positive center of charges (see Fig. 2.1(b) and 2.1(c)). The shift of ions can be reversed by applying an electric field anti-parallel to the spontaneous polarization.

2.2 Multiferroics

A ferroic material is a generic term for a ferromagnetic, a ferroelectric or a ferroelastic material. All ferroic materials have in common that they have a long-range, spontaneous
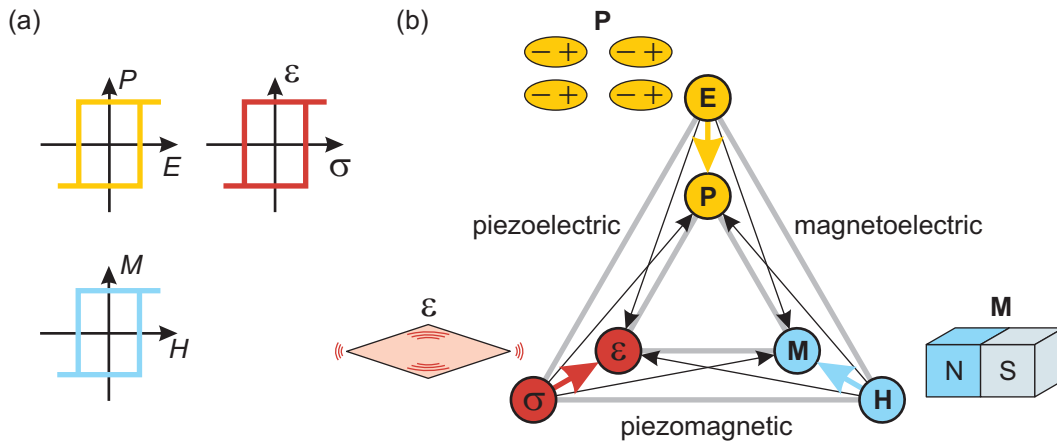
Figure 2.2: (a) Ferroics exhibit a hysteretic dependence of their order parameters on the corresponding external fields. For ferroelectrics the polarization P depends on the electric field E, for ferromagnets the magnetization M depends on applied magnetic field H and for ferroelastics the strain ϵ depends on the applied stress σ. (b) Diagram of the possible coupling between order parameters and external fields. Scheme is adapted from Ref. 4.

order parameter, which has hysteretic behavior with respect to its appropriate field (Fig. 2.2(a)). In case of ferromagnetics the magnetization M can be influenced by a magnetic field, for ferroelectrics (see Sec. 2.1) the spontaneous polarization P_S depends on the applied electric field E and for ferroelastics the spontaneous strain state ϵ can be changed by an applied stress σ. For vanishing external field, ferroic materials have at least two remanent states. Also, all ferroic materials have the property to form regions with the same direction of the order parameter, called "domains".

Originally, "multiferroics" were defined by H. Schmid as materials with a coexistence of at least two ferroic orders in a single phase [25]. In the recent years this definition has been broadened to include as well anti-ferroelectrics and anti-ferromagnets, and further, heterostructures built from different ferroic materials.

Multiferroics have attracted great interest because of their potential for new functionality. Figure 2.2(b) shows possible interactions which can principally be present in any material, not only in multiferroics. Any material responds with a polarization P to an externally applied electric field E, with a magnetization M to an externally applied magnetic field H and with a strain ϵ to an applied mechanical stress σ. However, particularly interesting interactions for applications are those which control one of the properties by a non-ordinary field. For instance can the polarization P in piezoelectric materials be influenced by an applied stress σ. The so-called "magneto-electric effect" controls either the magnetization by an electric field or the polarization by a magnetic field. Still to date, many researchers are looking for materials with a strong magneto-electric coupling, often by applying heterostructures [26–28]. This issue was as well the main motivation for the intense study of multiferroics. Although the magneto-electric effect can be present in non-multiferroic materials, e.g. in anti-ferromagnetic chromium oxide (Cr_2O_3) [29], high coupling constants are more likely to occur in multiferroic materials [1].

2.3 Materials employed in this work and their properties

In this section the materials used in the present thesis are introduced. First, the structural and functional properties of the main material of investigation, $BiFeO_3$ (BFO), are summarized in Sec. 2.3.1. In this thesis thin BFO films were grown on different substrates with a close lattice match to BFO. The structural properties of the employed substrates are presented in Sec. 2.3.2. And lastly, for electrical measurements conductive electrodes were deposited. Depending on the investigated configuration, first an epitaxial layer of strontium ruthenate, $SrRuO_3$ (SRO), was deposited on the substrate before the BFO film deposition. If needed, additional top electrodes were deposited onto the BFO film, consisting of amorphous SRO, gold, platinum, copper or epitaxial lanthanum strontium manganite, $La_{0.7}Sr_{0.3}MnO_3$ (LSMO). The structural properties of SRO and LSMO are discussed in Sec. 2.3.3.

2.3.1 Bismuth ferrite ($BiFeO_3$)

At room temperature BFO is a ferroelectric and antiferromagnetic material, therefore being one of the very few single-phase multiferroic materials at room temperature. First the structural properties are discussed, then the possible ferroelectric/ferroelstastic domain formations are explained.

2.3.1.1 Structural properties

BFO has a rather complex phase diagram as depicted in Fig. 2.3 for powdered bulk BFO. In the cubic γ-phase above 925°C, it has a pervoskite structure with Bi^{3+} ions at
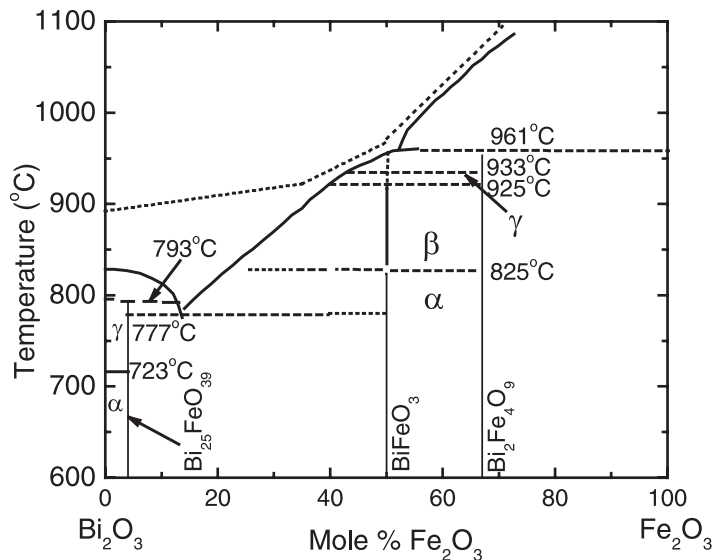
Figure 2.3: Phase diagram of the Bi_2O_3-Fe_2O_3 system obtained for powdered bulk material (Ref. [30]). The α-phase of BFO is the ferroelectric phase, whereas the β-phase and γ-phase are paraelectric phases.

the corner of the cube and one Fe^{3+} ion in the center which is surrounded by O^{2-} ions at the cube face centers forming an octahedron (Fig. 2.4(a)). Upon cooling down BFO
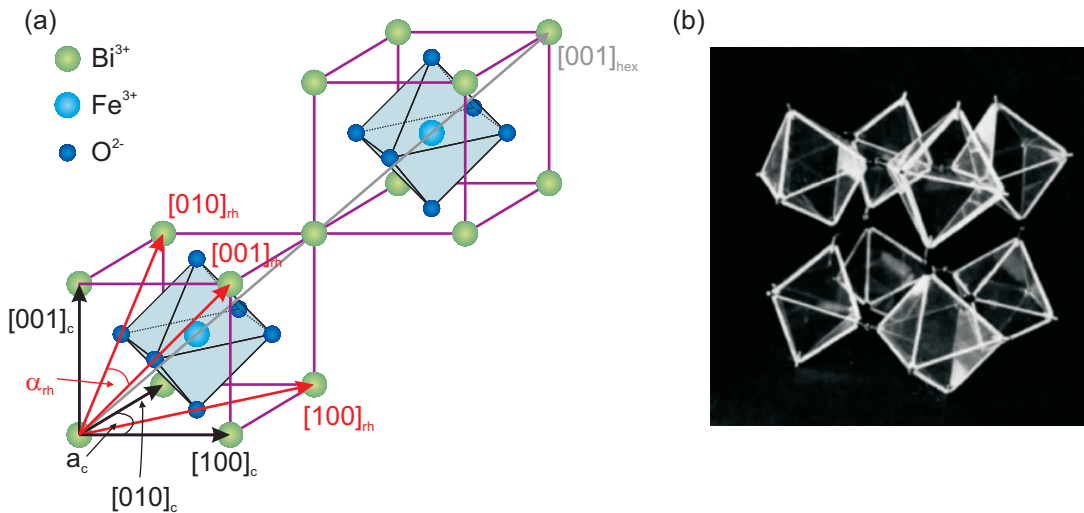
Figure 2.4: (a) Structure of BFO with rhombohedral unit vectors (index "rh") and pseudocubic unit vectors (index "c"). The rhombohedral unit cell incorporates two perovskite cubes along the $[111]_c$-axis to account for the full symmetry with oxygen octahedron rotations. For the rhombohedral unit cell there exists an equivalent hexagonal unit cell (index "hex"), where here just the third axis is shown. (b) $a^- a^- a^-$ oxygen octahedron rotations of four adjacent octahedrons in Glazer notation. Image taken from Ref. [31].

undergoes several phase transitions. At 925°C it has a structural phase transition to the orthorhombic β-phase, still being paraelectric. The paraelectric to ferroelectric phase transition occurs at $T_C \approx 825$°C and is accompanied by a structural phase transition. The so-called α-phase has a rhombohedral symmetry with space group $R3c$ [32] and it is the final structural phase below 825°C. The rhombohedral symmetry evolves from the ideal perovskite structure by a distortion in the following way (Fig. 2.4(a)): (1) The perfectly cubic perovskite is stretched along the pseudocubic $[111]_c$-direction, resulting in the rhombohedral symmetry. (2) The oxygen octahedrons are rotated around each cubic axis by the same angle α. However, along each cubic axis the rotation is in opposite directions for two adjacent cubes. Figure 2.4(b) shows the resulting rotations, which are called an $a^- a^- a^-$ oxygen octahedron rotation in the Glazer notation [31]. In addition, the oxygen octahedron is slightly distorted [33]. (3) The Fe^{3+} and Bi^{3+} ions are shifted along the $[111]_c$-direction with respect to the O^{2-} ions as depicted in Fig. 2.5 [33].

Due to the oxygen octahedron rotations the complete unit cell has to incorporate two pseudocubes (Fig. 2.4(a)). At room temperature the rhombohedral unit cell lattice parameters were determined from a monodomain single crystal as $a_{rh} = 5.6343$ Å and $\alpha_{rh} = 59.348$°, with an oxygen octahedron rotation of $\pm\alpha = 13.8$° around the $[111]_c$-axis [33]. The ion shifts were determined to be 0.13 Å and 0.54 Å along the $[111]_c$ axis for Fe^{3+} and Bi^{3+} respectively (see Fig. 2.5). Often the oxygen octahedron rotations are neglected and just one distorted perovskite cube is considered. In this pseudocubic notation the lattice constants are given as $a_c = 3.965$ Å and $\alpha_c = 89.45$°.

2.3.1.2 Ferroelectricity in bismuth ferrite

The ferroelectricity in BFO is mainly driven by the Bi^{3+} ion [34]. The Bi^{3+} ion has a stereochemically active $6s^2$ lone-pair allowing for a hybridization of the 6p orbital with
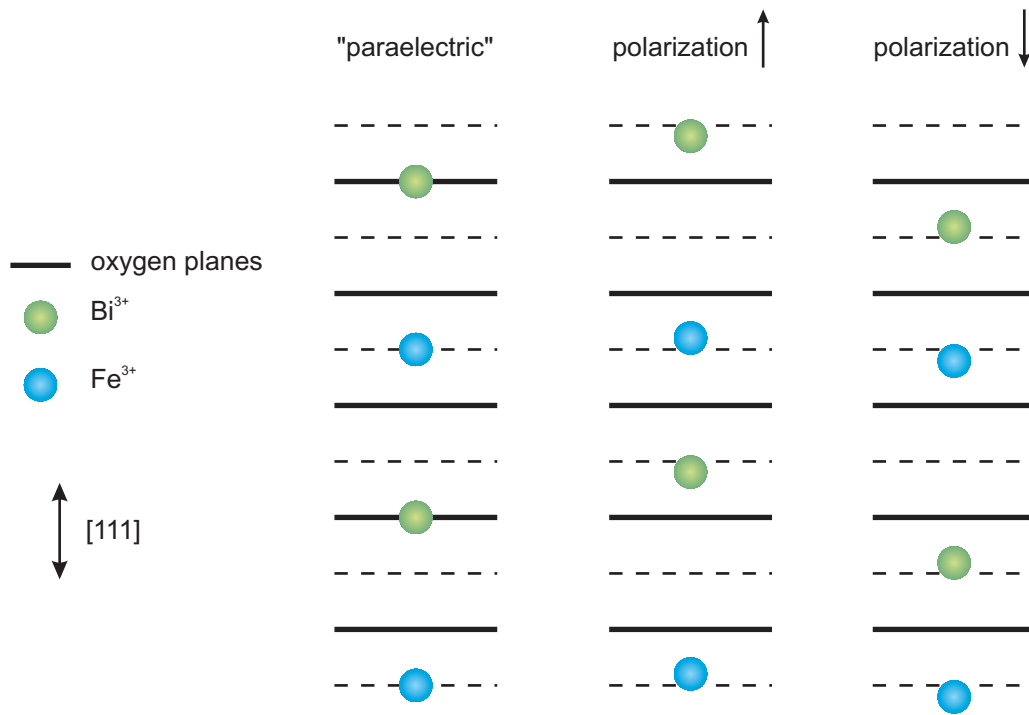
Figure 2.5: Viewing BFO with the $[111]_c$-axis in vertical alignment. The oxygen ions form planes perpendicular to the $(111)_c$-direction, separated by $1.33\,\text{Å}$. In the paraelectric phase the Bi^{3+} ion lies within such oxygen planes, whereas the Fe^{3+} ion is placed right in the middle between two planes (dashed lines). In the ferroelectric phase at room temperature the Fe^{3+} ions and Bi^{3+} ions are shifted by $0.13\,\text{Å}$ and $0.54\,\text{Å}$ along the $[111]_c$-direction [33], resulting in a ferroelectric polarization. Upon inversion of the polarization, the Bi^{3+} ion will move trough a plane of oxygen. All shifts are drawn true to scale with respect to the oxygen plane spacing.

the O 2p orbitals [35]. This drives the Bi^{3+} off-center and closer to the O^{2-} ion, leading ultimately to ferroelectricity.

Figure 2.5 depicts the resulting shifts of the Fe^{3+} and Bi^{3+} ions in the ferroelectric phase at room temperature. The value of the spontaneous polarization along the $[111]_c$-axis has been reported to be approximately $100\,\mu\text{C/cm}^2$ in thin films [36], single crystals [37] and ceramics [38], and is in agreement with theoretical calculations [34]. In projection along the often considered $[001]_c$-axes the polarization value amounts to $60\,\mu\text{C/cm}^2$.

In ferroelectric thin films the value of the polarization can often be strongly influenced by the epitaxial strain. For instance, the polarization of BTO can be significantly improved upon compressively straining the film [39]. For BFO the polarization along the $[111]_c$ axis is almost independent of the applied strain, which has been shown experimentally [40–42] and calculated theoretically [43].

2.3.1.3 Magnetism in bismuth ferrite

Below its Néel temperature $T_N = 370\,^\circ\text{C}$ BFO is an antiferromagnetic material [44]. The phase transition is not accompanied by a structural phase transition, however, an abrupt change in the thermal expansion coefficients at the phase transition has been reported for thin films [45]. The magnetism is driven by the Fe^{3+} ions in a G-type antiferromagnetic ordering, referring to a parallel alignment of the Fe^{3+} ions within one $(111)_c$ plane and an
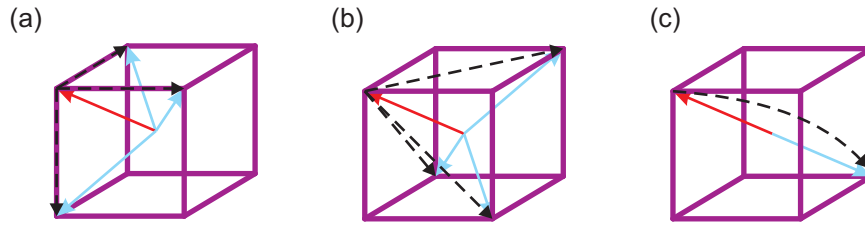
Figure 2.6: From an initial direction, depicted in a pseudocubic unit cell in red, the polarization can be switching to one of the seven remaining $\langle 111 \rangle_c$-directions, depicted in blue. For (a) 71°-switching and (b) 109°-switching three possible switching processes exist, whereas for (c) 180°-switching only one possibility exists.

anti-parallel alignment for two adjacent $(111)_c$ planes [44]. The spin alignment is in fact not perfectly antiparallel, but a small canted moment exists. The origin of this canting is the ferroelectricity which breaks the inversion symmetry and leads in this way to a magnetoelectric coupling [46]. The canted moment, however, rotates spatially, forming an incommensurate spin cycloid with a propagation along the $[110]_c$-axis and wavelength of approximately 63 nm [47]. Nevertheless, the canted moment has an easy plane of magnetization which is coupled to the ferroelectric polarization.

2.3.1.4 Switching of the order parameters

The direction of the ferroelectric polarization in BFO can be switched by an electric field. The rhombohedral distortion of BFO is weak enough, that from the initial direction the polarization can be changed to potentially seven new directions, namely to one of the seven remaining equivalent $\langle 111 \rangle_c$-directions. The possible switching processes are named after the angle between the old and new direction of polarization. Hence, three different types of switching are possible: 71°-switching (Fig. 2.6(a)), 109°-switching (Fig. 2.6(b)) and 180°-switching (Fig. 2.6(c)). Due to the multitude of possible switching directions a complete control of which switching occurs is difficult to realize [48].

Since the direction of the polarization and the rhombohedral distortion are coupled, a ferroelectric switching will result in ferroelastic switching for 71°-switching and 109°-switching as well. In addition, the antiferromagnetic planes, and therefore the magnetic easy plane of the canted moment, are rotated for these types of switching, because of their coupling to the ferroelectricity and unit cell distortion. In this respect, BFO exhibits a magnetoelectric coupling, which has been shown experimentally [49]. In case of 180°-switching the rhombohedral distortion remains unchanged, since for a complete inversion the rhombohedral symmetry is invariant. Also, the magnetic properties remain unchanged.

On the other hand, a switching of the magnetic order via a magnetic field is impractical, because of BFO's antiferromagnetic ordering with just a small canted moment, which is in addition coupled to the strong ferroelectricity.

2.3.1.5 Domains and domain walls in bismuth ferrite

As for all ferroic materials, BFO thin films, ceramics or single crystals form domains, i.e. regions with the same direction of the order parameter. Here, only the case of $(001)_c$-

oriented thin films is considered in detail. The slightly rhombohedrally distorted BFO unit cell can have four orientations with respect to a cubic substrate, which are named r_1 to r_4 and are shown in Fig. 2.7(a). For each ferroelastic variant r_i there are two possible ferroelectric states $P_i^{\pm}$, with P_i^+ and P_i^- having (in projection onto the $(001)_c$-axis) a polarization state pointing upwards, away from the substrate, and downwards, towards the substrate, respectively [50]. In regions where different ferroelastic/ferroelectric domains meet, the so-called "domain walls", different distortions and polarization directions meet. In the ideal case the domains in the BFO film align in such a way that both mechanical compatibility and electric compatibility are satisfied. The domain walls are named after the angle between the polarization directions in the two adjacent domains; in the same manner the switching processes are named. The ideal arrangements for rhombohedral ferroelectrics in general have been studied by Streiffer *et al.* [50]. The coherent twin boundaries which satisfy the structural compatibility were obtained by calculating and comparing the spontaneous strain of two adjacent ferroelastic domains. The results allow two different kinds of twin patterns: 109° stripe domains with $\{100\}_c$ twin boundaries (Fig. 2.7(c)) and 71° stripe domains with $\{101\}_c$ twin boundaries (Fig. 2.7(d)). The 109° domain boundaries have vertical domain walls, an alternating polarization up and down and a net in-plane polarization, as shown for the example of r_1/r_2 twin pattern in Fig. 2.7(e). On the other hand, the 71° stripe domains have 45° tilted domain walls, a uniform out-of-plane projection and a net polarization pointing perpendicular to the twin boundary, as seen for the example of r_1/r_4 in Fig. 2.7(f). The head-to-tail configuration for the polarization in all twin patterns is a consequence of minimizing the electrostatic energy [50].

2.3.2 Substrate crystals

In this work BFO thin films were grown on several different substrates to impose a different epitaxial stress onto the BFO film and investigate its influence. For a good epitaxial growth of the BFO film on top of the substrate, the structure and lattice constants of the substrate should be close to those of BFO. Here strontium titanate, $SrTiO_3$ (STO), and three of the orthorhombic rare-earth (RE) scandates, $REScO_3$ (with RE = Dy, Gd, Sm), were used. STO is a cubic and paraelectric material at room temperature, which crystallizes in the pervoskite structure with a lattice constant of $a_c = 3.905\,\text{Å}$ [51]. The $REScO_3$ on the other hand have a more complex crystal structure, but the advantageous property that the lattice constant can be tuned by the choice of the rare earth ion. The structure is isomorphic to the one of $GdFeO_3$ [52], which consists of four perovskite pseudocubes in one orthorhombic unit cell. The oxygen octahedrons are tilted in the $a^-a^-c^+$ type defined by Glazer [31]. Therefore, the orthorhombic unit cell has to be chosen to account for the full symmetry. The orientation of the pseudocubes with respect to the orthorhombic unit cell is shown in Fig. 2.8(a). The orthorhombic $[110]_o$-direction corresponds to the cubic $[001]_c$-direction. The pseudocubes within the orthorhombic unit cell are distorted from the ideal cubic perovskite structure by a monoclinic distortion, coming from the different lengths of the orthorhombic unit vectors a_o and b_o. In addition, the two in-plane lattice constants a_c and b_c differ. The pseudocubic lattice constants
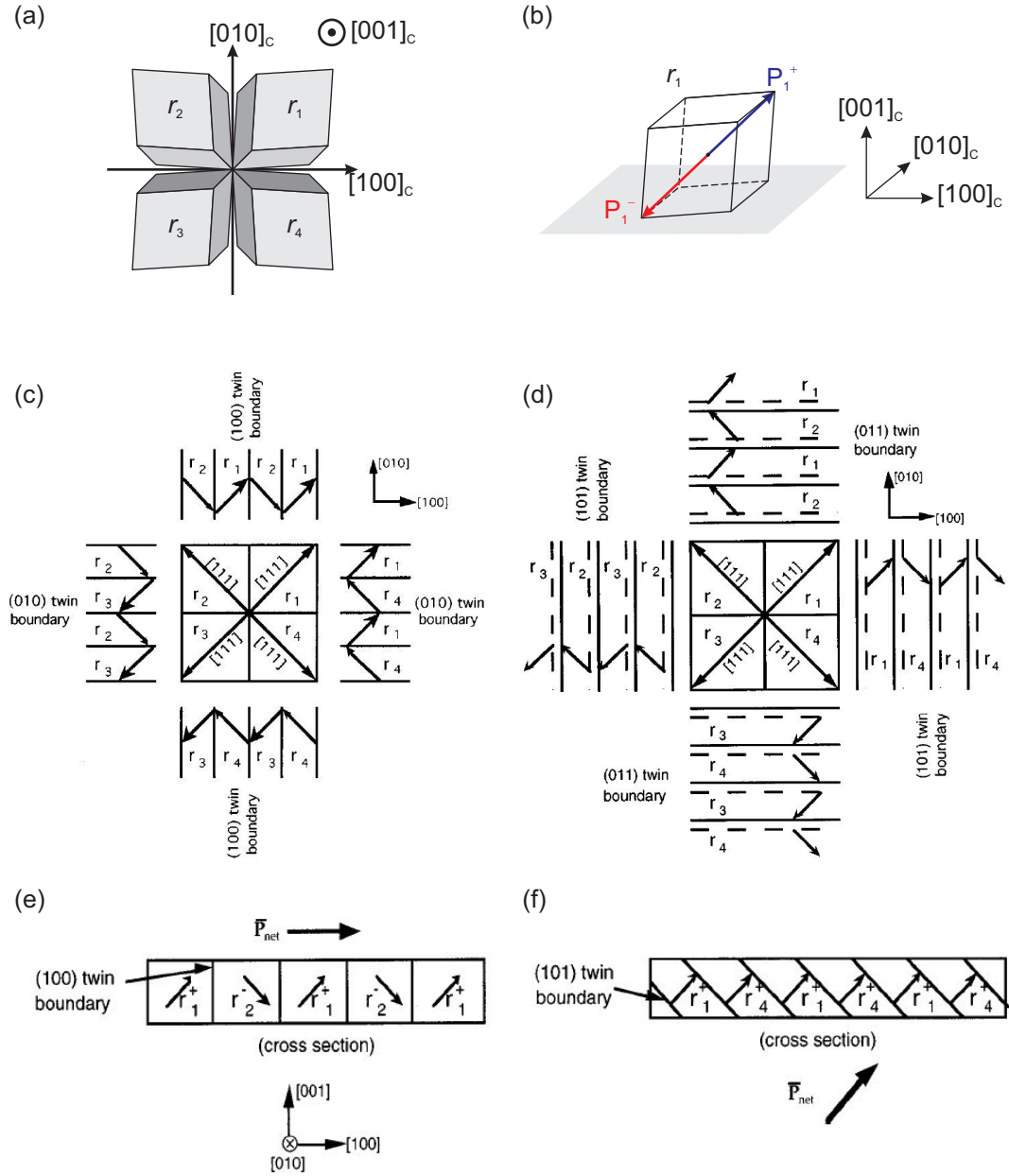
Figure 2.7: (a) Possible ferroelastic variants r_1, r_2, r_3 and r_4 for $(001)_c$-oriented BFO films depicted in topview with exaggerated rhombohedral distortions. (b) For each ferroelastic variant r_i there are two possible ferroelectric variants $P_i^\pm$, here shown for r_1. (c) $\{100\}_c$-r_i/r_j twin patterns in topview projected down $[001]_c$. The domains have alternating polarization up and down and form 109° domain walls. (d) $\{101\}_c$-r_i/r_j twin patterns in topview projected down $[001]_c$. (e) Example for 109° domain pattern with r_1/r_2 variants shown in cross section view. The twin pattern has a net polarization pointing along $[100]_c$. (f) Example for 71° domain pattern with r_1/r_4 variants shown in cross section view. The twin pattern has a net polarization pointing along $[101]_c$. (c)-(f) are taken from Ref. [50].

11
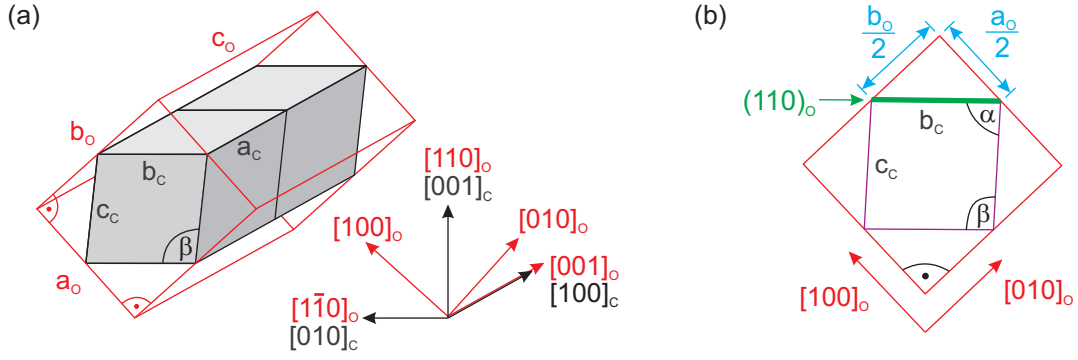
Figure 2.8: (a) Schematics of the orthorhombic unit cell, with two of the four perovskite pseudocubes drawn inside. The pseudocubic axes (with index "c") are defined with respect to the orthorhombic axes (with index "o") as sketched in the Figure and used throughout this thesis. (b) Projection of the unit cell along the $[001]_o$-axis or $[100]_c$-axis, respectively. The $(110)_o$-cut corresponds to a $(001)_c$-cut in cubic notation. The perovskite pseudocubes are monoclinically distorted with angle β, if the orthorhombic lattice constants a_o and b_o are unequal.

	a_o [Å]	b_o [Å]	c_o [Å]	a_c [Å]	b_c [Å]	β [°]	Misfit with BFO	Misfit with SRO
STO				3.905			$-1.4\,\%$	$-0.6\,\%$
DSO	5.440	5.717	7.903	3.952	3.946	92.8	$-0.3\,\%$	$+0.5\,\%$
GSO	5.480	5.746	7.932	3.966	3.970	92.7	$+0.2\,\%$	$+1.0\,\%$
SSO	5.527	5.758	7.965	3.983	3.991	92.3	$+0.7\,\%$	$+1.4\,\%$

Table 2.1: List of substrates used in this thesis. For the rare earth scandates the orthorhombic lattice constants a_o, b_o and c_o are given [53], as well as the calculated pseudocubic in-plane lattice constants a_c and b_c and monoclinic distortion angle β. For the cubic STO the lattice constant a_c is given [51]. For all substrates the (averaged) misfit values with BFO and SRO are listed.

with the monoclinic distortion angle can be calculated geometrically from the schemes in Fig. 2.8(a) and 2.8(b).

$$a_c = \frac{c_o}{2} \tag{2.4}$$

$$b_c = c_c = \sqrt{\left(\frac{a_o}{2}\right)^2 + \left(\frac{b_o}{2}\right)^2} \tag{2.5}$$

$$\beta = 180° - 2\arctan\left(\frac{b}{a}\right) \tag{2.6}$$

The lattice constants of the used rare earth scandates are listed together with the lattice constants of STO in Table 2.1. Due to the slight lattice mismatch with the BFO (see Sec. 2.3.1.1) an epitaxial strain will be imposed onto epitaxial BFO film grown on top of the substrate, defined by [54]

$$m = \frac{a_0 - a_f}{a_0} \tag{2.7}$$
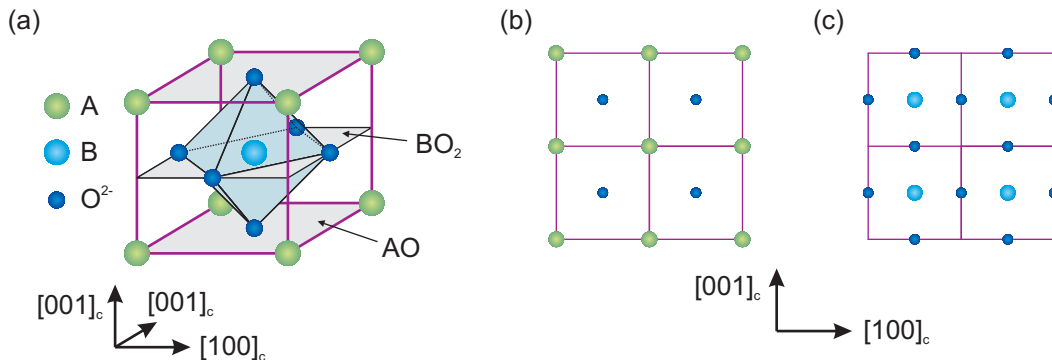
Figure 2.9: (a) General perovskite structure ABO_3 with cations A and B. For a $(001)_c$-cut there are the two possible terminations AO and BO_2. The terminations are shown in top view for (b) AO and (c) BO_2.

where a_0 is the bulk lattice constant and a_f the actual in-plane lattice constant in the film. For fully strained films the in-plane lattice constant is equal to the substrate in-plane lattice constant. With the here used set of substrates an epitaxial strain ranging from -1.4% to $+0.7\%$ can be imposed onto the BFO film.

In a $(001)_c$-cut of a general perovskite ABO_3 (Fig. 2.9(a)) there are two possible terminations, either an AO (Fig. 2.9(b)) or a BO_2 (Fig. 2.9(c)) termination. In case of STO these terminations are SrO and TiO_2, which are both non-polar. On the other hand, the terminations of the $REScO_3$ crystals consist of either REO^+ or ScO_2^-, both of which are polar.

2.3.3 Electrode materials

2.3.3.1 Strontium ruthenate

Strontium ruthenate, $SrRuO_3$ (SRO), is a metallic conductor with a bulk resistivity of $\rho = 2.75 \times 10^{-4}\,\Omega$cm at room temperature [55], and orders ferromagnetically below $160\,$K [56]. At room temperature SRO is paramagnetic and has an orthorhombic crystal structure with an $a^-a^-c^+$ Glazer oxygen tilt system [31, 57, 58], similar to the $REScO_3$ substrate crystals (Sec. 2.3.2). The orthorhombic lattice constants as well as the pseudocubic lattice constants calculated from Equation (2.4)-(2.6) are given in Table 2.2. For SRO films under compressive strain the orthorhombic structure with $a^-a^-c^+$ oxygen octahedron tilt system is maintained, however for films under tensile strain a transition to a tetragonal symmetry with $a^+a^+c^0$ oxygen octahedron tilt system has been reported [58, 59].

	a_o [Å]	b_o [Å]	c_o [Å]	a_{rh} [Å]	α_{rh} [°]	a_c [Å]	b_c [Å]	β [°]
SRO	5.532	5.572	7.850			3.926	3.925	90.4
LSMO				5.471	60.43	3.88		90.2

Table 2.2: List of oxide electrodes used in this thesis. The orthorhombic lattice constants for SRO are taken from Ref. [55] and the pseudocubic lattice constants are calculated from Eq. (2.4)-(2.6). The rhombohedral lattice constants for LSMO are taken from Ref. [60] and the pseudocubic lattice constants from Ref. [61].

2.3.3.2 Lanthanum strontium manganite

Lanthanum strontium manganite (LSMO) is an oxide material which has the general formula $La_{1-x}Sr_xMnO_3$. In the insulating and antiferromagnetic $LaMnO_3$ all manganese ions are in the Mn^{3+} valence state ($La^{3+}Mn^{3+}O_3^{2-}$). For each La^{3+} ion, which is substituted by a Sr^{2+} ion, one Mn^{3+} ion changes its valance state to Mn^{4+}, leading to ferromagnetism and conductivity [62]. Here a composition of $La_{0.7}Sr_{0.3}MnO_3$ was used. For this composition LSMO has a resistivity of approximately $8 \times 10^{-4}\,\Omega cm$ [63] at room temperature, and orders ferromagnetically below $T_C = 369\,K$ [64].

In bulk form, LSMO has a rhombohedral structure with an $a^-a^-a^-$ Glazer oxygen octahedron tilt system, which can be considered pseudocubic as well [58]. The lattice parameters are listed in Table 2.2, and are smaller than the ones for SRO. Similar to SRO, LSMO films grown on substrates performing a tensile strain change the crystal symmetry of LSMO to an orthorhombic symmetry [65].

2.4 Summary

This section gave an introduction to ferroelectrics and multiferroics. The materials used in this thesis and their properties were described. In particular the main material of investigation, BFO, which is one of the few single phase multiferroic materials at room temperature, was introduced. Its ferroelectric and antiferromagnetic behavior, as well as its theoretical energetically favorable ferroelectric/ferroelastic domain patterns and domain walls were explained. In addition all used single crystal substrates and their structural symmetry and properties were discussed.

Experimental setup and characterization methods

In this chapter the experimental techniques are introduced. In particular, the sample fabrication and the characterization tools are explained, which include among others piezoresponse force microscopy (PFM), X-ray diffraction (XRD), transmission electron microscopy (TEM), and ferroelectric measurements.

3.1 Sample fabrication

Epitaxial thin oxide films and heterostructures of BFO, SRO and LSMO were grown by pulsed laser deposition (PLD). If required, structured top electrodes were deposited *ex situ* on top of the films by radio frequency sputtering, thermal evaporation, or room temperature PLD.

3.1.1 Growth by pulsed laser deposition

Pulsed laser deposition (PLD) has become a widely used tool for high quality growth of oxide films [66, 67]. Its advantages over other deposition methods are its flexibility, the stoichiometric transfer from target to substrate, the energetic evaporated particles and the clean heat source. In addition, it is a very suitable technique for multilayer growth [68, 69].

The basic principle of PLD is shown in Fig. 3.1. A pulsed laser (KrF excimer laser, Lambda Physik LPX 300) with an ultraviolet wavelength $\lambda = 248$ nm and a pulse length of approximately 20 ns is focused by a lens and fed through a quartz window into a vacuum chamber. A ceramic target of the material to be deposited is placed in the focal point of the laser. For a sufficiently high laser energy fluency, each pulse will ablate part of the material. The target is rotated and toggled during the deposition in order to ablate material from different regions of the target and avoid the formation of cones [70]. The ablated material forms a strongly forward oriented plasma plume, which condenses on a target placed 5.5 cm away. For *in situ* growth of multilayers, the target can be exchanged in a target carousel.

Reactive or inert gases, such as oxygen, can be introduced into the vacuum chamber through a gas inlet, which on the one hand reduces the kinetic energy of the ablated species [71] and on the other hand is a reactive environment for forming oxygen containing compounds [69]. The substrate is fixed to a controlled heating stage to allow for epitaxial
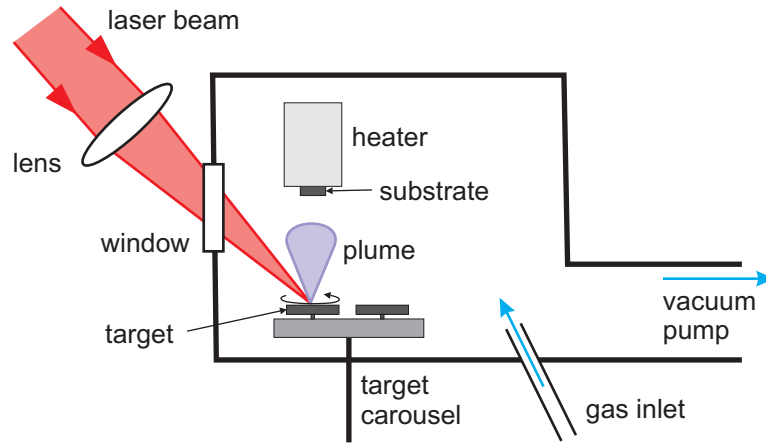
Figure 3.1: Schematic view of the used PLD chamber.

Target diameter	$\approx 5\,\mathrm{cm}$
Target supplier	PRAXAIR
Target composition	stoichiometric
Target purity	99.9 %
Ablation temperature	650°C
Ablation laser frequency	5 Hz
Ablation background gas	0.14 mbar O_2
Heating rate	20°C/min
Cooling rate	15°C/min
Atmosphere during heating	$< 7 \times 10^{-6}$ mbar below 300°C
	0.14 mbar O_2 above 300°C
Atmosphere during cooling	200 mbar O_2

	BFO	SRO	LSMO
Ablations pulse energy [mJ]	$30 - 90$	130	95
Corresponding laser fluency [J/cm^2]	$0.13 - 0.38$	0.54	0.40
Resulting growth rate [nm/min]	$0.5 - 1.5$	≈ 6	n. a.

Table 3.1: Procedure for PLD growth and list of parameters for films grown by PLD

growth of the film. After deposition the oxygen partial pressure can be increased for recovering part of the oxygen concentration, since often the oxygen is not incorporated with the full stoichiometric ratio.

All materials employed here could be grown with similar parameters, only different laser pulse energies had to be applied for each material. The standard parameters for all grown materials are listed in Table 3.1.

3.1.2 Top electrode deposition

Macroscopic top electrodes were deposited by clamping a mask on the sample which serves as shadow mask during deposition. Two different types of commercially available masks were used, whose intended purpose are actually accessories for transmission elec-

tron microscopy. The one type of mask consisted of a copper metal grid with square holes of different sizes ranging from $11 \times 11\,\mu m^2$ to $100 \times 100\,\mu m^2$. The resulting electrodes consisted of an array of squares with the same dimensions as the holes. This type of electrodes were used for out-of-plane electrical measurements. The second type of mask had just two holes with a side length of $1\,mm$, which were separated by a $20\,\mu m$ bar. Thus, the two resulting electrodes had a gap of $20\,\mu m$ between each other and were used for in-plane electrical measurements.

The electrode material was deposited either by thermal evaporation in case of gold or copper, by radio-frequency sputtering in case of platinum, or by room temperature PLD in case of SRO. Since a mask has to be fixed on top of the sample, the electrode deposition had to be performed *ex situ* after the PLD film growth. In case epitaxial *in situ* top electrodes were required, a uniform LSMO layer was grown by PLD immediately after the BFO film growth. Subsequently, patterned platinum electrodes were deposited *ex situ*. Afterwards, the LSMO film which was not capped by platinum was etched away, resulting in Pt/LSMO/BFO/SRO capacitors.[1]

3.2 Methods for structural and functional characterization

After sample fabrication several investigation techniques were employed for characterization. The atomic force microscope (AFM) was used for investigating the surface morphology, and with the special operation mode PFM the ferroelectric domains were visualized as well as manipulated. For probing the structural quality and epitaxy XRD and TEM were used. For the determination of the polarization, ferroelectric hysteresis curves were obtained.

3.2.1 Atomic force microscopy

The atomic force microscope (AFM) was invented by Binnig, Quate and Gerber in 1986 [72] and is until today a widely used tool due to its high versatility. Originally invented for studying the surface morphology of samples down to atomic resolution [73], many different operation modes have been developed in the meantime to investigate a multitude of different physical properties, e.g. detecting electric charges [74], measuring the surface elasticities [75], conductivities [76], and magnetic forces [77]. In the field of ferroelectrics the PFM operation mode (see Sec. 3.2.1.2) of the AFM has become a standard tool to visualize and influence the ferroelectric domains [78].

3.2.1.1 Basic working principle

The AFM belongs to the family of scanning probe microscopes, which have the following working principle. A probe is scanned over a sample surface and the measuring signal is compared in a feedback loop with a set value. The output of the feedback loop is applied to a piezoelectric actuator, so that the distance between sample and probe is kept constant. At the same time the output signal of the feedback loop reflects the topography of the sample surface (Fig. 3.2).

---

[1]LSMO was etched with the following solution: $31\,ml$ H_2O, 10 ml H_2O_2 and $0.1\,ml$ H_2SO_4. Etch rate is approximately $0.5\,nm/min$.
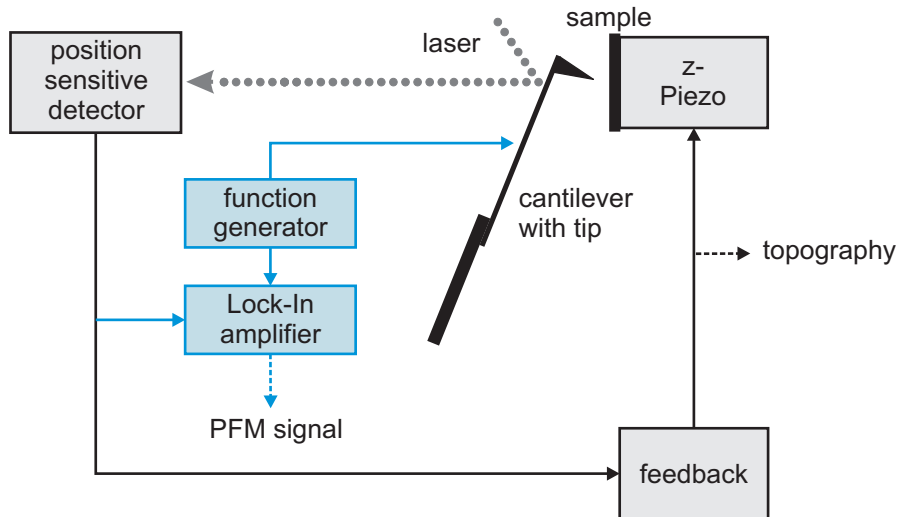
Figure 3.2: Schematic working principle of the atomic force microscope. The extensions for PFM are colored in blue.

In case of AFM the probe consists of a cantilever with a sharp tip at its end. The forces between the tip and the sample lead to a deformation of the cantilever, which is detected by the so-called optical lever mode. As depicted in Fig. 3.3, a laser beam is focused on the backside of the cantilever and the reflected laser beam is detected by a segmented photodiode. A normal force F_n leads to a deflection of the cantilever which is seen as a vertical movement of the laser spot on the photodiode. An in-plane force F_b parallel to the long side of the cantilever results in a buckling and as well a vertical movement on the photodiode. On the other hand, an in-plane force F_t acting perpendicular to the cantilever leads to a torsion of the cantilever and a lateral movement of the laser spot. By comparing the measured intensities on the photodiodes A, B, C and D, the position of the laser beam can be obtained and conclusions about the cantilever deformation drawn.

$$(A + B) - (C + D) \rightarrow \text{vertical signal (deflection, buckling)} \tag{3.1}$$
$$(A + C) - (B + D) \rightarrow \text{lateral signal (torsion)} \tag{3.2}$$

All forces can be detected simultaneously, however the forces F_n and F_b appear in the same readout channel and they can therefore not be separated.

For scanning the sample with the AFM, the normal force coming from the Lennard-Jones potential is used. Generally, between two atoms there act always attracting van der Waals forces and repulsing forces coming from the Pauli repulsion. The van der Waals forces are relatively long-range ($< 100\,\text{nm}$), whereas the Pauli repulsion dominates at short ranges ($< 1\,\text{nm}$). Both interactions are summarized in the Lennard-Jones potential and are most of the times given in the following form

$$V(z) = 4\epsilon \left[\left(\frac{\sigma}{z} \right)^{12} - \left(\frac{\sigma}{z} \right)^{6} \right] \tag{3.3}$$

with z being the distance between the atoms, ϵ the depth of the potential and σ the distance for vanishing potential $V(z) = 0$ (Fig. 3.4(a)). The force can be obtained by taking the derivative of the potential and it will vanish at the potential minimum.
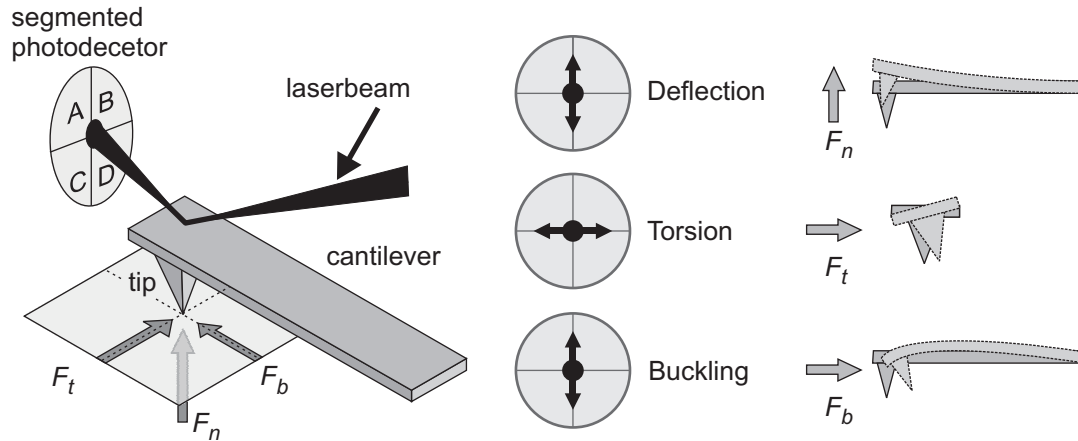
Figure 3.3: Schematics of the simultaneous detection of normal forces F_n and in-plane force, i.e. torsion F_t and buckling F_b, with the optical lever mode. Deflection and buckling lead to a vertical signal, whereas torsion leads to a lateral signal.

There are different AFM operation modes possible. In the "contact mode" the steep front part of the potential, which allows for best depth resolution, is used to control a fixed deflection of the cantilever (Fig. 3.4(b)). The tip is, as the name suggests, in contact with the sample. Due to the occurring friction during scanning noise is introduced which degrades the resolution. To overcome the friction and improve resolution the "tapping mode" can be used (Fig. 3.4(c)). Here, a dynamic mode is used by exciting the cantilever to a vibration at its resonance frequency and taking the vibration amplitude as the feedback signal. When approaching the surface, the vibration gets damped and the average distance can be controlled by a constant amplitude. During the vibration the tip is in contact with the sample just for a short time. The influence of friction is thus reduced and at the same time the steep front part of the potential is still used for obtaining a high depth resolution. Although the "tapping mode" has the best resolution for mapping the topography, for many operation modes the "contact mode" is used because a steady contact between tip and sample surface is required.

3.2.1.2 Piezoresponse force microscopy

The piezoresponse force microscopy (PFM) mode is a special contact operation mode of the AFM which allows the local mapping of the piezoelectric response of a sample. As described in Sec. 2.1, ferroelectricity entails piezoelectricity, and therefore all ferro-electrics show a piezoelectric response which can be used for domain visualization by PFM. It can measure piezoelectric displacements $< 1\,\mathrm{pm}$ [79] and has a lateral resolution limited by the radius of curvature of the tip, which can reach a few nanometers [80].

Principle of PFM

The PFM technique is based on the converse piezoelectric effect, which refers to a linear coupling between a mechanical strain x and an applied electric field E. In PFM an alternating voltage V_{ac} is applied to a conductive AFM tip to impose the electric field E to the sample, and a lock-in amplifier is used to detect the resulting vibration (Fig. 3.2).

(a)

(b)

(c)
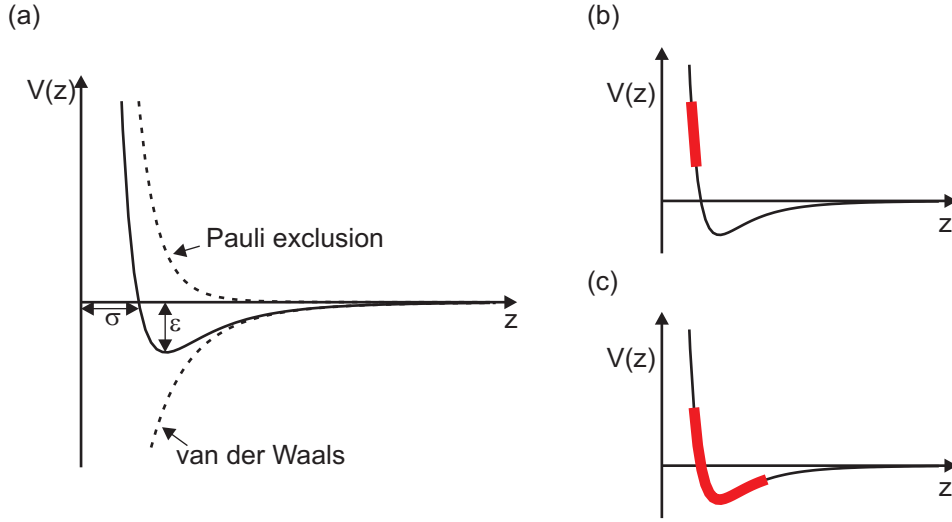
Figure 3.4: (a) Lennard-Jones potential and the average tip-sample distance highlighted for (b) the contact mode and (c) the tapping mode.

If the vertical signal of the segmented photodiode is fed to the lock-in amplifier an out-of-plane vibration is measured which is called vertical PFM (VPFM); in case the lateral signal is used a lateral movement of the tip is measured which is called lateral PFM (LPFM). How the direction of polarization can be obtained from the detected vibrations will be described in the following.

The piezoelectric tensor d is a third rank tensor and connects the applied electric field E with a resulting strain x. Because the strain tensor is symmetric ($x_{ij} = x_{ji}$) it follows that only 18 from the possible 27 piezoelectric tensor components are independent [17]. In addition, for particular crystal symmetries further restrictions for the tensor elements can be drawn from Neumann's law [17]. For example, crystals with point group $3m$ (e.g. BFO) having a hexagonal coordinate system (the third axis is along the direction of polarization) the following relationship holds [17]

$$\begin{pmatrix} x_1 \\ x_2 \\ x_3 \\ x_4 \\ x_5 \\ x_6 \end{pmatrix} = \begin{pmatrix} 0 & -d_{22} & d_{31} \\ 0 & d_{22} & d_{31} \\ 0 & 0 & d_{33} \\ 0 & d_{15} & 0 \\ d_{15} & 0 & 0 \\ -2d_{22} & 0 & 0 \end{pmatrix} \times \begin{pmatrix} E_1 \\ E_2 \\ E_3 \end{pmatrix} \tag{3.4}$$

where x_j describes an elongation/contraction along the corresponding principle axis in case of $j = 1, 2, 3$, and a shear strain in case of $j = 4, 5, 6$.

Due to the inhomogeneous electric field imposed by the tip and the many piezoelectric tensor elements the resulting strain can be rather complex. However, for ferroelectric films the resulting strain is often dominated by the elongation/contraction along the direction of spontaneous polarization. With the knowledge of the crystallographic orientation of the film or crystal, the direction of polarization can be deduced. For instance, in case of a film or crystal with the symmetry of the piezoelectric tensor given above, which has the polarization oriented fully out-of-plane, the electric field generated by the

AFM tip with applied voltage V is mostly parallel or antiparallel to the direction of polarization. Neglecting the field components E_1 and E_2, the dominating out-of-plane deformation is $x_3 = d_{33} \cdot E_3$, leading to a displacement for a crystal or film of thickness t on a grounded back electrode of [81]

$$\Delta t = \int_0^t d_{33} E_3 \mathrm{d}x_3 = d_{33} \cdot V \tag{3.5}$$

Whether a contraction or elongation occurs depends on the orientation of the polarization with respect to the electric field direction and is the key for ferroelectric domain visualization. Since an alternating voltage V_{ac} is applied to the tip, two adjacent 180° domains will have the same vibration amplitude in the VPFM signal, but a phase shift of 180° with respect to the applied alternating voltage.

In the other extreme case, when the direction of polarization is completely in the plane of the sample, no PFM signal should be expected from the mechanism described above. However, an in-plane movement can be detected by LPFM if the direction of the polarization is perpendicular to the cantilever orientation.[2] There exist two possible explanations for the origin of the lateral movement. Either it originates from a shear movement described by the tensor element d_{15} or an in-plane contraction and elongation described by the tensor element d_{33}, where the first one might be suppressed due to clamping [78, 82].

In the general case that the polarization is aligned with an angle $0° \leq \alpha \leq 90°$ to the sample plane normal, the projection to the normal is seen in VPFM, whereas the projection in the sample plane and perpendicular to the cantilever is seen in LPFM [82].

The PFM signal can be acquired in two equivalent ways, either in two images, the phase image φ and the amplitude image R, or as X image combining information in one image $X = R \cdot \cos\varphi$.

PFM performed on $(001)_c$-oriented BiFeO$_3$

This section describes the domain visualization of $(001)_c$-oriented BFO films by PFM, which are the kind of films investigated in this thesis. As shown in Sec. 2.3.1, there are eight possible variants for the ferroelectric polarization in $(001)_c$-oriented films. In the last section it has been explained that VPFM can visualize the out-of-plane projection of the polarization, whereas the LPFM can visualize the in-plane projection perpendicular to the cantilever. Figure 3.5 shows which variants of polarization can be distinguished in PFM [83, 84]. No matter of the cantilever orientation, from VPFM (Fig. 3.5(a)) it can only be concluded whether the polarization is one of the four pointing up or one of the four pointing down. If the cantilever is aligned along the $[010]_c$-axis (Fig. 3.5(b)), from LPFM it can be distinguished between the four variants with a component in $[100]_c$-direction and the four variants with a component in $[\bar{1}00]_c$-direction. In case the cantilever is aligned along $[100]_c$ (Fig. 3.5(c)), the component along $[010]_c$ or $[0\bar{1}0]_c$ can be determined. The VPFM image and the LPFM image for one of the two described cantilever orientations can be taken at the same time. Combining the information obtained by the two images allows to narrow the possible polarization variant down to two of the original eight. For a univocal determination of the polarization variant two images of the same area with both cantilever orientations have to be acquired and superimposed.

---

[2] In case the polarization is aligned parallel to the cantilever, the signal will be seen as buckling in VPFM instead.
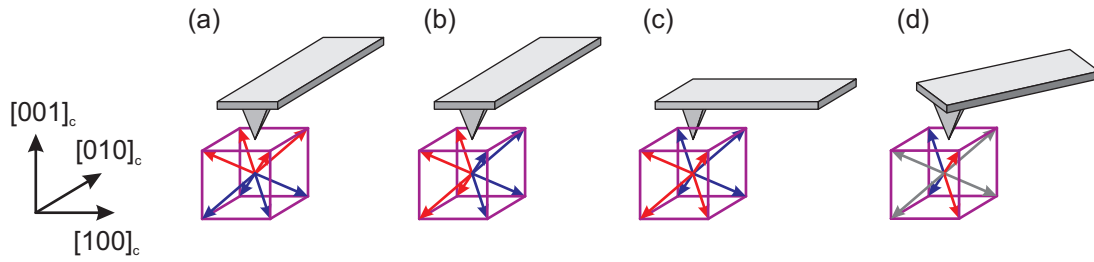
Figure 3.5: Schematics of which polarization directions can be distinguished by PFM. Directions which will give the same PFM signal are colored identical for (a) VPFM and (b)-(d) LPFM with the cantilever oriented (b) 0°, (c) 90° and (d) 45°.

Another possibility is the imaging with a cantilever orientation along the $[110]_c$-direction (Fig. 3.5(d)), which will give rise to three different contrasts in LPFM. Polarization variants pointing along the cantilever will give no LPFM signal, whereas the variants with a component along $[\bar{1}10]_c$ and $[1\bar{1}0]_c$ have the same LPFM amplitude, but a 180° phase shift with respect to each other. Again, for a univocal determination two scans with different cantilever orientations have to be performed.

3.2.2 X-ray diffraction

X-ray diffraction (XRD) is an important tool to check the film's crystalline quality, phase purity and epitaxial relationship to the substrate. If x-rays irradiate a material, the photons primarily interact with the electrons and part of the photons will be deflected. If the wavelength does not change, the process is called elastic scattering, or Thomson scattering. These elastically scattered x-rays are used in XRD measurements, since in this case a momentum transfer carries information about the electron distribution of the sample. In case of ordered atoms, i.e. in crystals, the diffraction appears in sharp interference peaks which allow to draw conclusions about the crystal lattice spacings. For a lattice with inter-plane spacing d and incoming x-rays with wavelength λ (Fig. 3.6(a)) the condition for a diffraction peak is given by Bragg's law

$$n\lambda = 2d\sin\Theta \qquad\qquad (n = 1, 2, 3, ...) \qquad\qquad (3.6)$$

where n represents the order of diffraction and 2Θ the angle of diffraction. The x-ray wavelength has to be smaller than twice the inter-plane spacing, in order to allow for Bragg diffraction.

The used setup (Philipps X'Pert MRD, type 3050/65) is schematically shown in Fig. 3.6(b). The x-rays are generated by focusing high energetic electrons on a copper target. By the collision between the electrons and the copper atoms the electrons are slowed down, generating Bremsstrahlung and ionizing inner shells of the copper atoms. When an electron of a higher shell fills the free spot in the inner shell, an x-ray photon with characteristic energy is emitted. For the copper target, the lines K_{α_1} and K_{α_2}, with very close wavelength of $\lambda(K_{\alpha_1}) = 1.5406\,\text{Å}$ and $\lambda(K_{\alpha_2}) = 1.5444\,\text{Å}$, respectively, have the highest intensity and were therefore used for the measurement. Moreover, the line K_β from copper ($\lambda = 1.3923\,\text{Å}$), and the line L_{α_1} from tungsten ($\lambda = 1.4764\,\text{Å}$) impurities appear as well. For one particular plane spacing d all of these x-ray lines produce a diffraction peak at different Θ_λ values. The K_β of copper and K_α of tungsten can be
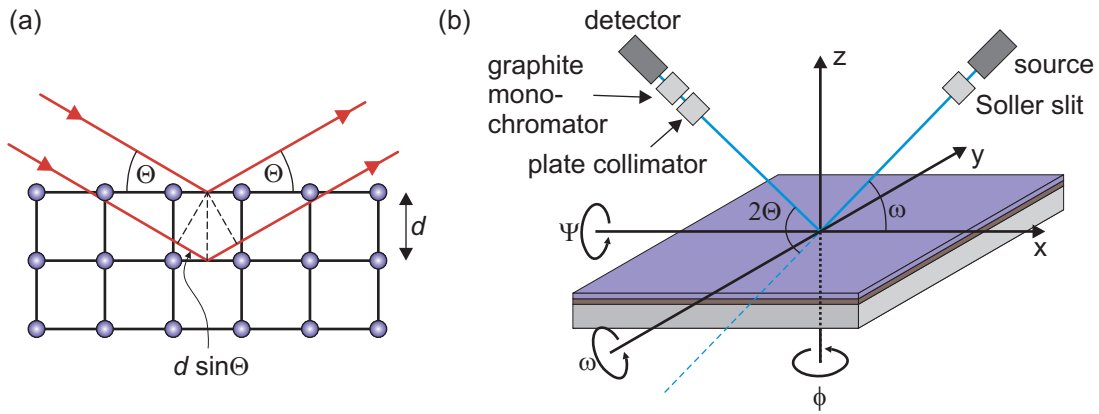
Figure 3.6: (a) X-ray diffraction for a crystal with inter-plane spacing d. A diffraction peak is visible at 2Θ if the additional way $2d\sin\Theta$ is equal to an integer multiply of λ. (b) Schematics of the x-ray diffraction setup with definition of the used angles.

suppressed by inserting a nickel filter (absorption edge at $1.49\,\text{Å}$). The two lines K_{α_1} and K_{α_2}, however, can not be separated and will always produce two diffraction peaks. In our setup with a Soller slit after the source and a plate collimator before the detector, an angular resolution for 2Θ of about $0.3°$ is achieved. As a result, for low angles of Θ the two peaks can not be resolved in our setup and an average peak is seen. For higher angles Θ the peak splitting is visible though.

The sample is placed in a Eulerian cradle to allow he sample to move in all three space axes x, y, and z. In this way different sets of atomic planes can be investigated and the position of the sample with respect to the incident x-ray beam adjusted.

3.2.2.1 $2\Theta/\omega$-scans

In $2\Theta/\omega$-scans the sample is tilted in steps by the amount $\Delta\omega$ and at the same time the detector is moved by twice the amount $\Delta(2\Theta) = 2 \cdot \Delta\omega$. Thus, different inter-plane spacings are probed, but the orientation of the planes is kept fixed. Often $2\Theta/\omega$-scans are used to scan the inter-plane spacings parallel to the sample surface, which means that $\omega = \Theta$. In this way the out-of-plane lattice constant of the deposited film can be extracted, and in addition, impurity phases which are aligned parallel to the sample surface can be detected.

When executing such a $2\Theta/\omega$-scan, first the sample has to be aligned, usually by adjusting Ψ and Φ so that one substrate reflection peak, e.g. STO(002), is maximized. Afterwards the film peak positions can be measured. The best values are achieved if several orders of diffraction are measured and the extracted values are then fitted by the empiric Nelson-Riley function f_{NRF} [85]:

$$f_{\text{NRF}}(\Theta) = \frac{1}{2}\left[\frac{\cos^2\Theta}{\sin\Theta} + \frac{\cos^2\Theta}{\Theta}\right] \tag{3.7}$$

The Nelson-Riley function extrapolates the measurements to $2\Theta = 180°$, which corresponds to complete back scattering where the systematic errors are smallest, but which is experimentally not possible to perform.

(a)

(b)
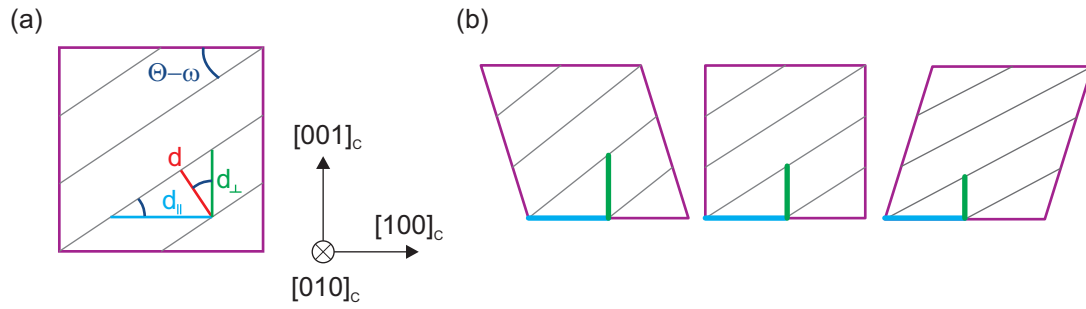
Figure 3.7: (a) Schematics of in-plane and out-of-plane lattice constant extraction from RSM. (b) For an in-plane monoclinic distortion the extracted out-of-plane distance depends on the orientation of the monoclinic crystal.

3.2.2.2 Reciprocal space maps

For additional information, for instance the degree of strain in the film or epitaxial relations between substrate and film, reciprocal space maps (RSMs) can be performed. In RSMs a range of inter-plane spacings and plane orientations is scanned. In detail, several $2\Theta/\omega$-scans with different values of $(\Theta - \omega)$, called offset, are acquired. To achieve in-plane and out-of-plane information usually a reciprocal space window around $(h0l)_c$ or $(0kl)_c$ is scanned. The measured peak position with inter-plane spacing d and offset tilt $(\Theta - \omega)$ can be decomposed into a part parallel to the sample surface and a part perpendicular to the sample surface. Figure 3.7(a) shows an example for a cubic material where the $(203)_c$ planes are considered. The measured inter-plane spacing d can be decomposed in the following way (valid for all crystal symmetries):

$$d_\parallel = \frac{d}{\sin(\Theta - \omega)} \tag{3.8}$$

$$d_\perp = \frac{d}{\cos(\Theta - \omega)} \tag{3.9}$$

The unit cell parameters, a in-plane and c out-of-plane, are obtained in this case by multiplying $d_\parallel$ and $d_\perp$ with the corresponding Miller indicies:

$$a = h \cdot d_\parallel = 2 \cdot d_\parallel \tag{3.10}$$

$$c = l \cdot d_\perp = 3 \cdot d_\perp \tag{3.11}$$

This, however, holds just for certain symmetries, such as cubic or tetragonal. In case of a monoclinic in-plane distortion of the pseudocubic unit cell, for instance, the extracted out-of-plane parameter depends on the crystal orientation, as depicted in Fig. 3.7(b). Here, all orientations give the same in-plane projection, but three different out-of-plane parameters. In this way the direction of distortion can be determined by XRD. Regarding the extracted lattice parameters, it can only be said, that the extracted distances are equal to the projection of the inter-plane spacing on the sample surface normal and the projection perpendicular to the sample surface normal. Nevertheless, RSMs are an important tool to gain information about the distortion direction as well as about the in-plane and out-of-plane lattice constants.

3.2.3 Electron microscopy

Electron microscopy allows observations with a resolution several magnitudes higher than with light microscopy, because accelerated electrons have a much shorter wavelength than visible light. For instance, electrons with a kinetic energy of 100 keV have wavelengths of a few pm, although usually this resolution is not fully achieved because of lens aberrations.

In the microscope electrons are emitted from a hot cathode or generated by field emission. The electrons are then accelerated towards an anode with a voltage ranging from a few keV to several 100 keV. In the following transmission electron microscopy (TEM) and scanning electron microscopy (SEM) are shortly introduced.

All TEM images in this thesis were acquired by either Dr. Daniel Biggemann, Dr. Miryam Arredondo, Dr. Hakan Deniz or Dr. Eckhard Pippel.

3.2.3.1 Transmission electron microscopy

The working principle of the TEM is similar to the principle of a light microscope, with the difference that electrons are transmitted through the specimen instead of light [86]. For image acquisition either the hardly diffracted electrodes (bright field TEM), or the strongly diffracted electrons (dark field TEM) are used. The contrast seen in these images are a result of the interaction between the electrons and the atom cores in the specimen and consists of diffraction contrast, phase contrast and thickness contrast. To allow a transmission of electrons through the specimen the thickness of the specimens has to be just a few 10 nm. TEM allows to investigate the epitaxial relationship, film thickness, defects, interface sharpness, but also the visualization of domains. In case of scanning transmission electron microscopy (STEM), the specimen is scanned by a focused electron beam. Here the contrast mechanism is related to the atomic number.

All specimen were either prepared by conventional method [86] or by focussed ion beam (FIB) milling. Images were acquired by conventional TEM CM20T (Philips, 200 keV), by high resolution TEM (HRTEM), JEM-4010 (JEOL, 400 keV) or a scanning transmission electron microscope (STEM), Titan80-300 (FEI, 300 keV). A resolution down to a few Å is achieved, which is limited by the lens aberrations.

3.2.3.2 Scanning electron microscopy

In scanning electron microscopy (SEM) a focused electron beam of a few keV energy is scanned over a sample. The generated secondary electrons are detected in reflection, which allows to acquire the sample topography. The resolution is limited by the excitation volume in the sample and can go down to a few nm [87]. In this thesis a JSM 6701 (JEOL) with acceleration voltages of 3-5 keV was used.

3.2.4 Electric characterization

Often the ferroelectric properties of a thin film, or its behavior under fatigue are of interest. The ferroelectric properties can either be investigated macroscopically in out-of-plane or in-plane capacitors, or locally by PFM.

For macroscopic measurements the electrodes were connected either by silver paste in case of SRO bottom electrode or by a beryllium copper tip attached to a micro manipulator in case of evaporated top electrodes. To probe the ferroelectric hysteresis a voltage pulse as depicted in Fig. 3.8(a) was applied to the electrodes, either by a

(a)

(b)

Measurement
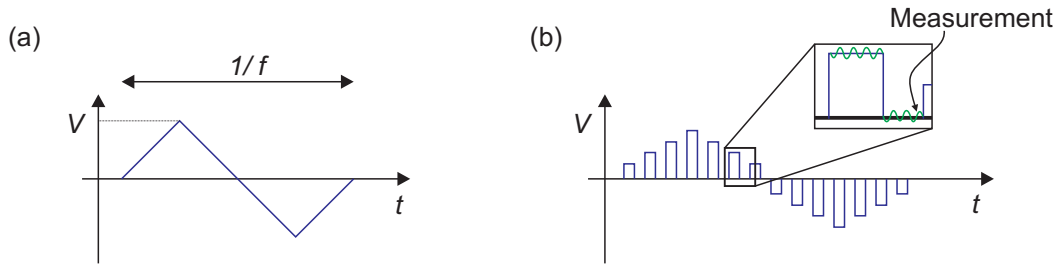
Figure 3.8: (a) Pulse form for acquiring a ferroelectric hysteresis curve. (b) Pulse form for obtaining a remanent piezoelectric hysteresis curve by PFM.

TF Analyzer 2000 (aixACCT) or by a Multiferroic tester (Radiant Technologies). The triangular voltage pulse has a frequency f and amplitude V. At the same time either the current or the integrated charge is measured. The measured signal stems from the ferroelectric contribution of interest, but as well from leakage contributions and capacitive charging. For frequencies in the kHz range, however, in most films the contribution of the ferroelectric polarization is dominant compared to leakage contribution. A possible capacitive charging contribution can be easily subtracted by a constant term from the current measurement I, because the voltage is raised linearly, so that $I = \frac{\Delta Q}{\Delta t} = C \cdot \frac{\Delta V}{\Delta t} = const$. The ferroelectric polarization can then be extracted, after the possibly required corrections, by the measured surface charge density $P_s = \frac{Q}{A}$, where A is the electrode area.

Fatigue measurements were performed by cycling the films with square pulses applied from a pulse generator AFG310 (Tektronik), amplified if voltages $> 10\,\text{V}$ were needed by the TF Analyzer amplifier. The rise time of the pulses was $75\,\text{ns}$ without amplifier and about 200-500 ns with amplifier.

For local ferroelectric switching investigations PFM can be employed. Several voltage pulses with increasing amplitude are applied, superimposed by an AC-voltage for PFM read-out (Fig. 3.8(b)). The PFM data are acquired in-between the pulses to obtain a remanent piezoelectric hysteresis curve, which contains the switching characteristics locally under the tip. Typical pulse length and delay times were $100\,\text{ms}$ with time constants of $10\,\text{ms}$ for the lock-in amplifier.

3.3 Summary

In this chapter the experimental methods were introduced. Thin oxide films are grown by PLD, additional top electrodes are then evaporated by thermal evaporation or sputtering through shadow masks. An important tool for characterization of the films is the AFM, which allows not only surface morphology mapping, but in the special operation mode PFM the visualization and manipulation of ferroelectric domains. With XRD and TEM structural properties, such as the epitaxy or strain states can be investigated. By electric measurements the ferroelectric properties can be tested, such as the value of spontaneous polarization and behavior under fatigue.

4

As-grown ferroelectric domains in epitaxial BiFeO₃ thin films

It has been described in Chapter 2.3.1 that there are four possible ferroelastic variants and eight possible ferroelectric variants in $(001)_c$-oriented BFO films, which are expected to form stripe domains if just the mechanical compatibility and electric compatibility between two adjacent domains are considered [50]. However, in thin epitaxial films additional boundary conditions affect the domain formation, such as the symmetry of the substrate and the lattice mismatch [84], the substrate miscut direction [88], the interface termination [89], and the electric boundary conditions [90]. It would be advantageous, if the domain variants can be reduced to simplify the domain structure and if the desired domain pattern for devices can be controlled by the boundary conditions.

In this chapter the pristine ferroelectric/ferroelastic domains in $(001)_c$-oriented BFO films grown on the substrates introduced in Sec. 2.3.2 are discussed. The aim is to give a thorough study of the influence of the boundary conditions, since often other studies reported in literature consider only one aspect. In particular, so far no study of the BFO domains grown on REScO₃ substrates exerting an in-plane tensile stress on BFO have been reported. Furthermore, the explanation given in literature [91, 92] of the domain formation on the REScO₃ substrates exerting an compressive in-plane stress is not sufficient and will be further completed.

BFO films were grown on STO(001)$_c$, DSO(110)$_o$, GSO(110)$_o$ and SSO(110)$_o$. With this set of substrates an in-plane strain ranging from $-1.4\,\%$ up to $+0.7\,\%$ can be investigated. The preparation of these substrates is briefly discussed in Sec. 4.1. For in-plane measurements BFO films deposited directly on the insulating substrate are of interest, whereas on the other hand for out-of-plane parallel plate capacitors first a layer of epitaxial SRO was deposited prior to the BFO film deposition. First the BFO films grown directly on the substrate are discussed in Sec. 4.2, then the films on the SRO buffered substrates are discussed in Sec. 4.3.

Part of the results in this chapter are published in Ref. 93 and Ref. 94.

4.1 Substrate preparation

All substrates were ordered from the supplier CrysTec (Berlin) with a 0.1° miscut with respect to the ideal $(001)_c$-orientation. STO and the REScO₃ substrates were treated in different ways prior to film deposition.
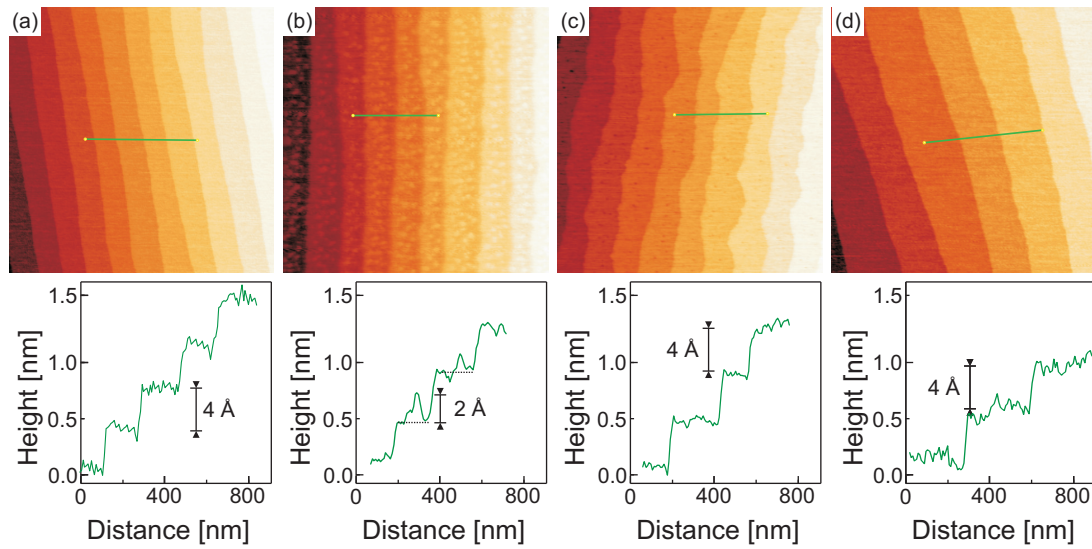
Figure 4.1: Substrate morphology with a corresponding scan line acquired by tapping mode AFM after pre-deposition treatment for (a) STO, (b) DSO, (c) GSO and (d) SSO. All images are $2 \times 2\,\mu m^2$.

The STO substrates were first etched in a buffered hydrofluoric acid solution[1] and subsequently annealed in air at 950°C for 2h. The treatment was reported to yield single terminated TiO$_2$ surfaces, by a reaction of the SrO-termination in water forming Sr-hydroxide complexes, which are solvable in the acid [95, 96]. Figure 4.1(a) shows the morphology of an STO substrate after the treatment, acquired by tapping mode AFM. The surface is atomically flat with terraces of approximately 200 nm in width and steps of one unit cell in height, indicating a single termination. The terraces are a result of the miscut vicinal substrate and their width is in agreement with the expected value $w \approx 4\,\text{Å}/\tan 0.1° \approx 200\,\text{nm}$.

The REScO$_3$ substrates were annealed for two hours in air without any wet etching step before. Different temperatures ranging from 975°C to 1200°C were tested for DSO, attaining similar results. The obtained morphology varies from substrate to substrate, even for the same parameters. Either results similar to the STO substrate were obtained, or some additional islands on top of the terraces formed with a height less than one unit cell, as depicted in Fig. 4.1(b). The half unit cell steps suggest that there are different terminations on the DSO substrate surface. However, for both kinds of morphologies, even for completely flat terraces, it has been reported that mixed terminations are present on DSO substrates after annealing [97]. Nevertheless, here, no influence of the surface morphology on the subsequent growth and domain formation of BFO could be observed. The GSO and SSO substrates were annealed at 1100°C and 1200°C, respectively. The morphology of the GSO varied, similarly to the one of DSO (e.g. completely flat terraces in Fig. 4.1(c)), whereas for SSO always completely flat terraces were obtained (Fig. 4.1(d)). For the SSO substrates, the terrace width varied more than for the other substrates, because of a limited availability of the 0.1° miscut crystals from the supplier.

Part of the DSO substrates were annealed in O$_2$ atmosphere at 1200°C for three hours, which was reported to alter the surface termination [98]. Compared to an Ar atmosphere,

---

[1]First the substrate was soaked in distilled H$_2$O for $\approx 1\,\text{min}$, then dipped for 15 s in 50 ml H$_2$O, 1.5 ml NH$_4$F, 0.5 ml HF.
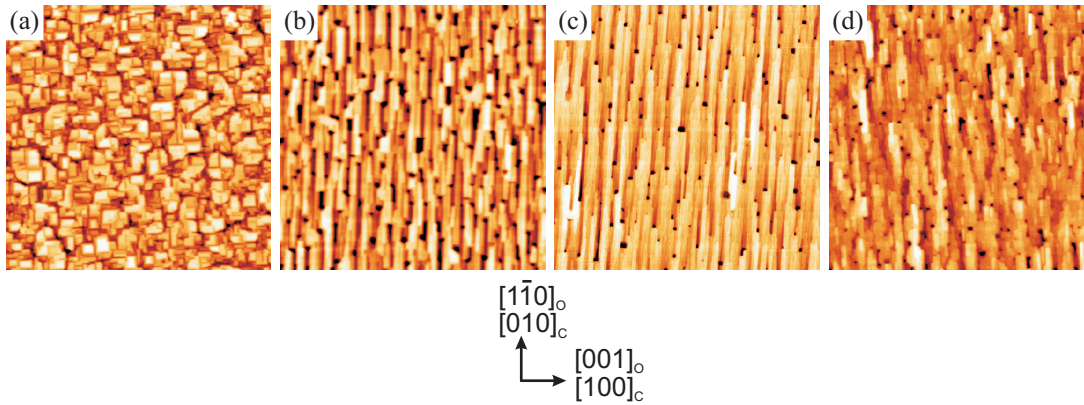
Figure 4.2: AFM surface morphology (acquired in tapping mode) of 26 nm thick BFO films deposited on (a) STO(001)$_c$ (color scale: 9 nm, rms: 2.0 nm), (b) DSO(110)$_o$ (color scale: 11 nm, rms: 2.7 nm), (c) GSO(110)$_o$ (color scale: 4 nm, rms: 1.0 nm) and (d) SSO(110)$_o$ (color scale: 7 nm, rms: 1.7 nm). All images are $4 \times 4\,\mu m^2$.

in O$_2$ atmosphere a higher amount of DyO$^+$-termination is expected [98]. The obtained surface morphology is similar to the standard annealing procedure and is not shown here.

4.2 BiFeO$_3$ films grown directly on the substrate

This section describes the domain formation of BFO films grown directly on the substrates STO(001)$_c$, DSO(110)$_o$, GSO(110)$_o$ and SSO(110)$_o$. First, in Sec. 4.2.1, it will be shown that the substrate symmetry influences the domain formation. Then, in Sec. 4.2.2, it is shown that the substrate termination plays an important role as well.

4.2.1 Influence of the type of substrate on the domains in BiFeO$_3$ films

In this section, the domain formation of BFO films with thicknesses up to 38 nm are discussed, which were grown on STO(001)$_c$, DSO(110)$_o$, GSO(110)$_o$ and SSO(110)$_o$. The substrates were treated by annealing in air prior to film deposition, as described in Sec. 4.1. The morphology of the 26 nm thick BFO films are shown in Fig. 4.2. For all films a 3D growth is observed. In case of STO substrate the BFO films formed squarish islands (Fig. 4.2(a)), whereas for all REScO$_3$ substrates the BFO films formed elongated islands or stripes (Fig. 4.2(b)-4.2(d)). In all films the structures are aligned parallel to the substrate crystal axis. For the REScO$_3$ substrates, the BFO stripe direction is always parallel to the $[1\bar{1}0]_o$ axis.

A good epitaxial orientation and phase purity can be inferred by $2\Theta/\omega$-scans. A zoom to the fourth order is shown in Fig. 4.3(a). It can be seen that the BFO peak position moves to higher 2Θ values for bigger substrate lattice constants, which corresponds to a smaller out-of-plane lattice constant of BFO. The values determined by the Nelson-Riley method are listed in Tab. 4.1 and plotted against the epitaxial strain in Fig. 4.3(b). For the BFO film on GSO substrate only a rough estimation can be given, since due to the close lattice mismatch between BFO and GSO, the BFO film peak is hidden in the GSO substrate peak of much higher intensity. In can be seen in the plot in Fig. 4.3(b) that

(a)

(b)
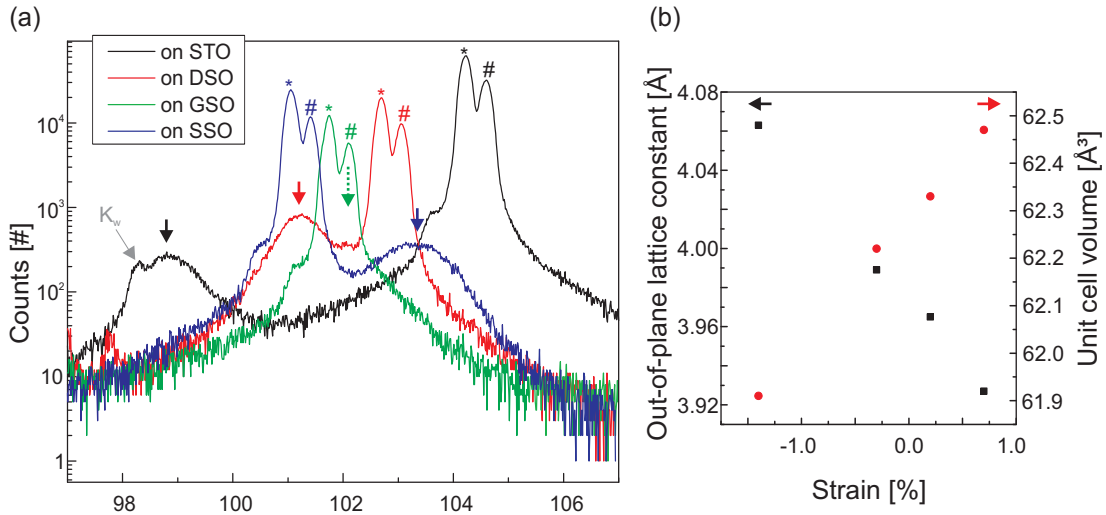
Figure 4.3: (a) $2\Theta/\omega$-scan around the $(004)_c$ peak of 26 nm thick BFO films grown directly on the substrates STO, DSO, GSO, SSO. The $K_{\alpha 1}$ and $K_{\alpha 2}$ peaks of the substrate are labeled by "$\star$" and "#", respectively. The BFO peak is indicated by an arrow. (b) Dependence of out-of-plane lattice constant of BFO (■) and pseudocubic unit cell volume (●) on the misfit.

Substrate	a_{sub} [Å]	c_{BFO} [Å]	V_{BFO} [Å³]
STO	3.905	4.063	61.91
DSO	3.949	3.989	62.22
GSO	3.968	≈ 3.965	≈ 62.33
SSO	3.987	3.927	62.47

Table 4.1: List of pseudocubic out-of-plane parameter of 26 nm thick BFO films grown directly on the substrates extracted from the $2\Theta/\omega$-scans by the Nelson-Riley method [85]. On the basis of the substrate in-plane parameter the pseudocubic unit cell volume of BFO is calculated.

the out-of-plane lattice constant is linearly dependent on the misfit, indicating an elastic deformation, as reported before [99]. In addition, the pseudocubic unit cell volume was calculated with the assumption that the BFO film is completely strained and adapts the in-plane lattice constant of the substrate, which will be shown in RSMs further down. Over the investigated range from $-1.4\,\%$ strain to $+0.7\,\%$ strain a slight unit cell expansion of $\approx 0.8\,\%$ takes place.

In order to visualize the ferroelectric domains, PFM was employed on all films. As described in Sec. 3.2.1.2, PFM measurements with two different cantilever orientations are necessary for a univocal determination of the polarization variant. Here, this has not been done at the exact same location, but at different spots on the sample. Nevertheless, it will be shown that this is sufficient here to determine the type of domain variants present in the film.

Fig. 4.4(a) shows the PFM image for the BFO film on $STO(001)_c$. Measurement with cantilever orientations parallel to $[100]_c$ and parallel to $[010]_c$ were performed. Both orientations give similar domain patterns, and just one orientation is shown here. The VPFM
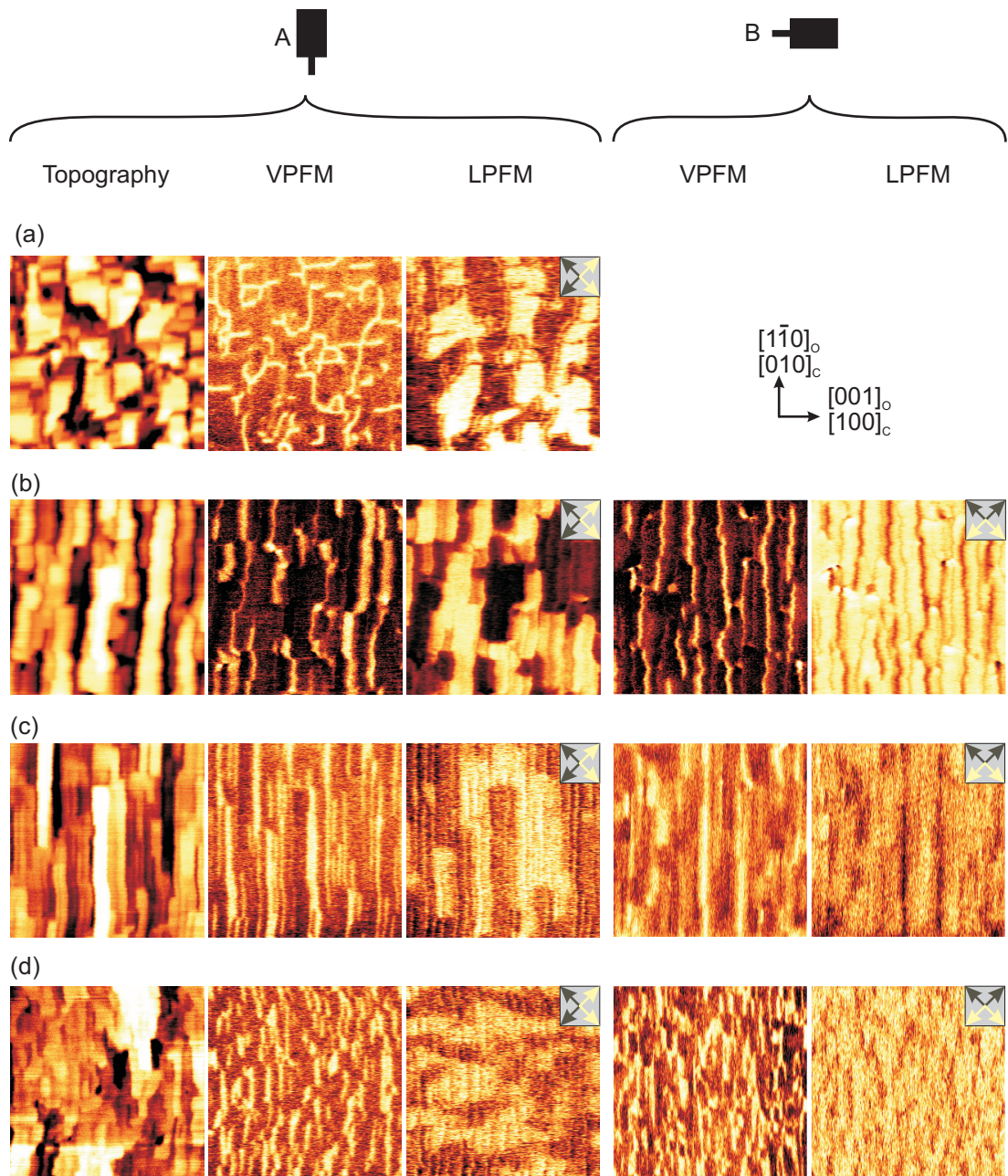
Figure 4.4: Topography, VPFM and LPFM images acquired for two different cantilever orientations A and B of $26\,nm$ thick BFO films without SRO bottom electrode grown on (a) STO, (b) DSO, (c) GSO and (d) SSO. All images are $1 \times 1\,\mu m^2$.
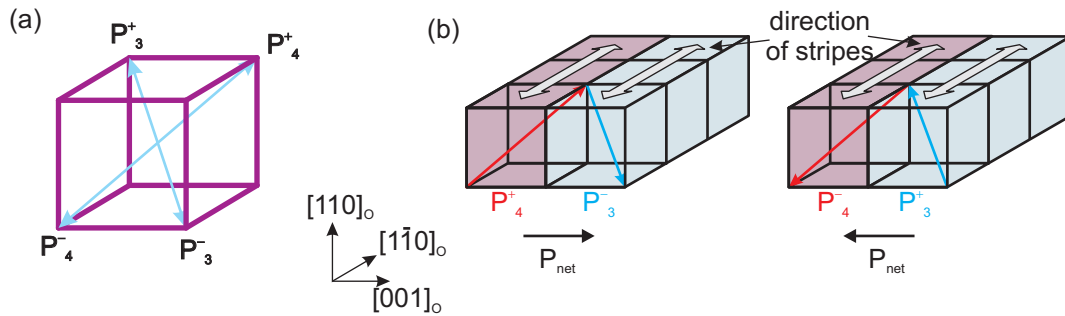
Figure 4.5: (a) Scheme of the four occurring polarization variants for BFO films grown on the REScO$_3$. (b) The two possible 109° stripe domain patterns built up by the structural variants r_3 and r_4.

images reveal that almost for the complete film the out-of-plane projection of the polarization points upwards (dark contrast), away from the substrate interface. The LPFM images show for both cantilever orientations evenly distributed contrasts. As a result, all four polarization variants which have an out-of-plane projection of the polarization pointing upward (P_1^+, P_2^+, P_3^+ and P_4^+) exist evenly in the film. Often, the topographic features match the lateral domain pattern, meaning that many islands are monodomain. There are a few lines though, which have an out-of-plane projection of the polarization pointing downwards (white contrast). These lines match almost always domain walls seen in LPFM, but they only appear for originally tail-to-tail domain walls. The result is a rather complex domain configuration at these lines, which is not considered here in detail.

A completely different domain pattern occurs for BFO films on the REScO$_3$ substrates. The situation is very similar for all three substrates, independent of the compressive and tensile strain. The PFM measurements of the BFO film on DSO, GSO and SSO are shown in Figs. 4.4(b-d), respectively. As can be seen for instance in case of DSO substrate in Fig. 4.4(b), the vertical PFM consists of stripes, which are aligned in the same way as the stripes in morphology. If the cantilever is aligned perpendicular to the stripes, i.e. parallel to $[001]_o$ (orientation B), the LPFM pattern is identical to the VPFM pattern, unless with inverted color contrast. From this it follows that where the out-of-plane projection of the polarization is pointing upwards, the in-plane projection of the polarization is pointing along the $[1\bar{1}0]_o$ axis, and vice versa for a projection downwards (there it has an in-plane projection along $-[1\bar{1}0]_o$). In other words, from the measurement with cantilever orientation parallel to $[001]_o$ it can be concluded that in all BFO films on REScO$_3$ substrates there exist only the polarization variants P_3^+, P_3^-, P_4^+ and P_4^- (see Fig. 4.5(a)), and therefore only the structural variants r_3 and r_4. In case the cantilever is rotated by 90°, i.e. parallel to $[1\bar{1}0]_o$ (orientation A), the domain configuration seen in LPFM changes to a pattern with patches. Although the image was acquired at a different spot on the sample than the one for orientation B, the exact domain pattern can be deduced from orientation A, since the domain configuration for an orientation B at the exact same location can be deduced from the VPFM image. Combining all information it follows that within one patch seen in LPFM with orientation A the stripes form 109° domain boundaries. For a bright contrast a patch consists of a stripe sequence with P_3^- and P_4^+ variants and a net in-plane polarization that is pointing towards $[001]_o$, whereas for a black contrast the patch consists of a stripe sequence with P_3^+ and P_4^-

and the net in-plane polarization is pointing towards $-[001]_o$ (see Fig. 4.5(b)). Domain boundaries of the patches seen in LPFM with orientation A can either be 180°, in case they coincide with domain boundaries in the VPFM, or 71° otherwise.

The PFM images of tensile strained BFO films on GSO and SSO (Fig. 4.4(c) and 4.4(d)) reveal that in principle the same domain patterns as for DSO substrate formed, however the stripe width is considerably smaller. Whereas for DSO the average stripe periodicity is about $\approx 140\,\text{nm}$, in case of GSO and SSO the stripes are much finer, some of them even smaller than $10\,\text{nm}$. These domain sizes are at the border of PFM resolution [80]. As a result, not all details can be resolved and the PFM contrast is weaker than for BFO films on DSO. To circumvent the resolution limit of PFM and to get a more detailed view of the domain patterns TEM investigations were employed. With the here available TEMs, one is mainly restricted to the observation of ferroelastic domains, 180° domains can therefore not easily be visualized, however the lateral resolution is orders of magnitudes higher. A plan-view specimen was prepared of the $26\,\text{nm}$ thick BFO film and a cross section specimen was prepared of a $38\,\text{nm}$ thick BFO film, both grown on $SSO(110)_o$. As can be seen in Fig. 4.6(a), the stripes are clearly visible by plan-view TEM and match in size with those seen by PFM. The stripes end with a needle like shape and merge alternatingly at angles of $\pm 45°$ with respect to the stripe direction. The average stripe width is 10-15 nm, but there are as well stripes with less than $5\,\text{nm}$ in width. The corresponding diffraction pattern, depicted in Fig. 4.6(b), shows the typical (pseudo)-cubic diffraction pattern and confirms the epitaxial growth of the BFO film. The cross section dark field TEM image shown in Fig. 4.6(c) reveals vertical domain boundaries as well as 45° tilted domain walls. As discussed in Sec. 2.3.1, from theoretical considerations the 109° domain walls are expected to be vertical, whereas for 71° domain walls a tilt angle of 45° is predicted. Therefore the vertical domain wall can be assigned to the 109° stripe domains and the 45° tilted domain walls either to the needle like ending of the stripes or to walls where two patches meet which are seen in LPFM with cantilever orientation A. Figure 4.6(d) is a HRTEM image of two 109° domain walls with the interface to the DSO substrate. No defects, such as misfit dislocations, were visible under these measurement conditions, neither for the domain wall nor for the interface between BFO and SSO substrate.

As a summary of the PFM and TEM measurements so far, the $28\,\text{nm}$ thick BFO films on STO substrate form islands with all structural variants occurring, with a preferred out-of-plane polarization component pointing upwards. Further, the BFO film on the $REScO_3$ substrates form 109° stripe domains, consisting of only two structural variants r_3 and r_4. From the theoretical considerations by Streiffer *et al.* [50], which are presented in Sec. 2.3.1, eight different energetically favorable domain patterns can occur. However, for BFO on STO none of these formed, whereas on the $REScO_3$ only one of the eight possible stripe patterns formed.

The reason that none of the predicted domain patterns form in BFO on STO substrate may be explained by the film morphology, which consists of relatively high islands. Each island is usually monodomain and the domain walls are placed at the groves between two islands. Hence, the domain wall energy is reduced, just because the volume of the domain wall is reduced. As a result, the domain wall energy is not sufficient to be the dominant mechanism for the domain pattern formation, but it is energetically more favorable to have each island as one single domain. Due to symmetry reasons on the cubic substrate each structural variant is equally likely. On the other hand, the interface may impose the out-of-plane polarization component. Assuming a valence mismatch at the interface,
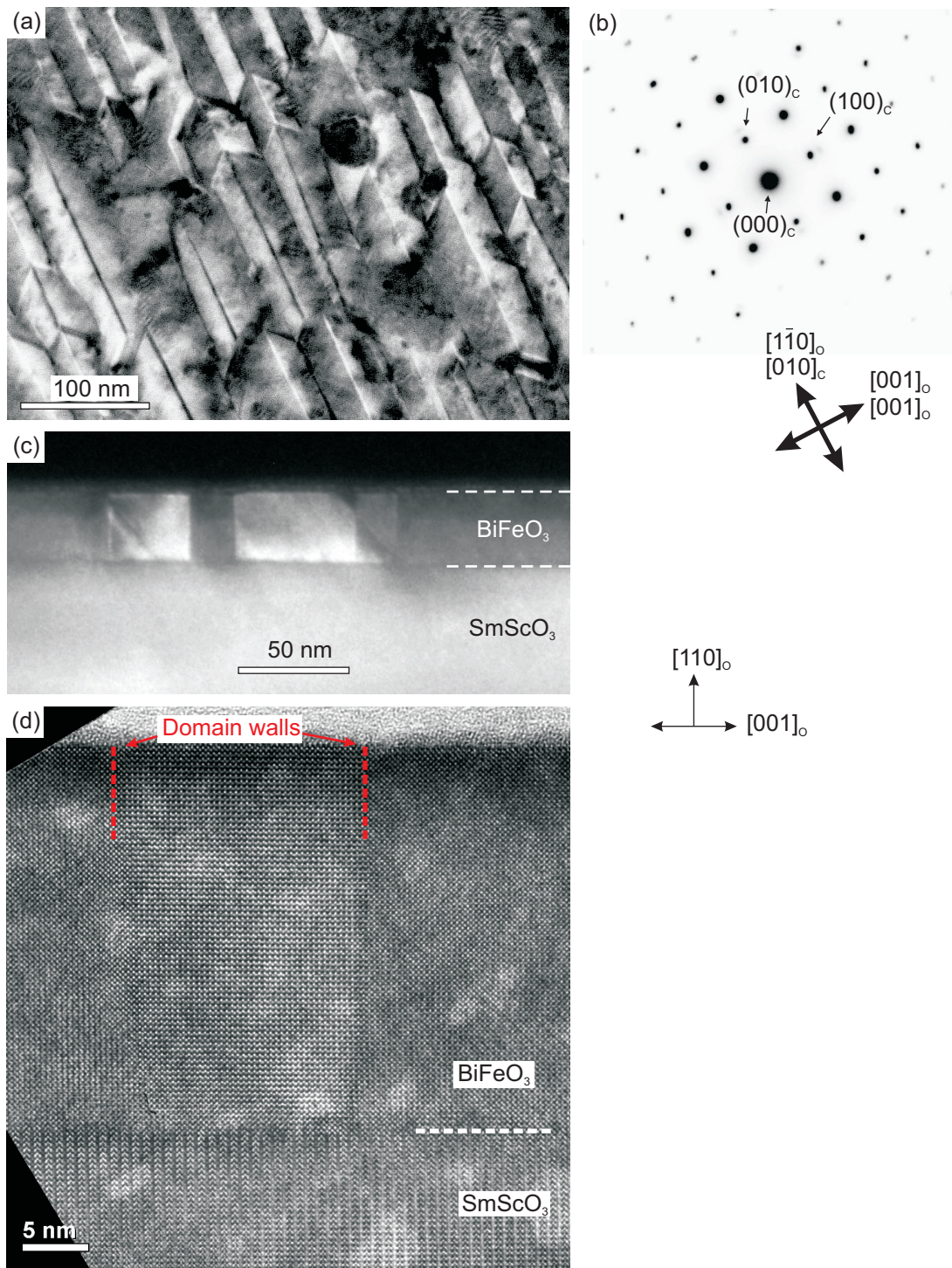
Figure 4.6: (a) Bright field plan-view TEM image along $[110]_o$ zone axis of a 26 nm thick BFO film grown on SSO(110)$_o$ and (b) its corresponding diffraction pattern. (c) Dark field TEM cross section image of 38 nm thick BFO film on SSO a few degrees out from $[1\bar{1}0]_o$ zone axis to enhance domain contrast and (d) HRTEM image showing two 109° domain boundaries in the BFO film.
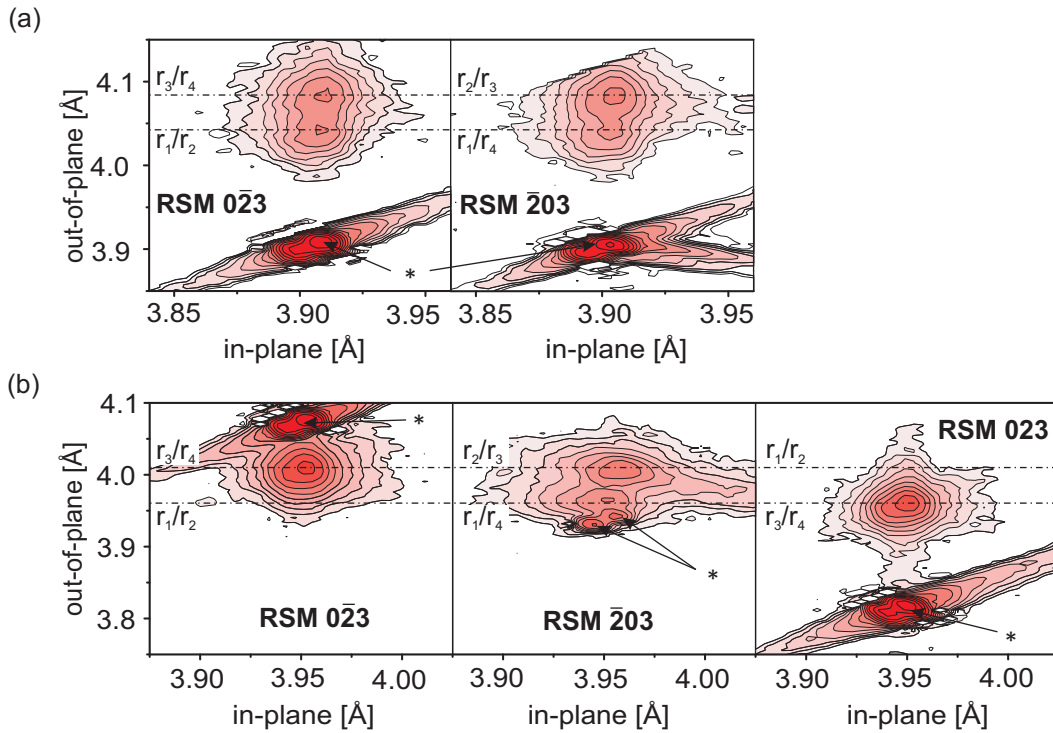
Figure 4.7: XRD-RSMs for a BFO film on (a) $STO(001)_c$ around $(0\bar{2}3)_c$ and $(\bar{2}03)_c$, and on (b) DSO around $(0\bar{2}3)_c$, $(\bar{2}03)_c$ and $(023)_c$. The substrate peaks are labeled with $(\star)$. All RSMs are displayed in logarithmic color code.

similar to the polar discontinuity model [100], a *B*-site termination of $SrTiO_3$ inflicts a polarization pointing upwards on BFO [89], which is in agreement with our observations.

The rare earth scandate substrates impose 109° domain patterns on the BFO films, which consist of only two structural variants. Without any electrical compensation at the interface, the 109° domain patterns are energetically more favorable in thin films than the 71° domain patterns, because a polarization pointing alternating up and down reduces the depolarization field [101]. The formation of 109° and 71° domain patterns will be discussed in more detail in Sec. 4.2.2. Still, there are four different 109° stripe domain patterns possible, however, just one of these occurs in BFO films on $REScO_3$ substrates. Often the slightly different in-plane lattice parameters, or the different in-plane thermal expansion coefficients of the $REScO_3$ substrates are given as origin of the stripe selection [91]. However, by symmetry arguments this effect might impose the directions of the stripes, but not the exact structural variants and therefore leaving two possible 109° domain patterns. In addition, for DSO, GSO and SSO the lower in-plane misfit is along the $(001)_o$ direction (see Tab. 2.1), whereas for $TbScO_3(110)_o$ substrate the lower in-plane misfit is along $(1\bar{1}0)_o$ direction [91]. Nevertheless, BFO films on all substrates form stripes along the $[1\bar{1}0]_o$ direction. Therefore it is unlikely, that the two different in-plane lattice constants are the origin of the particular stripe formation. Here, a different origin is proposed, which will be explained by XRD measurements in the following.

Figure 4.7(a) shows RSM measurements of the BFO film on STO substrate around the $(0\bar{2}3)_c$ and $(\bar{2}03)_c$ reflections of STO. As described in Sec. 3.2.2, the extracted out-of-plane parameter from RSMs is related to the distance of the planes under investigation

35
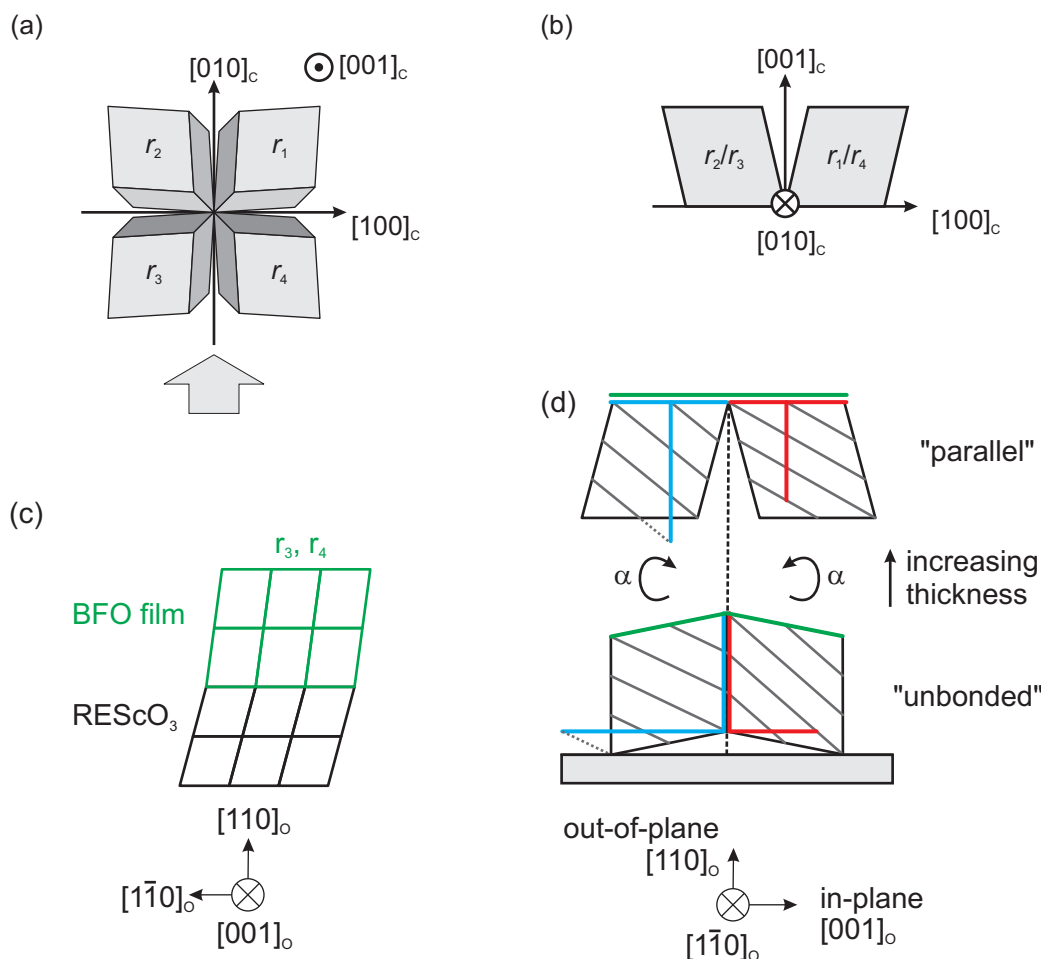
Figure 4.8: (a) The four possible ferroelastic variants seen in top view. For XRD-RSM measured around $(203)_c$ or $(\bar{2}03)$ the projection along the $[010]_c$ direction is of importance, which is indicated by the arrow in (a) and shown as projection with exaggerated distortion in (b). The structural variants r_2/r_3 and r_1/r_4 have the same projection and are therefore indistinguishable by XRD-RSM around these peaks. (c) Schematics of the orientation of the structural variants of BFO with respect to the REScO$_3$ substrates. (d) Schematics of the unit cell rotation with increasing thickness for tensile in-plane strained BFO films on GSO and SSO. The $(203)_c$ planes (gray lines) and the extracted in-plane and out-of-plane lattice constants shown for both structural variants (red and blue lines, respectively) lead to a transition from a vertical to horizontal peak splitting in the RSMs. The green lines show the orientation of the $(004)_c$ planes in both cases.

along the $(001)_c$ direction and the extracted in-plane parameter from RSMs is related to the distance of planes along the appropriate in-plane projection (e.g. for RSM around $(203)_c$ along $(100)_c$). For cubic materials the cubic lattice constant can be extracted. Both RSMs in Fig. 4.7(a) yield 3.905 Å for the STO substrate, in agreement with values reported in literature. In case of RSMs of BFO around $\{\bar{2}03\}_c$, the projection of the structural variant onto the corresponding plane is of importance. For instance, in case of RSMs around $(203)_c$ or $(\bar{2}03)_c$ the projection onto the $(010)_c$ plane is essential. Here, the four structural variants (Fig. 4.8(a)) are seen as two pairs, r_2/r_3 and r_1/r_4 (Fig. 4.8(b)). As a result, by XRD the two pairs can be distinguished, but the two variants within one pair can not be resolved. Both pairs have different out-of-plane parameters, due to their

monoclinic projection, as discussed in Sec. 3.2.2. For BFO on STO both RSMs around $(0\bar{2}3)_c$ and $(\bar{2}03)_c$ show a peak splitting, which is in agreement with the observations from PFM that all structural variants occur in the film.

The BFO films on REScO₃ have all similar behavior. The RSM in case of BFO on DSO is shown in Fig. 4.7(b). First, it should be mentioned that the DSO substrate has different out-of-plane lattice parameters for the three shown RSMs $(0\bar{2}3)_c$, $(\bar{2}03)_c$ and $(023)_c$, which is a result of the monoclinic distorted pseudocubic unit cell. As described in Sec. 3.2.2, the direction of distortion can be determined from the extracted out-of-plane lattice parameters. Depending on the investigated peak, the BFO film exhibits one or two peaks. This is in agreement with the PFM investigations that only r_3 and r_4 are present in the film. With respect to the DSO substrate, which holds for all BFO films on REScO₃ substrates as well, the selected variants of BFO are those which adapt the monoclinic distortion of the substrate, as depicted in Fig. 4.8(c). This can be seen from the fact, that BFO exhibits the larger out-of-plane lattice constant for the RSM around $(0\bar{2}3)_c$, for which the DSO substrate shows the large out-of-plane lattice constant as well. Vice versa, both materials show a small out-of-plane lattice constant for the RSM around $(023)_c$. Since the monoclinic distortion of DSO is along the $[100]_c$ axis, but the BFO distortion is along one diagonal, there are two equally good matching distortions, namely r_3 and r_4.

One explanation why the BFO wants to adapt the monoclinic distortion of the substrate might lie in the required oxygen octahedron connectivity at the interface between substrate and film [102, 103]. Due to the different symmetry of BFO and the REScO₃, both materials have different oxygen octahedron rotations. However, at the interface they have to share oxygen atoms. The variants r_3 and r_4 may fit better to the oxygen rotation of the substrate at the interface.

The tensile strained BFO films on GSO and SSO show an additional film thickness dependent effect. Figure 4.9(a-f) shows RSMs around $(203)_c$ of BFO films on SSO. The BFO film on GSO has the same behavior and is not shown here. Films with thickness 13 nm, 26 nm and 38 nm were investigated and the data is shown in two ways: (1) $\Theta - \omega$ versus 2Θ in Fig. 4.9(a-c) and (2) converted to in-plane and out-of-plane parameters in Fig. 4.9(d-f). From the first representation the plane spacing can be deduced from the 2Θ value and the tilt of the planes with respect to the sample surface from $(\Theta - \omega)$. As already mentioned, the second representation allows to decompose the plane spacing into one part perpendicular to the sample surface and one part parallel to the sample surface. In can be seen from the first representation that the BFO films have the same 2Θ value for all thicknesses, so the $(203)_c$ plane spacing stays constant. However, there is a transition in the $(\Theta - \omega)$ position, i.e. the tilt angle with respect to the sample surface, with increasing thickness visible. Starting from the 13 nm thick film (Fig. 4.9(a)), in the additional layers the two structural variants rotate in opposite directions. The RSM of BFO film with 38 nm thickness (Fig. 4.9(c)) forms reflections with maximum intensity at different $(\Theta - \omega)$ values, however the different orientation of the first layers is still visible as tail. The 26 nm thick BFO film (Fig. 4.9(b)) is in the middle of the transition with no pronounced peak at none of the two positions.

On the other hand, from the second representation it can be seen that the two structural variants start from an in-plane (horizontal) peak splitting for the 13 nm thick film (Fig. 4.9(d)) and end up with an out-of-plane peak splitting for the 38 nm thick film (Fig. 4.9(f)). This means that in the first layers the two structural variants (≤ 13 nm) have the same $(203)_c$ plane spacing projected out-of-plane. Then, there is a transition
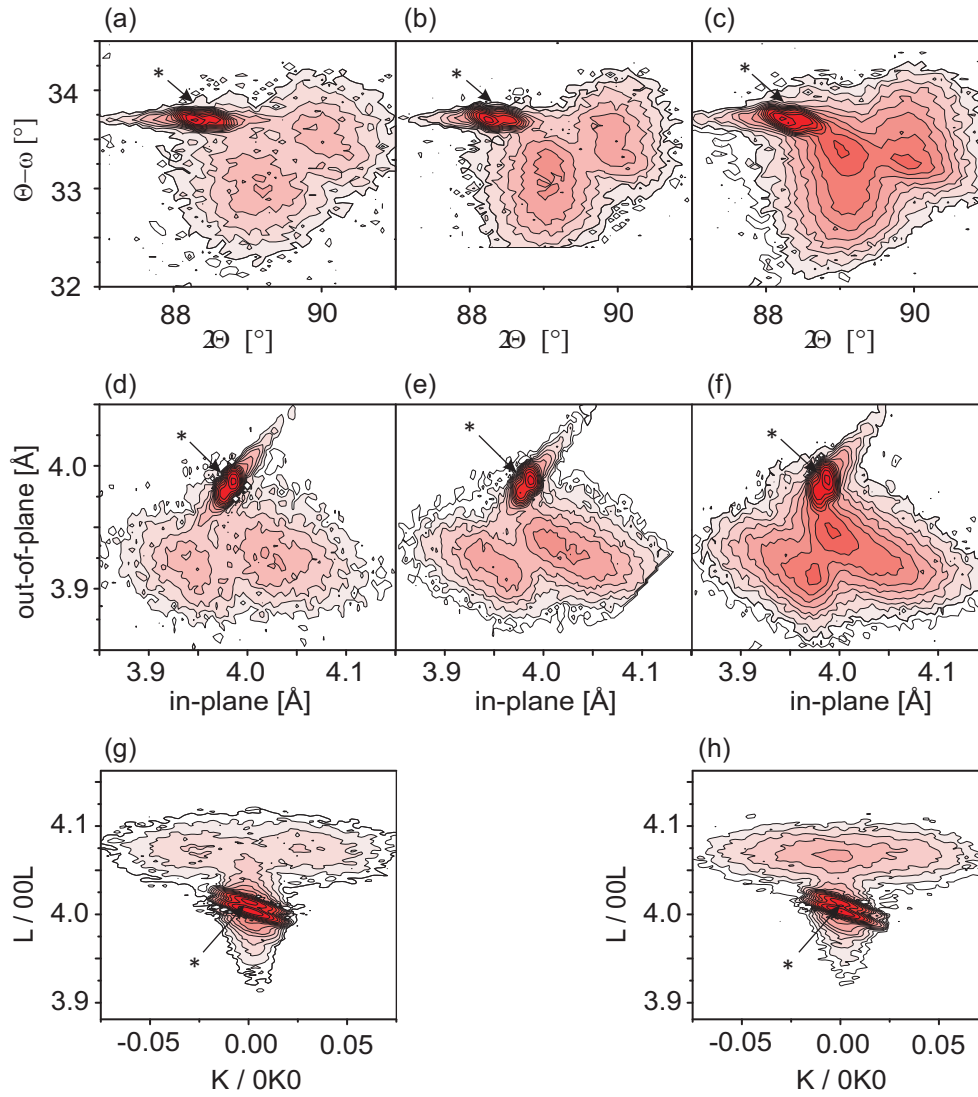
Figure 4.9: XRD-RSMs around $(203)_c$ of BFO films grown on $SSO(110)_o$. Films with three different thicknesses were measured: (a,d) 13 nm, (b,e) 26 nm and (c,f) 38 nm. The data are shown in two ways, (a-c) $\Theta - \omega$ versus 2Θ, and (d-f) transformed into lattice parameters. XRD-RSM around $(004)_c$ for the same BFO films of (g) 13 nm and (h) 38 nm thickness. The K and L axes are the Miller indices in pseudocubic notation for the SSO substrate and are parallel to the in-plane and out-of-plane direction of the sample surface. The substrate peaks in all RSM are labeled with ($\star$). All RSMs are displayed in logarithmic color code.

to a $(203)_c$ plane spacing for layers > 26 nm with equal in-plane projection. A possible explanation of this observation is depicted in Fig. 4.8(d). Starting from an "unbonded" orientation for the first layers, for which the two structural variants have an identical out-of-plane projection for the $(203)_c$ planes, the unit cell rotates with increasing film thickness to a "parallel" alignment with respect to the sample surface. A further evidence is given by the angle of rotation α, which is about 0.3° to 0.4° and matches exactly the rhombohedral distortion of BFO in projection onto the $(010)_c$ plane seen by the XRD measurement.

Also, RSMs around (004)$_c$ were performed. For a "unbonded" configuration a peak splitting is expected as seen in Fig. 4.8(d), for the "parallel" configuration on the other hand no peak splitting should be observed. As can be seen in Fig. 4.9(g) for the 13 nm thick BFO film and in Fig. 4.9(h) for the 36 nm thick BFO film, the measurements are in agreement with this consideration.

All the mentioned arguments speak for a rotation of the unit cell with increasing thickness for tensile strained BFO films on GSO and SSO as sketched in Fig. 4.8(d).

4.2.2 Influence of DyScO$_3$ substrate termination on the domains in BiFeO$_3$ films

In Sec. 4.2.1 it was shown that BFO films grown on DSO substrates, which were annealed in air prior to film deposition, form 109° stripe domains consisting of the structural variants r_3 and r_4. In this chapter it is shown that the domain pattern of the BFO film can be changed by a different annealing procedure of the DSO substrate, which is likely to result in a different surface termination.

Figure 4.10(a-c) shows the topography, VPFM and LPFM image of a 50 nm thick BFO film on DSO substrate which was annealed in O$_2$ atmosphere as described in Sec. 4.1. The images were acquired with a cantilever orientation parallel to [110]$_c$, which was here advantageous for domain visualization. The surface morphology (Fig. 4.10(a)) consists of stripes aligned along the [1$\bar{1}$0]$_o$ axis and is very similar to the surface morphology of the BFO film grown on DSO substrates annealed in air (Fig. 4.2(b)). The domain pattern, however, is very different. In VPFM (Fig. 4.10(b)) an almost uniform black contrast is visible, just interrupted by a few short bright segments aligned parallel to the [1$\bar{1}$0]$_o$ axis, along with the topographic features. The faint stripes aligned along [001]$_o$ are coming from in-plane buckling crosstalk and should not be considered. On the other hand, the LPFM image (Fig. 4.10(c)) reveals stripes along [001]$_o$, perpendicular to the features in topography. The stripes have an alternating bright and gray contrast. Measurements with a different cantilever orientation allowed the assignment of the gray contrast as depicted in the inset of Fig. 4.10(c). Combining all information, it can be deduced that 71° stripe domains formed, consisting of P_3^+ and P_4^+ polarization variants, with a net polarization pointing out-of-plane upwards and in-plane towards [$\bar{1}$10]$_o$. The small white segments seen in VPFM are 109° stripes, which are identical to the 109° stripes on DSO substrates annealed in air.

XRD-RSMs of the same BFO film around (024)$_c$ in Fig. 4.10(d) and around (204)$_c$ in Fig. 4.10(e) confirm that only the two structural variants r_3 and r_4 are present in the BFO film. These are the exactly same structural variants as for BFO films on DSO substrate annealed in air (compare with Fig. 4.7(b)). This is in agreement with the theoretical considerations of Streiffer *et al.* [50], who predicted that 109° stripe domains and 71° stripe domains, which are built up from the same structural variants, are aligned perpendicular to each other (see Fig. 2.7).

Therefore, in both cases (the DSO substrate annealed in air and the one annealed in O$_2$ atmosphere) the substrate symmetry imposes the structural variants r_3 and r_4 onto the BFO film. The reason for this is, as discussed in Sec. 4.2.1, the monoclinic distortion of the pseudocube, or rather the full orthorhombic symmetry of DSO. As already mentioned, one possible explanation might be the oxygen octahedron connectivity [102, 103].
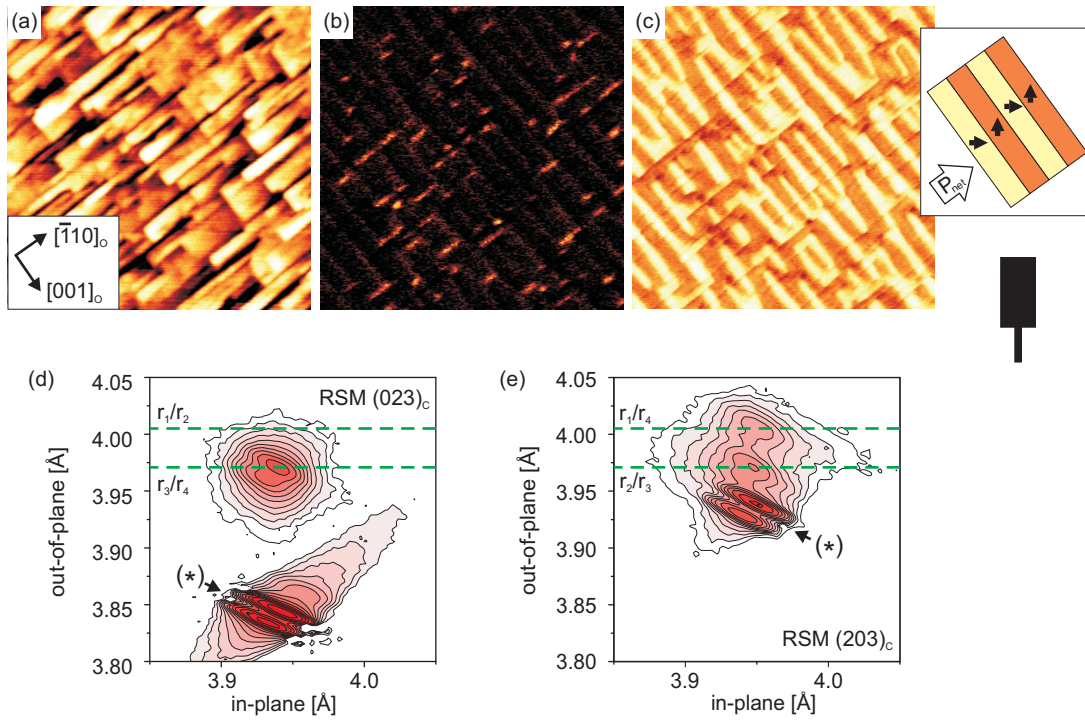
Figure 4.10: (a) Topography, (b) VPFM and (c) LPFM images of 50 nm thick BFO deposited on DSO(110)$_o$ substrate pretreated by annealing in O$_2$ atmosphere. All images are $8 \times 8\ \mu m^2$. The cantilever orientation is shown schematically on the right hand side. The inset in (c) shows the in-plane projection of the polarization variants with the net in-plane polarization direction. XRD-RSMs of the same film around (d) peak (024)$_c$ and (e) peak (204)$_c$. The substrate peaks are labeled with ($\star$). All RSMs are shown in logarithmic color scale.

On the other hand, the different annealing procedure of the DSO substrate prior to deposition leads to different stripe formations. The formation of 71° and 109° domain patterns compete against each other and the energetically more favorable pattern will form [101, 104]. Huenag *et al.* [101] reported, that the energies which play a role consist of three parts, the energy F_w for the domain wall itself, the elastic energy F_e due to the different structural variants and the depolarization field energy F_d. In general, it has been reported that there is crossover from 71° to 109° domains with increasing thickness. A strong influence on the crossover is given by the depolarization energy F_d [101].

Furthermore, the interface between the BFO film and the substrate or bottom electrode can influence the depolarization field [89, 105]. Yu *et al.* [89] reported, that an interfacial valence mismatch influences the potential step across the interface and successively the ferroelectric polarization direction. Therefore, the interface properties and their influence on the depolarization field should be included in the calculation by Huang *et al.* [101].

Here, the different annealing procedure of DSO substrate drives the BFO film across a transition from 109° to 71° domains. The termination of DSO could not be determined by the tools available; drawing a reliable conclusion is therefore difficult. It has been reported though, that sole annealing does not lead to a single surface termination [97, 106]. However, with respect to the valence mismatch model of Yu *et al.* [89], both terminations, DyO$^+$ and ScO$_2^-$, have no valence mismatch with BFO and should therefore not induce any out-of-plane polarization. These terminations might therefore induce the

109° stripe domains, since this pattern has no net out-of-plane polarization component (see Fig. 2.7(e)). On the other hand, other reports claim [98], that annealing in O$_2$ atmosphere can lead to evaporation of Dy$^-$ and O^{2-}, resulting in non-stoichiometric surfaces, as well as oxidation of Dy$^+$ to Dy^{2+}, which both might lead consequently to a preferred polarization upwards within the model of valence mismatch. The 71° stripe domain patterns have a net out-of-plane component (see Fig. 2.7(f)), and the 71° stripes domains on the DSO substrate annealed in O$_2$ atmosphere seen here have a net out-of-plane polarization component upwards, in agreement with this consideration.

4.3 BiFeO$_3$ films grown on SrRuO$_3$ buffered substrate

In Sec. 4.2 the domain formation of BFO films deposited directly on the substrate was discussed. In this chapter, the domain formation of BFO films which are grown on SRO buffered substrates is examined. It is shown that the conductive bottom electrode SRO, which is needed in case plane-parallel capacitors shall be formed, has a strong influence on the film growth and domain formation. First, in Sec. 4.3.1 the growth of the SRO layer on the discussed substrates is considered. Then in Sec. 4.3.2, the BFO domain formation on these SRO buffered substrates is discussed. Two different thickness regimes are considered: first thin films of ≈ 25 nm thickness for comparison with the BFO films grown directly on the substrates, followed by thicker films of ≈ 150 nm, which are more favorable for plane-parallel capacitors.

4.3.1 Growth of SrRuO$_3$ bottom electrode

In case plane-parallel capacitors with epitaxial BFO in-between shall be formed, first a high quality epitaxial bottom electrode has to be grown on the substrate, followed by the BFO film growth. Because of its relatively close lattice match and its good electrical properties (see Sec. 2.3.3), SRO is chosen here. In this section the surface morphology of the SRO grown on all four used substrates (STO(001)$_c$, DSO(110)$_o$, GSO(110)$_o$, and SSO(110)$_o$) is investigated. The BFO/SRO samples discussed in the following sections are however grown *in situ*, without checking the SRO surface morphology in between, to achieve the best possible interface between SRO and BFO. Here, investigations of single SRO layers grown with the same parameters as for the heterostructures are shown, allowing indirect conclusions on the heterostructures.

Figure 4.11 shows the surface morphology of SRO films grown with the parameters listed in Tab. 3.1. In case of STO and DSO substrate, Fig. 4.11(a) and 4.11(b), respectively, high quality SRO layers grown in step-flow-growth [107] were reproducibly achieved. The substrate terraces with one unit cell high steps are maintained in the SRO films. In case of GSO and SSO substrates, however, a worse surface morphology was observed, probably due to the high tensile lattice mismatch of +1.0% and +1.4%, respectively. In addition, different surface morphologies were obervered. In the best case the SRO layer on GSO shows still terraces (Fig. 4.11(c)), however, small islands start to form as well. In the worst case the terraces are primarily seen due to a scar of about 2 nm depth running along the direction of the substrate terraces (Fig. 4.11(e) and 4.11(f)). Even between two scars the SRO film is not flat, but shows a substructure with one or two unit cell high steps. For SRO on SSO, in the best case the SRO layer is quite flat (Fig. 4.11(d), rms: 0.63 nm), however, the terraces of the substrate are not visible
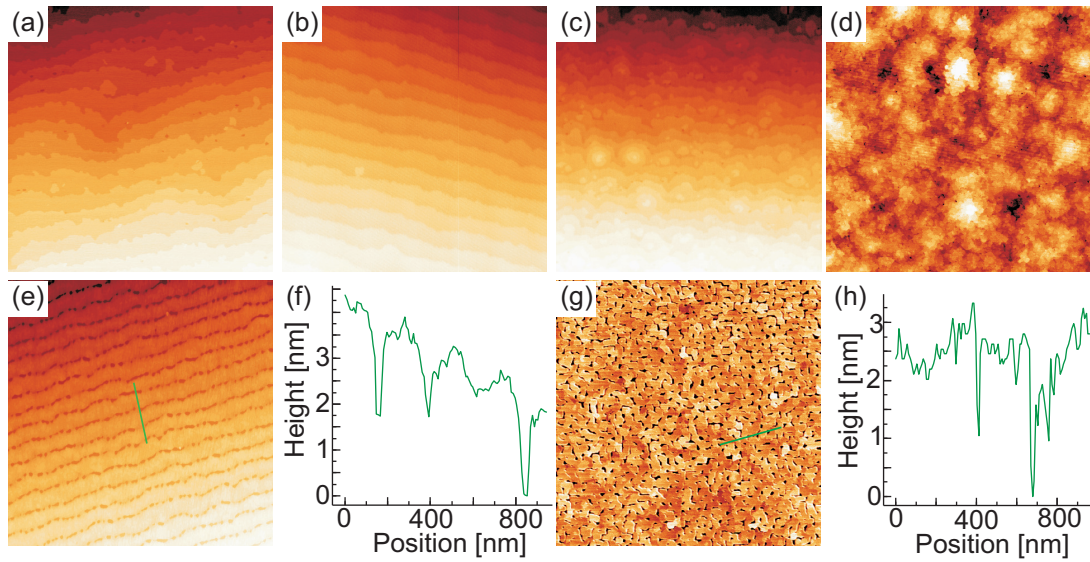
Figure 4.11: AFM topography images of a 50 nm thick SRO layer grown on (a) STO(001)$_c$, (b) DSO(110)$_o$, (c) GSO(110)$_o$, and (d) SSO(110)$_o$. Some SRO layers on GSO and SSO show a rougher morphology, e.g. (e) 50 nm thick SRO on GSO with (f) corresponding scan line, and (g) 10 nm thick SRO on SSO with (h) corresponding scan line. All images are $4 \times 4\,\mu m^2$.

anymore and many islands formed. Some films, especially thinner films, do not form a uniform film but bigger islands of 1-3 nm height.

XRD measurements, which are shown in the following sections, reveal that the 50 nm thick SRO films on STO and DSO substrates are fully strained. Particularly due to the good surface morphology, the SRO buffered STO and DSO substrates are good substrates for subsequent BFO deposition and investigation. On the other hand, XRD-RSMs of SRO films on GSO and SSO show that even thin SRO layers of 5-10 nm thickness start to relax. Together with the bad surface morphology the conclusions which can be drawn from BFO films grown on these buffered substrates are therefore limited.

4.3.2 BiFeO$_3$ domain formation on SrRuO$_3$ buffered substrates

4.3.2.1 Thin films ($\approx$25 nm)

BFO films of 25 nm thickness were grown on the SRO buffered substrates STO(001)$_c$, DSO(110)$_o$, GSO(110)$_o$ and SSO(110)$_o$. As discussed in the previous Sec. 4.3.1, in case of STO and DSO high-quality SRO layers were achieved, whereas on GSO and SSO the surface morphology of SRO consisted of islands. In addition, even for very thin layers ($\approx$ 5 nm) the SRO was already partly relaxed.

Figure 4.12(a-d) shows the surface morphology of the 25 nm thick BFO films on these substrates. Despite the bad surface morphology of the SRO films grown on GSO and SSO, the BFO films on all substrates are atomically flat and terraces are visible. On STO and DSO the terraces are very straight, for the films on GSO and SSO the terraces are rather ragged. Compared to the surface morphology of the BFO films grown directly on the substrate, it is obvious that a different growth mode occurred. While for the film directly on the substrate a 3D growth mode took place, in case of the SRO
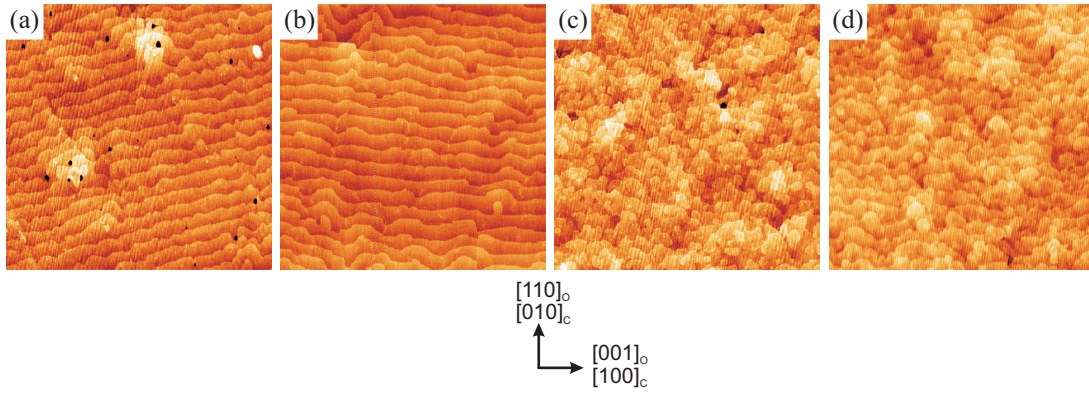
Figure 4.12: AFM surface morphology of 25 nm thick BFO film on SRO buffered (a) STO(001)$_c$, (b) DSO(110)$_o$ (c) GSO(110)$_o$ and (d) SSO(110)$_o$. All images are $4 \times 4\,\mu m^2$, the terraces seen correspond to one unit cell high steps.

buffered substrate the flat surface morphology suggests either a step-flow-growth mode or a layer-by-layer growth mode. A possible explanation for the different growth modes might be given by different surface diffusivities, more precisely a higher diffusivity in case of SRO buffered substrates. In case of step-flow-grown SRO the surface is A-site terminated [108], on the other hand the substrates have a dominantly B-site termination after their pre-treatment [96, 97]. In general, a higher surface diffusivity was measured for A-site terminated perovskites [108], which is in agreement with our observed BFO growth modes.

VPFM images on all BFO films reveal that they have a uniform out-of-plane component pointing downwards to the SRO bottom electrode, and are not shown here. This downwards out-of-plane direction of the polarization of BFO on SRO was reported often in literature [90, 92], and is explained either by a complete screening of the polarization by surface charge carriers in SRO [90] or by the valence mismatch model for A-site terminated SRO [89].

Figure 4.13 shows the LPFM images of the BFO films on the SRO buffered substrates for two different cantilever orientations, one with the cantilever parallel to the terraces, the other with the cantilever perpendicular to the terraces. The BFO films on SRO/STO and SRO/DSO show a similar behavior. For the cantilever perpendicular to the terraces, an evenly distributed bright and dark contrast occurs. Minor differences are that the domains on SRO/DSO are bigger than those on SRO/STO. For the cantilever oriented parallel to the terraces, however, both films exhibit more bright than dark contrast, which corresponds to a preferred projection of the polarization towards $[010]_c/[1\bar{1}0]_o$. This means, that preferentially the polarization variants P_3^- and P_4^- exist in the film (Fig. 4.13(e)). For the BFO films on SRO/GSO and SRO/SSO both cantilever orientations reveal mosaic-like domain patterns with evenly distributed contrasts. Therefore, all four polarization variants (P_1^-, P_2^-, P_3^-, and P_4^-) pointing downwards occur (Fig. 4.13(f)). The appearance of all polarization variants on GSO and SSO is expected though, because the bad SRO surface morphology on these substrates destroyed all possible symmetry reduction needed for a domain variant selection.

To further investigate the origin of the preferred domain variants on SRO buffered STO and SRO buffered DSO substrates, XRD-RSMs on these films were measured. The RSMs of BFO on SRO/STO around $\{203\}_c$ in Figure 4.14(a) show that the SRO has a
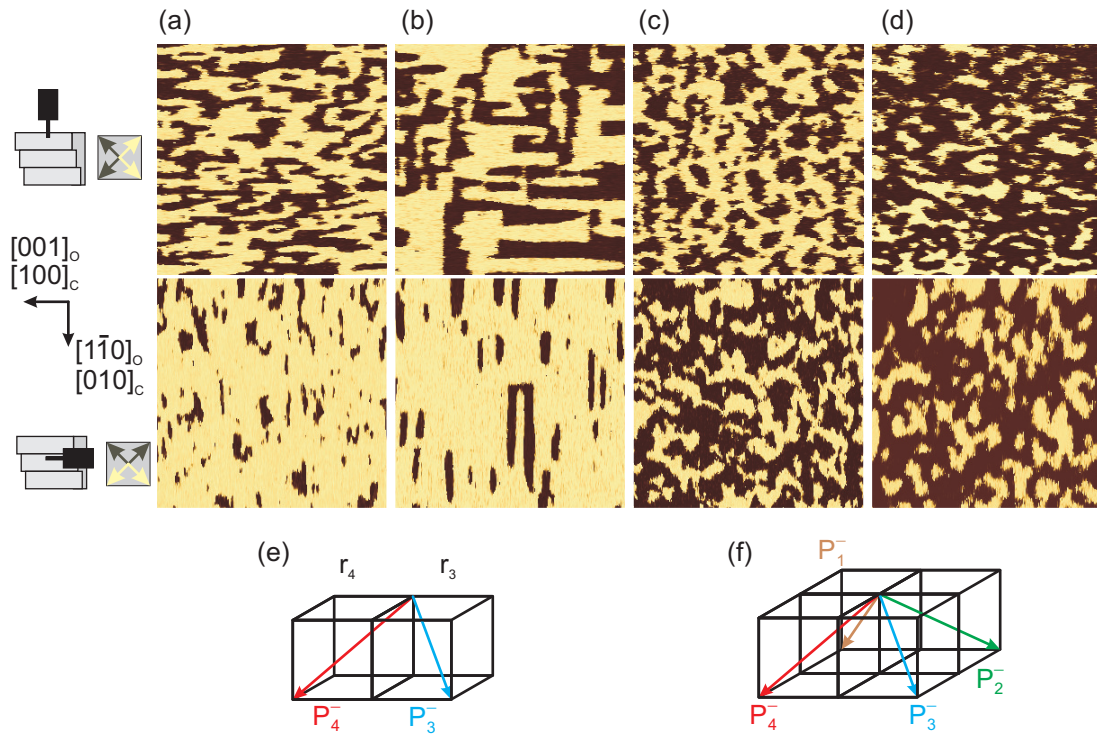
Figure 4.13: LPFM images with two different cantilever orientations for 25 nm thick BFO films on SRO buffered (a) STO, (b) DSO, (c) GSO and (d) SSO substrates. The drawing on the left hand side indicate the cantilever orientation with respect to the terraces. All images are $3 \times 3 \, \mu m^2$. Schematics for the preferred domain variants on (e) STO and DSO, as well as on (f) GSO and SSO.

monodomain orthorhombic structure (again with monoclinically distorted pseudocube), as reported in literature [109], and that the BFO film comprises preferentially the structural variants r_3 and r_4. The epitaxial orientation of SRO with respect to the STO substrate is determined by the miscut direction and the subsequent formation of terraces, which lowers the square symmetry of the STO surface. Already from the fact that there is nothing else for the cubic STO substrate which reduces the symmetry, apart from the terrace alignment, it can be concluded that the terraces are the origin of the preferred polarization variants in BFO, however, indirectly by controlling the SRO orientation. Figure 4.15(a) shows a corresponding schematics of the epitaxial orientation of the BFO/SRO/STO system.

Figure 4.14(b) shows the RSMs of BFO on SRO/DSO around $\{203\}_c$ and is in agreement with reports about a tetragonal symmetry of SRO on tensile straining substrate [59]. Again, the epitaxial orientation is determined by the terraces. Here, the orthorhombic symmetry of DSO (with the monoclinic distortion of the pseudocube), however, reduces the symmetry even further and might be an additional origin for the preferred domain variants. To check which of the two points is responsible for the preferred polarization variants on SRO/DSO, the BFO film with the same parameters was grown on a second SRO buffered DSO substrate, for which the DSO miscut angle was in the opposite direction (steps going downwards towards $[1\bar{1}0]_o$). In this case (not shown here) the preferential polarization variants changed to P_1^- and P_2^-, proving that the terrace alignment,
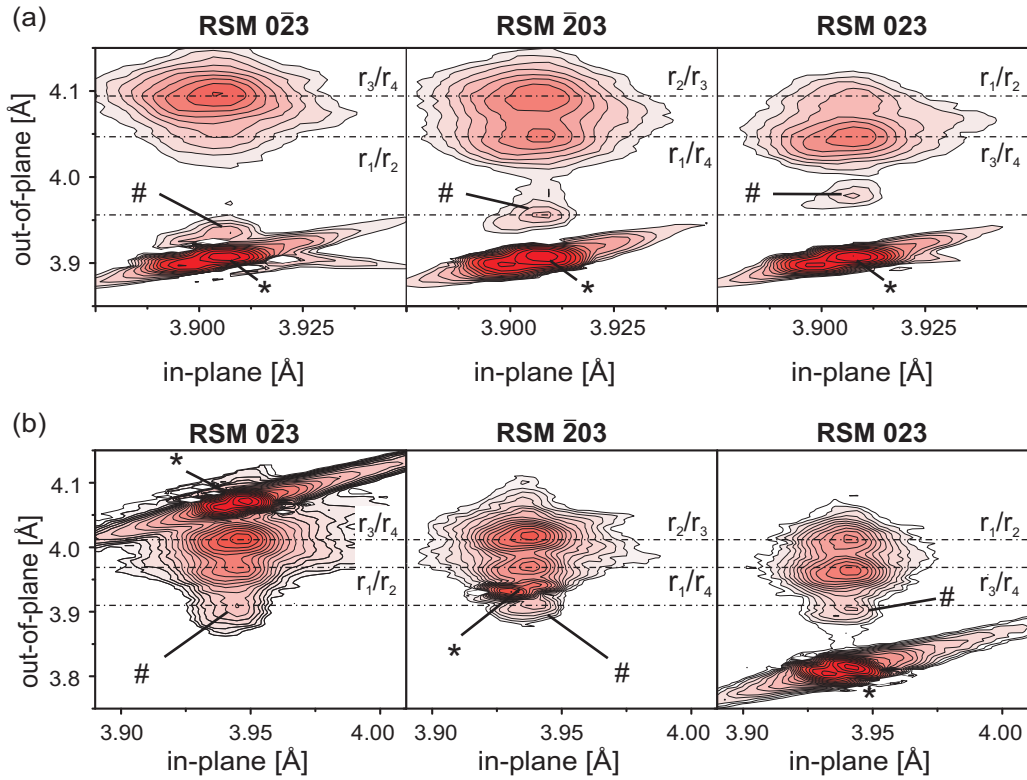
Figure 4.14: XRD-RSMs of 25 nm thick BFO film on (a) SRO/STO(001)$_c$ and (b) SRO/DSO(110)$_o$. The SRO layer is labeled with (#), the substrates are labeled with (⋆). All RSMs are displayed in logarithmic color scale.
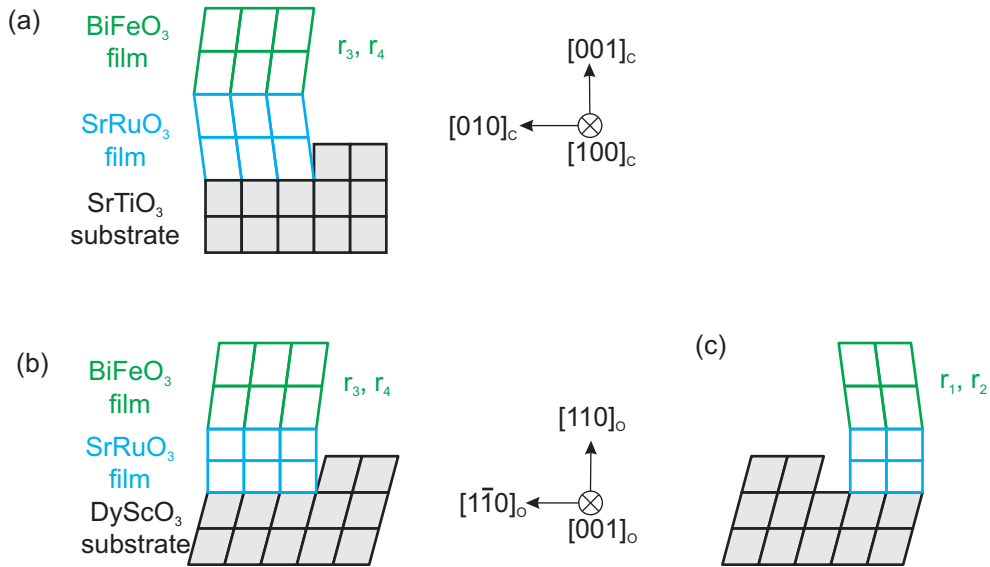
Figure 4.15: Schematics of the epitaxial orientation for thin (a) BFO/SRO/STO and for BFO/SRO/DSO with two different miscut directions (b) and (c).

and not the orthorhombic symmetry of DSO, is the origin of the chosen polarization variants (see Fig. 4.15(b) and 4.15(c)).

It should be noted, that a structural variant reduction induced by the substrate miscut has been reported already by Jang *et al.* [88]. In their case, however, STO(001)$_c$
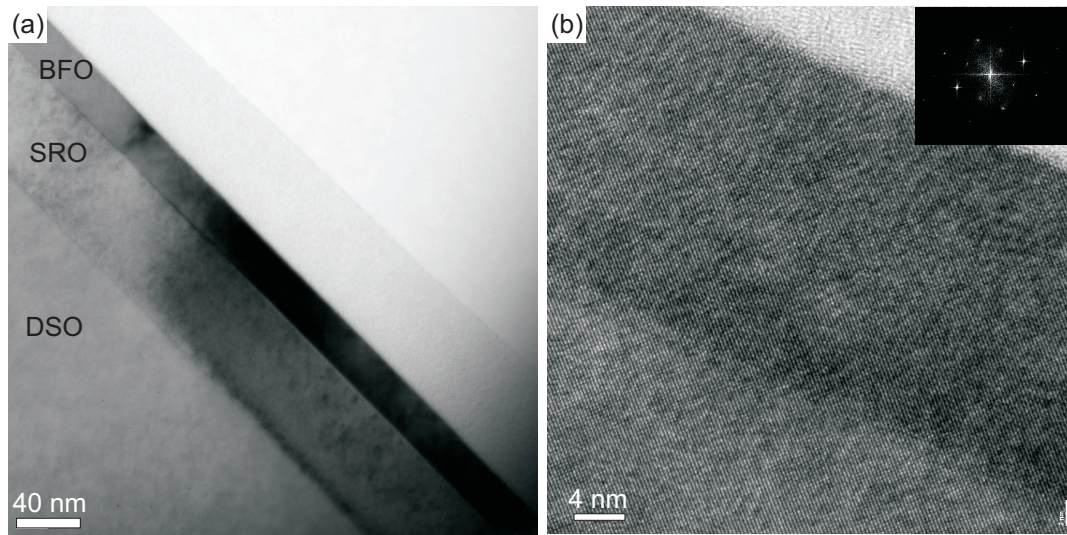
Figure 4.16: (a) TEM image of the 25 nm thick BFO/SRO/DSO film and (b) HRTEM image of the BFO film with BFO/SRO interface. The inset in (b) shows the fast Fourier transformation pattern, proving epitaxial growth.

substrates with high miscut angles of 4° were used, instead of the low miscut angles of 0.15° used here. The high miscut angle results in very low terrace widths of about 5-10 nm and in particular in terrace step bunching. Their suppressed structural variants are exactly opposite to the suppressed variants here. Therefore, a different mechanism has to be behind both cases. For high miscut substrates a variant selection because of mechanical restrictions at the step-bunched terraces is proposed, whereas here the epitaxial orientation of SRO seems to be crucial.

The RSMs in Fig. 4.14 show for both samples investigated here, BFO/SRO/STO and BFO/SRO/DSO, that the BFO and SRO layers are still completely strained and adopt the substrate in-plane lattice constant. TEM measurements acquired for the 25 nm thick BFO/SRO/DSO system are shown in Fig. 4.16(a,b), which prove the good film morphology and the good epitaxial quality of the sample (see FFT in inset). In the HRTEM image of the interface between BFO and SRO in Fig. 4.16(b) no defects, such as misfit dislocations, are visible. This is in agreement with the XRD measurements showing fully strained films.

Finally, macroscopic ferroelectric hysteresis measurements were performed to investigate in which respect the different epitaxial strain, the different domain patterns and the different structural variants may influence the electric characteristics of the BFO films. Amorphous SRO top electrodes covered with platinum ($60 \times 60\,\mu m^2$) were deposited on the 30 nm thick BFO films, except for the film on SSO substrate, where smaller amorphous platinum top electrodes were deposited ($12 \times 12\,\mu m^2$). The voltage was applied to the top electrode. Figure 4.17(a) and (b) show the ferroelectric polarization and switching current of BFO films on SRO buffered STO, DSO and GSO substrates. In agreement with other reports [41, 42], there is a slight decrease in ferroelectric polarization from negative to positive epitaxial in-plane strain, though it should be noted again that the BFO film on GSO is not fully strained. For the BFO film on SSO substrate, smaller electrodes had to be chosen, because of existing leaking paths for bigger electrodes. The drawback of the small electrode lies in the high relative error of the electrode area de-
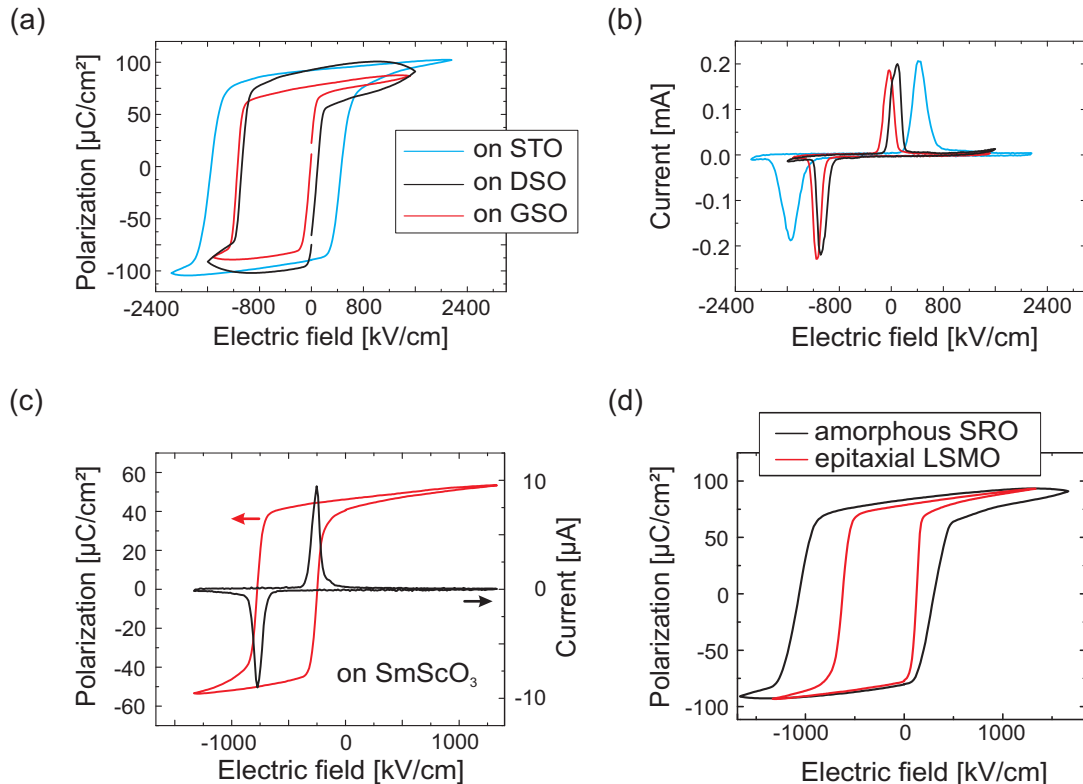
Figure 4.17: (a) Ferroelectric hysteresis loop and (b) its corresponding current for films on SRO buffered STO, DSO, and GSO substrates, measured at 100 K and 1 kHz with amorphous SRO top electrodes ($60 \times 60 \, \mu m^2$). (c) Ferroelectric polarization and corresponding current for BFO film on SSO substrate, measured at 100 K and 1 kHz with amorphous platinum top electrodes ($12 \times 12 \, \mu m^2$). (d) Ferroelectric polarization loop for BFO films on DSO substrate with $60 \times 60 \, \mu m^2$ amorphous SRO and epitaxial LSMO top electrodes, respectively, measured at 10 K and 1 kHz.

termination (even up to 25 %), which is a result of the fuzzy edge of the electrode from the sputtering procedure. Therefore, the data can not be compared reliably with the other films and are shown separately in Fig. 4.17(c). It can been said though, that the ferroelectric polarization is in the same order of magnitude. In addition, some reports claim that the occurrence of four structural variants may lead to domain wall pinning and subsequent lower switchable ferroelectric polarization [88, 110]. The measurements here show, that this does not hold in general and films with all structural variants can show good switching characteristics, since the BFO film on STO and DSO substrates with only two preferential structural variants, and the BFO film on GSO and SSO substrates with all four structural variants, exhibit no drastic difference in the ferroelectric polarization.

Furthermore, all films show a strong built-in field of about -550 kV/cm, called "imprint", which corresponds to -1.65 V. This electric field is aligned parallel to the as-grown out-of-plane polarization direction pointing towards the SRO bottom electrode. One origin of the imprint may be given with the help of the valence mismatch model [100]. For $(001)_c$ oriented perovskite materials ABO_3 the planes can be divided into alternating layers of AO and BO_2 (see Fig. 2.9), which have alternating net charges $\pm\rho$ so that the bulk material is neutral. If two materials with different net charges ρ form an interface,

a valence mismatch occurs which results in a voltage step at the interface. In the framework of this valence mismatch model, a voltage step across the BFO/SRO interface of $1.5 \pm 0.3\,\mathrm{V}$ was calculated [89], which may give rise to an internal field corresponding to $-0.75 \pm 0.18\,\mathrm{V}$ and may therefore contribute to the built-in field. In order to verify whether or not the top electrode influences this property as well, a BFO film on SRO buffered DSO substrate with epitaxial LSMO top electrode was grown for comparison. Figure 4.17(d) shows a direct comparison with amorphous SRO top electrode. It can be seen that the imprint is altered by approximately $140\,\mathrm{kV/cm}$ which corresponds to $0.4\,\mathrm{V}$. Even more evident is the considerably decreased coercive voltage. The interfacial properties play therefore an important role for both the imprint and the the coercive voltage.

Summarizing the domain formation of thin ($\approx 25\,\mathrm{nm}$) BFO films on SRO buffered substrates, it can be said that for this thickness regime the theoretical consideration about the domain wall compatibility of Streiffer *at al.* is not the driving mechanism, but it is the interfacial properties. First, the SRO layer induces either by its electrostatic properties [90] or due to the valence mismatch [89] a polarization pointing downwards. And second, on the one hand, the investigations on GSO and SSO substrates are limited, because of the mismatch between SRO and these substrates, leading to bad SRO surface morphologies. On the other hand, for STO and DSO substrate the epitaxial relationship of SRO to these substrate is given by the miscut direction of the substrates. Subsequently, either the SRO symmetry or the terraces in the SRO layer induced some preferred structural variants with mosaic-like domain patterns on both STO and DSO substrates in a very similar manner.

4.3.2.2 Thick films ($\approx$150 nm)

For the 25 nm thick BFO films on SRO buffered substrates discussed in the last section, the formed domains are imposed by the interface. The theoretically predicted 71° and 109° stripes [50] did not form, most probably because the domain wall compatibility was not dominant enough for the investigated thickness of 25 nm. To increase the importance of the domain walls, thicker films of 150 nm thickness were investigated here. However, only BFO films on SRO buffered STO and SRO buffered DSO were investigated, because of the good growth quality of the SRO on these two substrates.

Figure 4.18(a) and 4.18(d) show the surface morphology of 150 nm thick BFO films on SRO/DSO(110)$_\mathrm{o}$ and on SRO/STO(001)$_\mathrm{c}$, respectively. The morphology still reveals almost only one-unit-cell-high steps, however, the terraces do not run straight anymore and often bunch together as well. In addition, some holes of about 20 nm in depth are present in both films. As for the thinner films on SRO buffered substrates, the VPFM images in Fig. 4.18(b) and 4.18(e) reveal an out-of-plane polarization component pointing towards the SRO bottom electrode. Though for the here discussed thicker films, small domains with polarization up are visible. The LPFM images in Fig. 4.18(c) and 4.18(f) reveal stripes, which can be, together with the VPFM images, assigned to 71° stripe domains, similar to the BFO film deposited on O$_2$ annealed DSO substrates. The stripes run along the $[\bar{1}10]_\mathrm{o}$ direction for DSO and along the $[100]_\mathrm{c}$ direction for STO, which is in both cases again likely to occur because of the terrace alignment and the subsequent orientation of the SRO bottom layer. For DSO, regions where the net in-plane polarization points towards $[001]_\mathrm{o}$ (bright patterns) and regions where it points towards $[00\bar{1}]_\mathrm{o}$ (dark patterns) exist. Often, theses regions are divided by the stripes of opposite
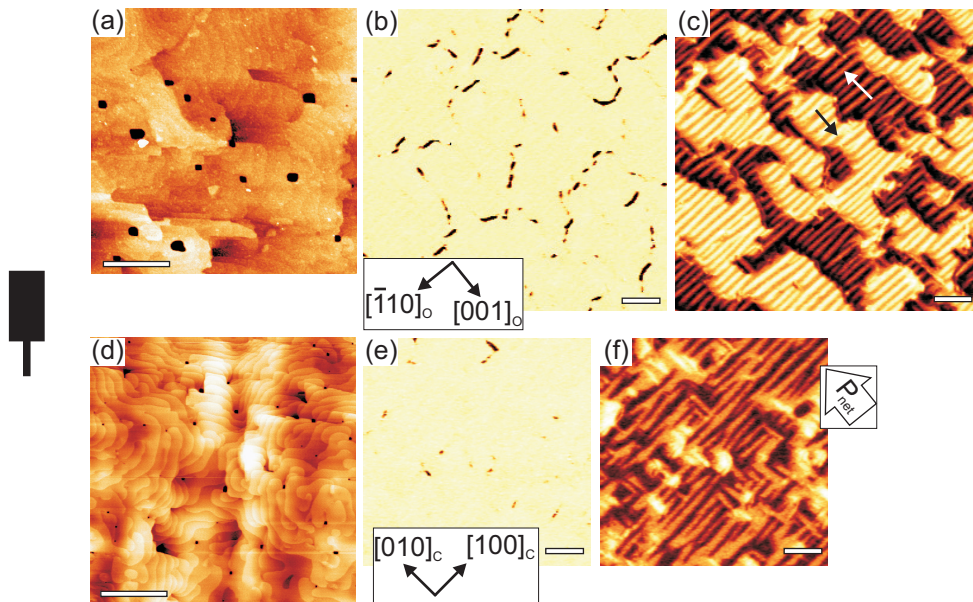
Figure 4.18: (a) AFM topography by tapping mode, (b) VPFM and (c) LPFM images of 150 nm thick BFO on SRO/DSO(110)$_o$. (d) AFM topography by tapping mode, (e) VPFM and (f) LPFM images of 150 nm thick BFO on SRO/STO(001)$_c$. The arrows in (c) indicate the direction of net in-plane polarization for the dark and bright regions. All scale bars are 1 μm. The cantilever orientation is shown schematically on the left hand side.
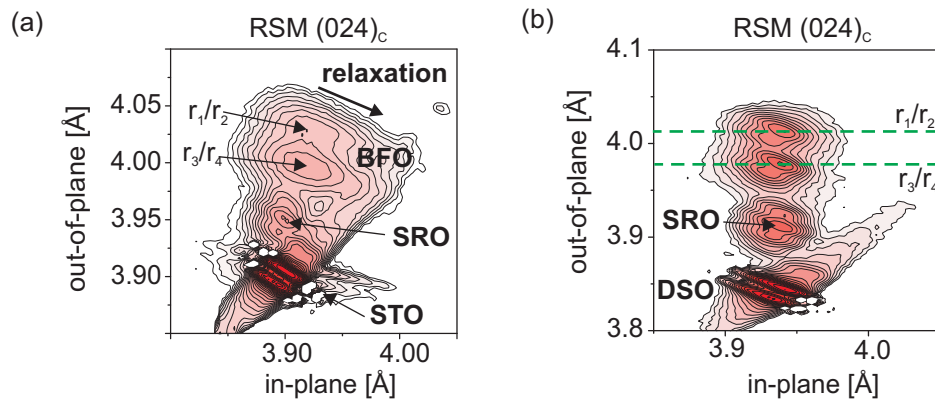
Figure 4.19: XRD-RSMs around (204)$_c$ for 150 nm thick BFO films on (a) SRO buffered STO and (b) SRO buffered DSO. All RSMs are displayed in logarithmic color scale.

out-of-plane polarization seen in VPFM. On the other hand, in case of STO, there is a preferential net in-plane polarization direction towards the [010]$_c$ direction. XRD-RSMs were performed to check the qualilty of the BFO films. It has been reported that the critical thickness for strain relaxation of BFO on STO is about 30 nm [111]. Therefore, at least for the BFO/SRO/STO sample a relaxation of the BFO film is expected. The RSM around (204)$_c$ of this film in Fig. 4.19(a) shows that the SRO is still strained with the same in-plane lattice parameter, however, for the BFO film a relaxation is visible, seen as a decrease of the out-of-plane lattice parameter and an increase of the in-plane lattice parameter, both developing towards the bulk BFO parameters. In contrast, the RSMs around (204)$_c$ of the BFO/SRO/DSO film in Fig. 4.19 shows that both SRO and BFO are completly strained, with the same in-plane lattice parameter as the DSO substrate. This

$(001)_c$

$(010)_c$

BFO

SRO

STO

50 nm
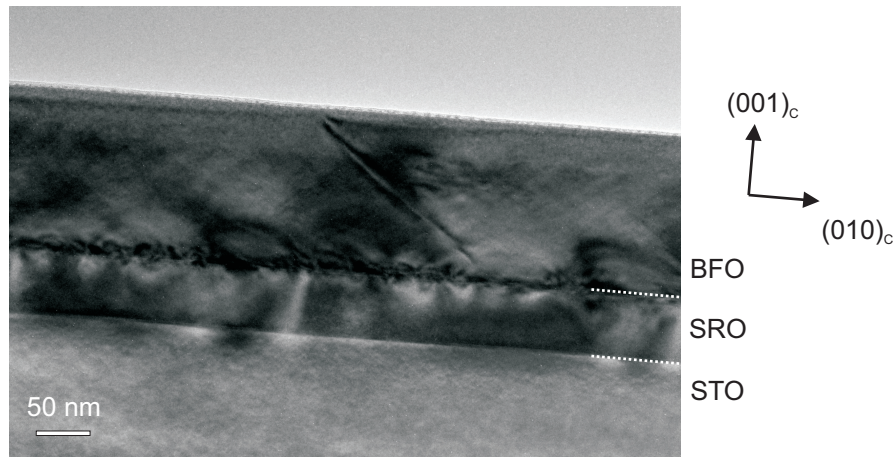
Figure 4.20: TEM image of thick BFO film on SRO buffered STO substrate.

(a)

(b)

(c)

$[100]_c$

$[010]_c$
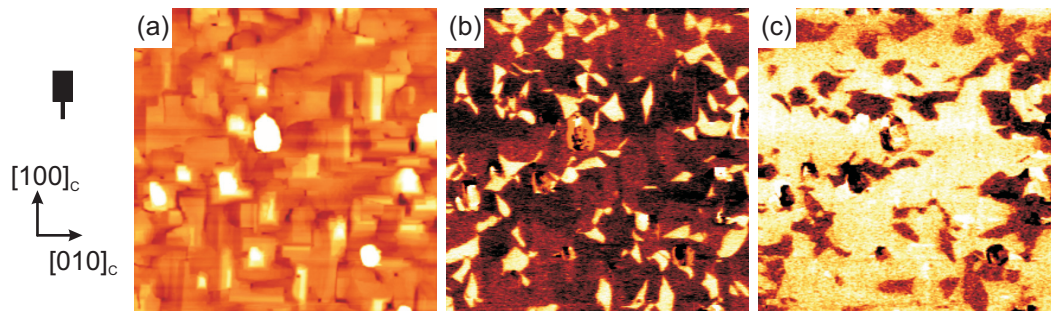
Figure 4.21: (a) Topography (color scale: 60 nm), (b) VPFM image, and (c) LPFM image of approximately 200 nm thick BFO film grown with high laser fluency on LSMO buffered STO. The orientation of the cantilever is sketched on the left side. All images are $7 \times 7\,\mu m^2$.

suggests, that the lower misfit of BFO with DSO allows to grow fully strained 150 nm thick BFO films.

Due to the net in-plane polarization direction for the BFO/SRO/STO sample, the structural variants r_3 and r_4 are preferred, seen as well in Fig. 4.19(a). On the other hand, since for the BFO/SRO/DSO sample both net in-plane polarization variants occur, all structural variants should be present equally, in agreement with Fig. 4.19(b).

Figure 4.20 shows a cross section TEM image of another 150 nm thick BFO film on SRO buffered STO substrate to get further insight into the structural quality of the film. A feature aligned 45° to the film normal is clearly visible, which can be assigned to a 71° domain boundary, which are expected to form $\{101\}_c$ boundaries. In addition, a periodic strain contrast with a spacing of less than about 20 nm is visible at the BFO/SRO interface. Since from XRD-RSMs a relaxation of the BFO film is seen, misfit dislocations at the SRO/BFO interface are expected and may therefore presumably be attributed to the visible features.

At last point it shall be noted, that the domain pattern in the BFO films shown here are rather stable for applied laser fluency in the range from 0.15 J/cm² to approximately 0.6 J/cm². For higher laser fluency there is a transition to an unordered domain pattern. Figure 4.21 gives an example for an approximately 200 nm thick BFO film grown with

a laser fluency of $0.83 \, \text{J/cm}^2$ on LSMO buffered STO substrate.[2] A mosaic-like domain pattern is seen in both the out-of-plane component of the polarization and the in-plane component of the polarization. The most likely explanation is, that so much material is deposited per laser pulse on the substrate that a transition to a 3D growth mode is introduced, as seen in the rough film morphology. In addition, the film and interface between BFO and bottom electrode are most probably more defective, which results among others in a mixture of upwards and downwards domains. Although the quality of these films is presumably worse than the films grown with lower laser fluency, for some investigations this domain configuration is advantageous and will be employed in Chapter 6.

4.4 Summary

In this section, the ferroelectric/ferroelastic domain formation of BFO films grown on $STO(001)_c$, $DSO(110)_o$, $GSO(110)_o$, and $SSO(110)_o$ substrates were discussed. It was shown, that the domain formation can depend on many factors: the growth mode of the film, the type of interface and its properties, the substrate symmetry, the substrate miscut direction, and the predicted domain wall compatibility by Streiffer *et al.* [50]. A schematic overview of the as-grown domain formations in the BFO thin films is given in Fig. 4.22 and will be summarized in detail in the following.

BFO films grown directly on the substrate were considered with film thicknesses $\leq 50 \, \text{nm}$. In case of STO substrate small islands formed in the BFO film, each of those consisting of just one polarization variant. The TiO_2 termination of the STO substrate imposes the out-of-plane component of the polarization pointing upwards. Due to the cubic symmetry of STO, all four polarization variants (P_1^+, P_2^+, P_3^+ and P_4^+), and therefore all four structural variants (r_1, r_2, r_3, and r_4) occur with equal amount.[3]

In case BFO is grown directly on the $REScO_3$ substrate a 3D growth mode is observed as well, however, two structural variants of BFO are fully suppressed and only the variants r_3 and r_4 form. So far reported only for compressively strained BFO films on DSO and $TbScO_3$ substrates, this variant selection happens as well for tensile strained BFO films on GSO and SSO. It is very robust and occurs for different substrate terminations and subsequent different domain patterns. Although reported in literature that the different in-plane parameters of the $REScO_3$ substrates are responsible for this effect, by symmetry considerations this property is not sufficient to select exactly one pair of structural variants from the four compatible pairs possible. Here, the monoclinic distortion of the pseudocubic unit cell of the $REScO_3$ substrate is proposed as origin, since this distortion reduces the symmetry enough so that the two structural variants may be selected. A possible mechanism behind might be the required oxygen octahedron connectivity at the interface.

With the structural variants r_3 and r_4, both 71° and 109° stripe domains can be formed. If the $REScO_3$ substrates are annealed in air prior to BFO film deposition, the BFO films on all $REScO_3$ substrates have 109° domain patterns. The 109° domain pattern has no net out-of-plane component of the polarization and thus might be energetically more

---

[2]The domain structure for BFO on LSMO buffered STO substrate with lower laser fluency is similar to the domain structure of BFO on SRO buffered STO, but it is not shown here.

[3]It should be noted though, that the structural variants can be reduced afterwards by an electric field for instance [112]
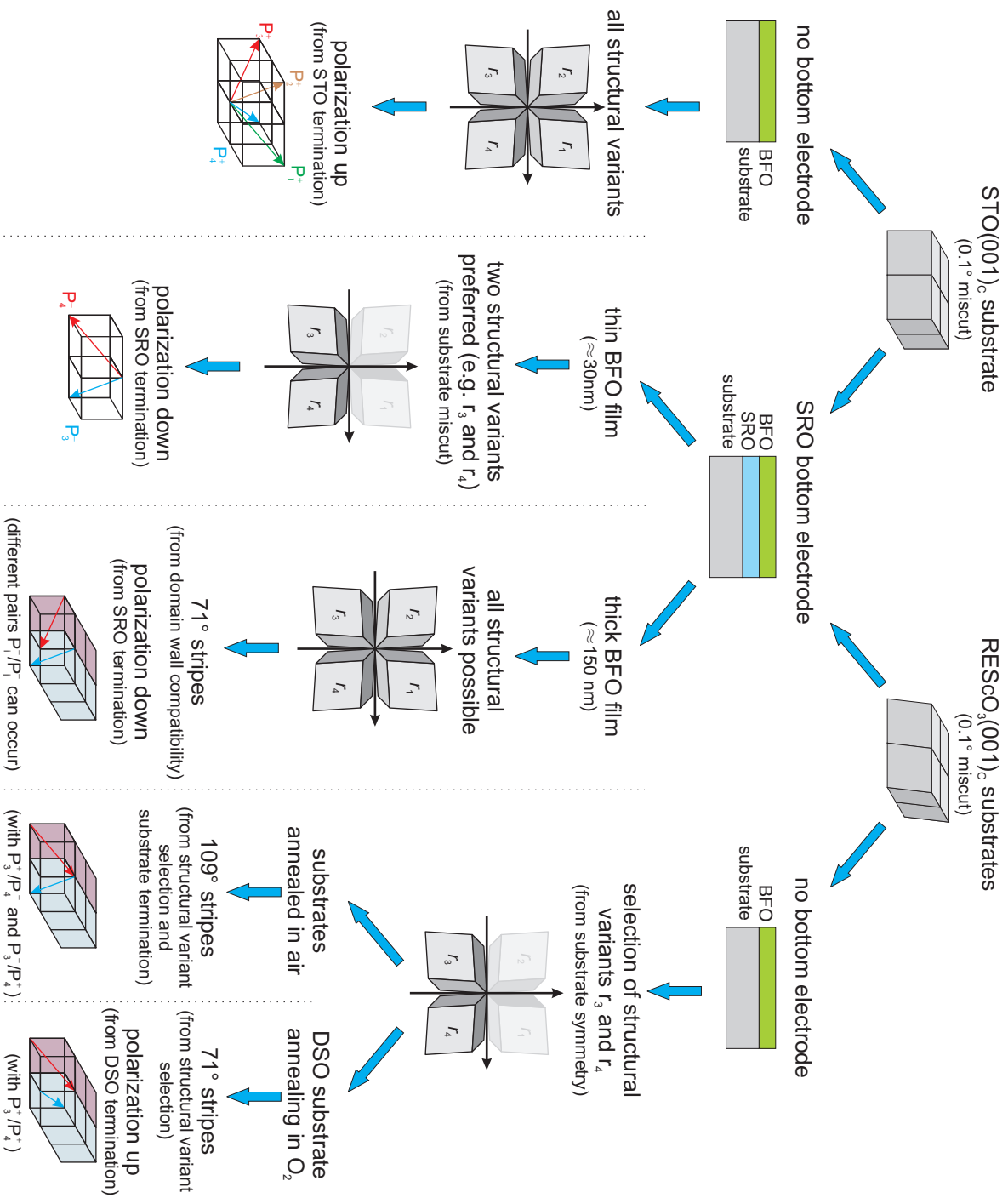
Figure 4.22: Schematic summary of the as-grown domain formation in the epitaxial BFO thin films investigated here.

favorable than the 71° domain pattern, if the depolarization field existent for the latter can not be compensated by the interfacial properties. For the tensile strained BFO films, an additional rotation of the unit cell with increasing thickness within the first 30 nm is observed. Starting from an "unbonded" configuration the unit cells rotate towards a parallel alignment. The angle of rotation extracted from the RSMs is equal to the distortion of the BFO pseudocubic unit cell and therefore is in perfect agreement with this model.

The BFO film grown on DSO substrate annealed in O_2 atmosphere prior to film deposition exhibits 71° domains with a net out-of-plane polarization pointing upwards, still built up by the structural variants r_3 and r_4. It has been reported that a different atmosphere during annealing of DSO can alter its surface termination. The exact surface termination of our DSO substrates could not be determined by our means of investigation tools, however, with respect to the valence mismatch model certain terminations would cause a polarization pointing upwards.

In case the substrates are buffered with a conductive SRO bottom electrode first, the growth mode of the BFO film grown on top changes to step-flow-growth or layer-by-layer growth, probably due to a different surface diffusivity on the A-site terminated SRO. All films have an out-of-plane polarization component pointing towards the SRO layer, which has been reported to come from either the valence mismatch or the polarization screening by surface charge carriers. Because of the large lattice mismatch between the SRO bottom electrode and the GSO and SSO substrate, the SRO on these substrate has a bad surface morphology and is as well partly relaxed. The BFO domain investigation on these films is therefore limited.

For thin BFO films (≤ 30 nm) on STO and DSO substrate the domain formation is dominated by the interfacial properties rather than the domain wall compatibility. The epitaxial relationship of SRO on these substrates is defined by the miscut direction. The BFO film has preferred (but not completely suppressed) structural variants, which are a consequence of either the SRO structural orientation or the terraces in the SRO morphology.

For thicker BFO films (≈ 150 nm) on SRO buffered STO and DSO the domain wall compatibility becomes more dominant and 71° stripe domains, still with an out-of-plane polarization component towards the SRO bottom electrode, form. Usually only one stripe direction occurs, which is again likely to happen because of the miscut direction of the substrates.

5

Stability of 71° stripe domains in BiFeO₃ thin films upon repeated electrical switching

The 71° stripe domain patterns of BFO have been reported to exhibit new functionalities, such as conductivity confined at the domain walls [9, 16] and an above-bandgap photovoltaic effect [11], which are not present in the surrounding bulk domains or rely on the special domain pattern. One of the most interesting findings was reported recently by Heron *et al.* [12], who demonstrated that by utilization of these 71° stripe domains of BFO the magnetization of a CoFe layer in a BFO/CoFe heterostructure can be reversed by an electric field at room temperature. For this reversal two effects are used: (i) The magnetization of the CoFe layer couples to the small net magnetization of BFO (see Sec. 2.3.1) and can therefore be switched together with a ferroelastic switching of the underlying BFO domain. (ii) Not the magnetization of each domain is reversed, but the net magnetization built up from the stripe domain pattern. This feature is a result of the particular 71° stripe domain pattern.

The reliability of 71° stripe domains of BFO upon repeated electrical switching has not been addressed so far, which is an important issue in case these stripe domains of BFO are considered for device applications. The 71° stripe domains have a net polarization which has (for $(001)_c$-oriented films) an out-of-plane component and an in-plane component (see Fig. 2.7). It can be assumed that both components can be switched in general, either the in-plane component by applying an electric field in-plane, or the out-of-plane component by applying an electric field out-of-plane. It has been reported, that a common switching mechanism of a single domain consists out of 71° switching, where the component along the direction of applied electric field is reversed (Fig. 5.1(a)) [113–115]. If the net polarization of the 71° stripe domains is switched, however, a more complicated switching process has to occur. As depicted in Fig. 5.1(b, c), a rotation of the domain walls is necessary for both in-plane and out-of-plane switching processes in case the mechanical compatibility predicted by Streiffer *et al.* [50] is maintained. As a result, part of the film undergoes a 71° switching, and the rest of the film a 109° switching.

So far, not many studies exist regarding the switching process of the 71° stripe domains. Many reports investigate the manipulation of these domains by means of an AFM tip [48, 92, 116], which has, however, some drawbacks. On the one hand, the electric field under the tip is very inhomogeneous, and on the other hand, a scanning of the area which is supposed to be switched is necessary. In potential devices, capacitors with a homogeneous electric field between two electrodes are usually favorable; the observations from switching
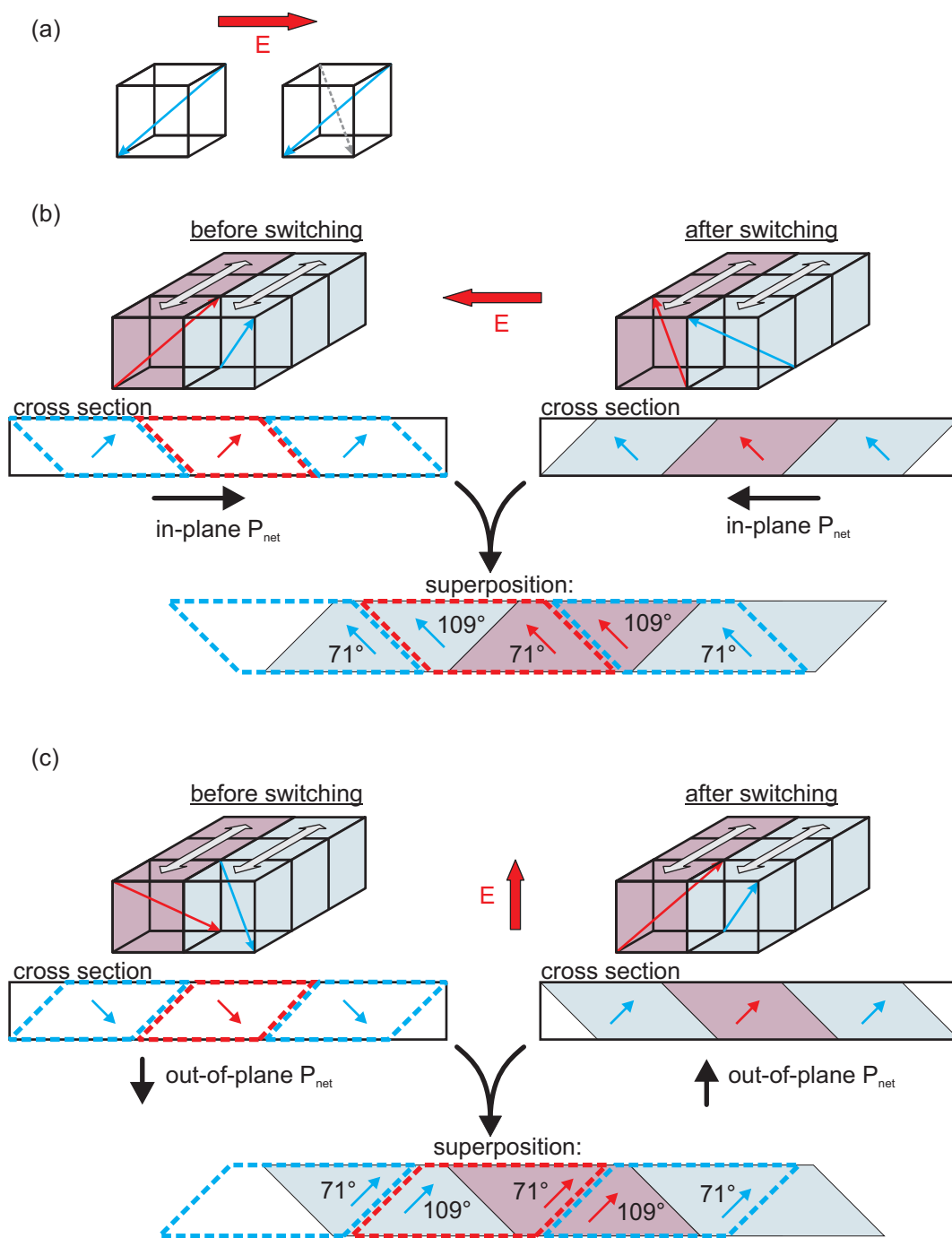
Figure 5.1: (a) In case the electric field E is applied along one of the cubic axes the component of the polarization along this axis can be reversed by a 71° switching. In case the (b) in-plane or (c) out-of-plane component of the net polarization of 71° stripe domains is reversed, a more complex switching process has to take place. It consists of a combination of 71° and 109° switching, as can be seen by the superposition of the pristine state and the switched state.

studies with an AFM tip, however, can not necessarily be translated to these capacitor systems.

In case in-plane electrodes are deposited on the sample, the observation of the in-plane domain switching between these electrodes is easily accessible by PFM. This approach has been used for instance to study the basic switching process between only two polarization variants in a $(110)_c$-oriented BFO film [115]. In fact, it has been already reported that the 71° stripe domain switching on STO and DSO substrates can be investigated by this method and that indeed the net in-plane polarization can be reversed [117, 118]. Very recently, the stability and fatigue behavior of 71° stripe domains of BFO on STO substrate was reported [112]. Further, electrical investigations were performed on $BFO/TbScO_3(110)_o$ samples with similar in-plane electrode configuration [119].

On the other side, for out-of-plane switching of the 71° stripe domains only macroscopic electrical studies exist [92]. The evolution of the domain pattern upon electrical switching itself has not been investigated so far. The out-of-plane approach is more laborious, because top electrodes have to be deposited. These top electrodes do not only affect the VPFM investigations [120], but also hinder LPFM imaging, as will be discussed later in this chapter. One way to circumvent this problem is a removal of the electrode after the switching cycles [121, 122], which has other drawbacks, as will be discussed.

In this chapter the macroscopic electric switching characteristics and the microscopic stability of the 71° stripe domain patterns upon repeated electrical switching is presented, for both the in-plane (Sec. 5.1) and out-of-plane (Sec. 5.2) capacitor configurations.

Part of the results presented in this chapter are published in Ref. [94].

5.1 Switching with in-plane configuration

For investigations of the in-plane net polarization switching of 71° BFO stripe domain patterns, a BFO film with 71° stripe domains is needed in the first place, and moreover, the growth of the BFO film on a highly insulating substrate with low dielectric permittivity, such as DSO, and the deposition of two metallic electrodes on the top film surface are essential so that the application of an in-plane electric field is possible. As presented in Sec. 4.2.2, it is possible to achieve 71° stripe domains in BFO films deposited directly on $DSO(110)_o$ substrates by annealing the DSO in O_2 atmosphere prior to film deposition. The 71° stripe domains are aligned along the $[001]_o$ direction of the DSO substrate, with the net in-plane polarization direction pointing along the $[\bar{1}10]_o$ direction. The switching investigations presented in this chapter were done on the same 50 nm thick BFO sample as shown in the previous chapter (see Fig. 4.10).

Subsequently, after BFO film growth two copper electrodes with a length of 1 mm and with a gap of 20 μm between each other were deposited on top of the BFO film by *ex situ* thermal evaporation through a shadow mask. As depicted in Fig. 5.2, the long sides of the electrodes were aligned parallel to the 71° stripe domains, so that an electric field could be applied perpendicular to the stripes, and therefore in the direction of the net in-plane polarization of the stripe pattern. Either a pulse generator was connected to the electrodes in order to apply square pulses for switching the BFO film in between the electrodes, or a ferroelectric tester was employed to measure the in-plane projection of the ferroelectric polarization. In between the electrodes, the domains were visualized by PFM. The cantilever was aligned along the $[\bar{1}11]_o$ direction of the substrate, which
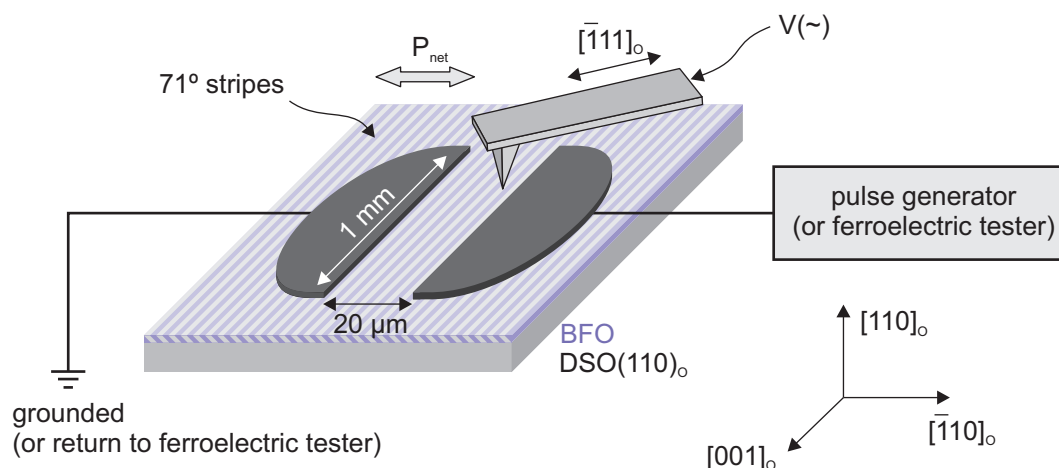
Figure 5.2: Schematics of the experimental setup for in-plane switching of the 71° stripe domain pattern.

corresponds to $[1\bar{1}0]_c$ (a 45° orientation) with respect to the pseudocubic axes, to allow for extraction of more information from only one scan. The electrodes were connected in such a way that the voltage could be applied without removing the sample from the AFM. Therefore, PFM measurements of the same area before and after the application of voltage pulses was feasible.

Figure 5.3(a) shows a LPFM image of a pristine area, acquired between the electrodes. As discussed already in Sec. 4.2.2, the VPFM reveals an almost uniform contrast indicating an out-of-plane polarization component pointing upwards and is not shown here. The in-plane component is sketched next to the LPFM images in Fig. 5.3(a), showing the typical zigzag with the net in-plane polarization pointing towards $[\bar{1}10]_o$, exactly as the as-grown domains imaged away from the electrode (compare with Fig. 4.10).

For verifying that the application of a voltage pulse switches the stripe domain pattern, a single, unipolar, square pulse of +200 V of 5 µs length was applied to the high potential electrode (see Fig. 5.2). As can be seen in Fig. 5.3(b), the complete stripe domain pattern is inverted in such a way that a bright contrast changed to an intermediate contrast, and an intermediate contrast changed to a dark contrast. This means, that the polarization of each stripe is rotated by 90° in the plane and the net in-plane polarization is reversed by 180°, as has been already reported before [12, 118]. The VPFM image remained unchanged and is not shown here. It should be noted though, that, as already mentioned, from theoretical considerations a more complex switching process should have taken place in the cross section view (see Fig. 5.1(b)). Even for the fastest pulse possible to apply by the pulse generator with amplifier (≈ 1 µs, because the rise time together with the fading time of the pulse adds up to 750 ns), the complete film between the electrodes is switched in the way as shown in Fig. 5.3(b).

The test of stability of these 71° stripe domains was done by repetitively switching the film with square pulses of ± 200 V of 5 µs length. Because of technical limitations of the pulse generator, after each complete switching cycle (one positive pulse and one negative pulse), a delay of 2.5 µs had to be introduced before the next pulse. Figure 5.3(c) displays the LPFM image after 5×10^5 of such switching cycles. The domain walls of the as-grown domain configuration are superimposed as black lines. It can be seen, that the domain pattern is very stable and almost no changes are visible. Only at a few spots, one of
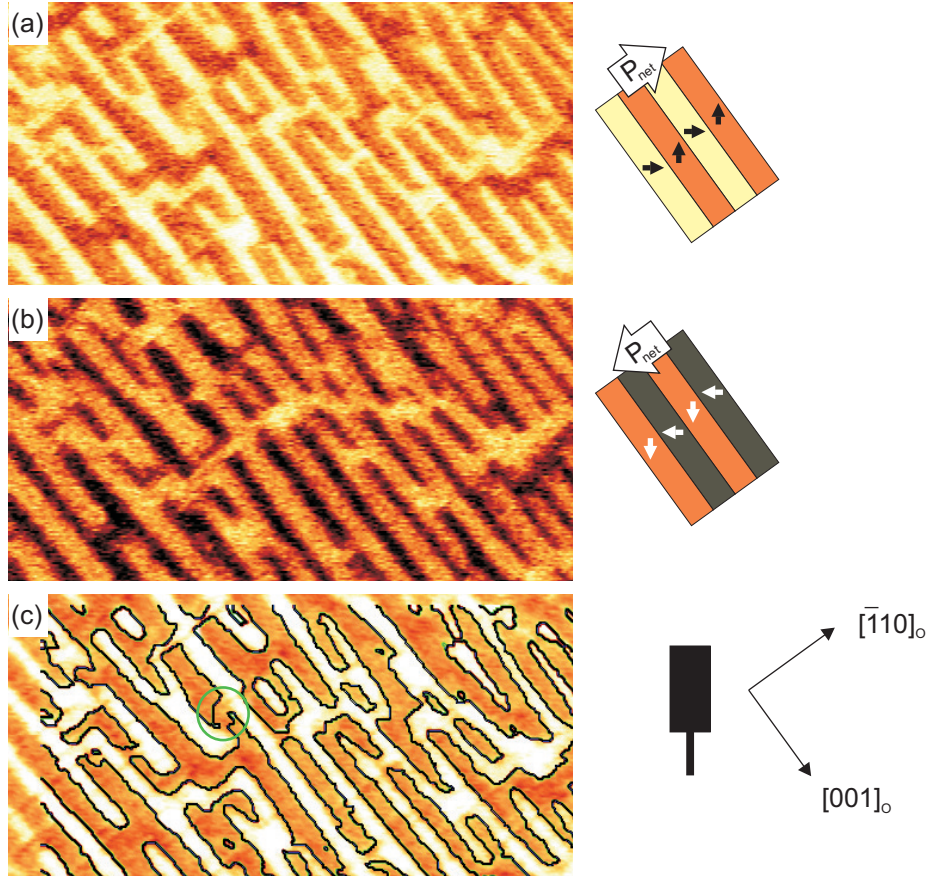
Figure 5.3: (a) As-grown LPFM image acquired between the electrodes with a sketch of the domain pattern and net in-plane polarization directions next to it. (b) LPFM image of the same area after applying a unipolar square pulse. (c) LPFM after 5×10^5 switching cycles with the as-grown domain walls from (a) superimposed as black lines. The green circle indicates one of the few changes in the domain pattern. All images are $5 \times 2.5\,\mu\mathrm{m}^2$. The cantilever orientation is sketched on the bottom right.

them marked by a green circle, did changes occur. The changes which are visible tend to remove the initial interruptions of the 71° stripe domains and drive the film towards a perfect 71° stripe domain pattern.

The switching process was investigated by macroscopic ferroelectric hysteresis measurements as well, by connecting the ferroelectric tester to a second set of electrodes and measuring the macroscopic in-plane switching current. Figure 5.4(a) shows the switching current and integrated polarization measured at $1\,\mathrm{kHz}$ and at room temperature after 1.7×10^6 switching cycles. To calculate the polarization an effective area of $A_{\mathrm{eff}} = l \cdot h$ was assumed, with l being the electrode length ($1\,\mathrm{mm}$) and h being the film thickness ($\approx 50\,\mathrm{nm}$) [119]. In addition, a slope coming from a capacitive charging of the sample was subtracted from the polarization curve (see Sec. 3.2.4). With these assumptions, a spontaneous polarization of $\approx 50\,\mu\mathrm{C/cm}^2$ is extracted from the measurement. This is in good agreement with the projection of the reported value for the spontaneous polarization of BFO onto the $[100]_c$ direction, considering the relative high error regarding the film thickness and the electrode area.
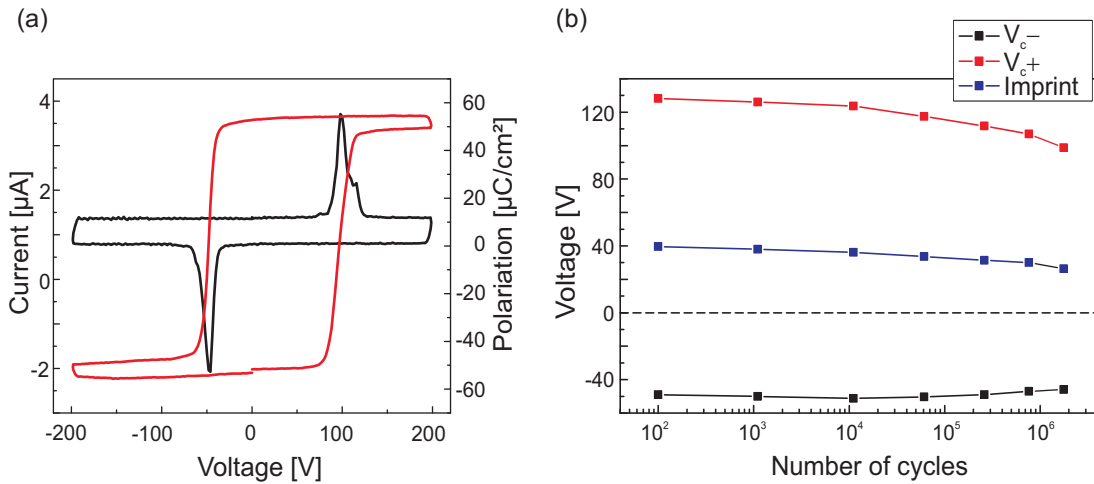
Figure 5.4: (a) Switching current and integrated polarization of an in-plane hysteresis, measured at $1\,\text{kHz}$ and room temperature after 1.7×10^6 switching cycles. (b) Development of the positive coercive voltage (V_c+), the negative coercive voltage (V_c-), and the imprint with increasing number of switching cycles.

The coercive voltages are very asymmetric, the switching peak at negative voltages having a lower absolute value than the one for positive voltages. The resulting hysteresis loop is thus highly imprinted towards positive voltages, which corresponds to a built-in electric field driving the net in-plane polarization towards the as-grown direction $[\bar{1}10]_o$. The reason for this may either be given by the interfacial properties which inferred the direction of as-grown polarization in the first place,[1] or – as reported for BFO films on TbScO₃ – by defect dipoles [119].

Figure 5.4(b) shows the evolution of the coercive voltages and imprint with increasing number of switching cycles. It can be seen that all three quantities tend to decrease. After the maximum of performed switching cycles, 1.7×10^6, the imprint has reduced to 66% of the initial value. This improvement is an advantage regarding device applications since lower imprint and coercive voltages are favorable.

Very recently,[2] it was reported that the 71° stripe domains of BFO on STO substrate show a fatigue behavior [112], which consists of (i) the formation of charged domain walls starting after approximately 10^6 switching cycles (which, however, does not affect the switchable polarization) and (ii) charge injection from the electrodes after 10^{10} switching cycles (which leads to domain wall pinning and subsequent decrease of switchable polarization). None of the two effects were observed here, which is most probably because the number of maximum performed switching cycles performed here is just at the border where changes at the domain pattern start to appear according to the report. Furthermore, the different substrates and the different electrode materials may further influence the stability and fatigue behavior of the BFO film as well. In addition, the macroscopic hysteresis loops in the report are not imprinted, which may result from the cubic STO substrate with no preferred structural variants in the BFO film.

---

[1] As described in Sec. 4.2.2, the as-grown structural variants are r_3 and r_4. In case the polarization is reversed, the variants have to change to r_1 and r_2. With the assumption that these variants are less energetically favorite, an imprint towards the as-grown state may be explained.

[2] After the completion of the experimental work of this thesis.
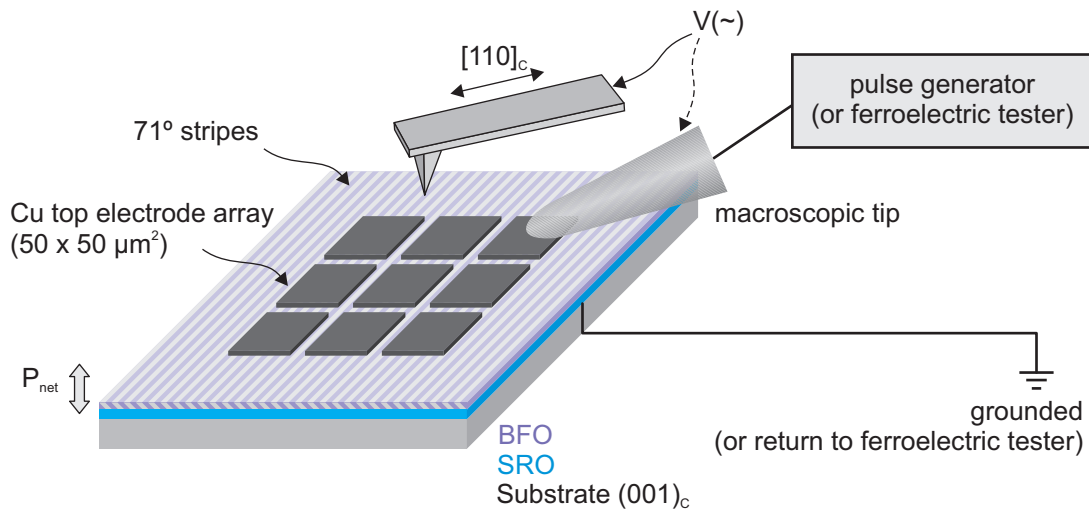
Figure 5.5: Experimental setup for out-of-plane 71° stripe domain switching.

Summarizing the behavior of in-plane switching of a 71° stripe domain pattern of BFO, it can be said that the domain pattern is very stable, for all the considered switching frequencies up to $100\,\mathrm{kHz}$. Even after 10^6 cycles no significant changes in the domain pattern are visible. In addition, the macroscopic electric switching properties improve with increasing switching cycles. Nevertheless, a strong imprint exists, with a built-in electric field driving the polarization towards the as-grown state.

5.2 Switching with out-of-plane configuration

Compared to the in-plane switching of the 71° stripe domains, the microscopic investigation of the domain pattern in the out-of-plane switching by PFM is more difficult because of the geometrical configuration itself, in which the BFO film is sandwiched between a bottom electrode and a top electrode (Fig. 5.5). There are two general approaches: either the domain configuration is revealed through the top electrode, or the top electrode is removed by chemical etching and subsequently PFM imaging is performed. In principle the first approach is favorable, because PFM investigations of the same location with successive switching pulses can be performed. However, it will be shown in the next section, that the LPFM image acquired through the top electrode is dominated by the VPFM signal and differs distinctly from the LPFM acquired without top electrode. A removal of the top electrode is therefore necessary for an unambiguous domain visualization. The drawback is, however, that it does not allow the observation of the domain evolution after intermediary number of cycles and it requires to make measurements on several neighboring capacitors, in order to study the dependence of the domain changes on the number of switching cycles. In other words, the final state after switching can not be compared to the pristine state at that location nor can it be compared with intermediate states.

First, in Sec. 5.2.1, the PFM investigations through the top electrode, as well as the domain stability upon top electrode removal is presented. In the following Sec. 5.2.2 the actual investigations about the stability of the 71° stripe domains upon repeated electrical switching are presented.
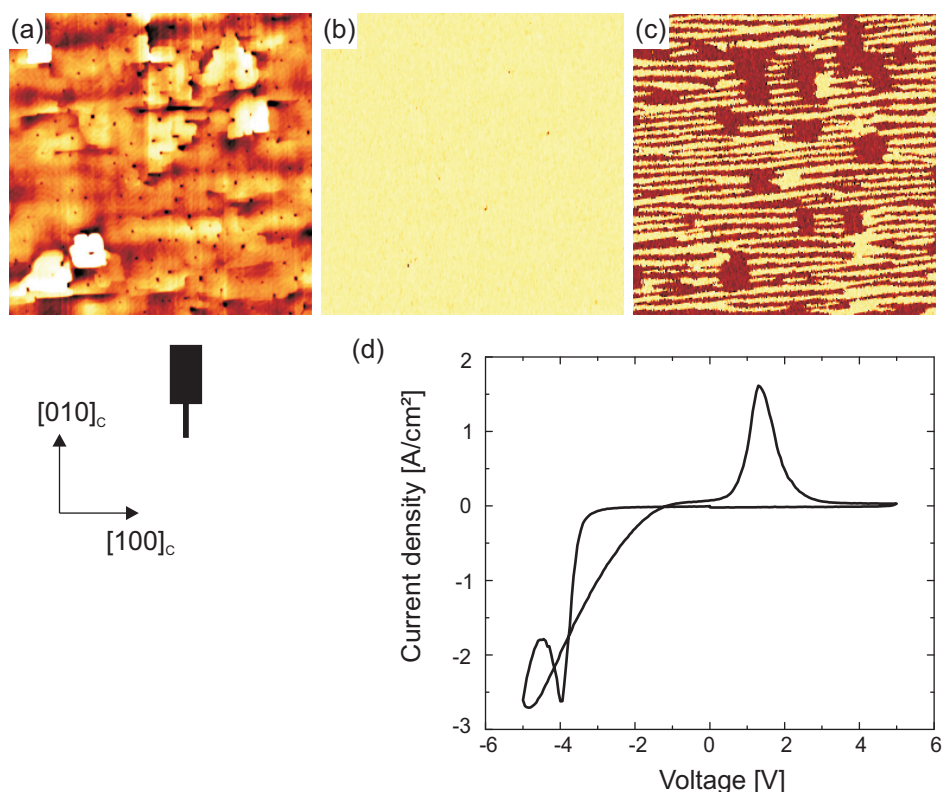
Figure 5.6: (a) Topography (scale 5 nm, rms: 1.6 nm), (b) VPFM phase and (c) LPFM phase of 150 nm thick BFO on SRO buffered STO(001)$_c$. All images are $8 \times 8\,\mu m^2$. The orientation of the cantilever is sketched next to the crystallographic coordinate system. (d) Ferroelectric switching current measured at 1 kHz and room temperature on Cu top electrode with $60 \times 60\,\mu m^2$ in size.

5.2.1 PFM imaging through a top electrode and domain stability upon top electrode removal

In this section basic studies regarding PFM measurements through a top electrode and the reliability of the investigation of the switched capacitors are shown. From the observations it will be reasoned which approach has been chosen for the actual 71° stripe domain out-of-plane switching investigations.

A 150 nm thick BFO film grown on SRO buffered STO(001)$_c$ was used for these investigations. Figure 5.6(a-c) shows the topography, VPFM phase and LPFM phase images, respectively. As already discussed in Chapter 4, for BFO films on SRO buffered substrates, the VPFM image reveals a uniform bright contrast, corresponding to an out-of-plane component of the polarization pointing towards the SRO bottom electrode. The LPFM image shows 71° stripe domains, which can be confirmed by a second LPFM image with different cantilever orientation (not shown).

To form plane-parallel capacitors for out-of-plane switching an array of copper electrodes with a layer thickness of 10-30 nm and a lateral size of $50 \times 50\,\mu m^2$ to $60 \times 60\,\mu m^2$ were thermally evaporated *ex situ*. Copper has been chosen as top electrode material, since on the one hand, if necessary, a removal of the top electrode by chemical

wet etching without attacking the BFO film is possible,[3] and on the other hand better switching properties were achieved compared to gold top electrodes (see Sec. 5.2.2.2). For macroscopic electric measurements one of the copper top electrodes was contacted by a macroscopic needle. The needle was either connected to the pulse generator, in case arbitrary switching pulses should be applied, or to the ferroelectric tester, in case the ferroelectric polarization should be measured. The SRO bottom electrode was either grounded or connected to the return of the ferroelectric tester, respectively (see Fig. 5.5).

A typical ferroelectric switching current is shown in Fig. 5.6(d). The switching peaks are pronounced, however, for negative voltages a rather strong leakage contribution is superimposed. The asymmetric leakage suggests that one of the interfaces (either SRO/BFO or BFO/Cu) is responsible for charge injection, which may be explained by different work functions and electron affinities of the electrodes, as well as different interface qualities [123, 124]. In addition, the two coercive voltages are asymmetric as well, similar to the in-plane switching configuration (see Fig. 5.4(a)). The corresponding built-in field is again directed in such a way that the polarization is driven to the as-grown state with an out-of-plane polarization component pointing towards the SRO bottom electrode. The measured imprint of $-1.3\,\mathrm{V}$ is in agreement with the valence mismatch model [89], as already mentioned before.

The hysteresis loop has been run through with negative voltages first, and thus switching the film upwards first. As a consequence of the high imprint voltages, however, the positive coercive voltage is close to $0\,\mathrm{V}$. The base of the positive switching peak starts in fact already shortly below $0\,\mathrm{V}$. Therefore, after a unipolar negative pulse and subsequent removal of the applied voltage, the polarization state with an out-of-plane component pointing upwards is relatively unstable.

In the following, a comparison of the two approaches for domain visualization by PFM shall be addressed. As already mentioned, PFM investigations through the top electrode are in principle advantageous, though their feasibility still has to be proven. On the other hand, in case the electrode is etched away, it has to be made sure that exposing the film to the acid does not change its domain state. In general, it has been reported that the chemical environment can influence ferroelectric domain states in some cases [125–127], and a particular case will be shown in Chapter 6 as well.

To allow for PFM image acquisition through the large top electrodes the alternating voltage for PFM read-out was applied to both the cantilever of the AFM and a macroscopic needle, which was connected to the same Cu top electrode (see Fig. 5.5). Without the macroscopic needle no PFM signal was detectable while scanning the sample, most likely because the small contact area between AFM tip and top electrode is not sufficient to connect the top electrode properly, leading ultimately to screening of the electric field in the BFO film by the top electrode [120]. It should be noted, however, that PFM measurement through top electrodes without additional macroscopic connection were already reported [128–130], but for much smaller electrode sizes which require far less charges for building up the voltage in the capacitor. In addition, in most reports only VPFM measurements are considered. For the BFO investigations shown here, an acquisition of the LPFM signal is required. So far not many reports exist about LPFM measurements through a top electrode, nevertheless, for a certain configuration the feasibility has been reported recently [131].

---

[3]Sample dipped for 10-20 s in the following ultrasonically agitated solution: $0.25\,\mathrm{g}$ $(HN_4)_2S_2O_8$ dissolved in $30\,\mathrm{ml}$ H_2O.
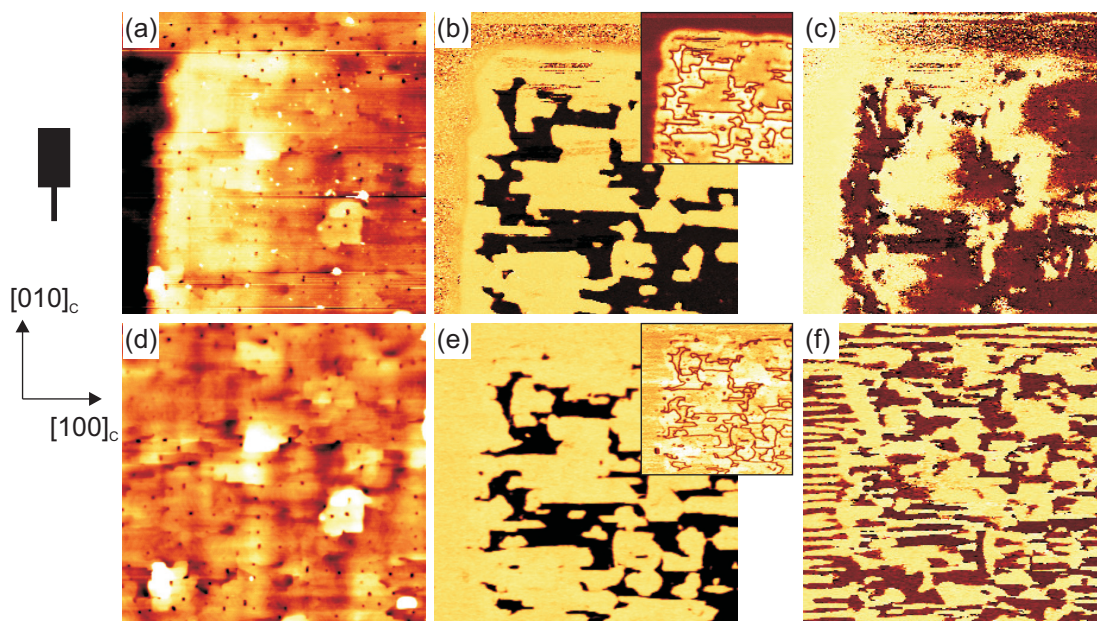
Figure 5.7: (a) Topography, (b) VPFM phase (inset shows amplitude) and (c) LPFM phase acquired at a corner of a 10 nm thick Cu top electrode deposited on a BFO/SRO/STO sample. (d) Topography, (e) VPFM phase (inset shows amplitude six times enhanced compared to (b)) and (f) LPFM phase of the same location after removal of the Cu top electrode. All images are $8 \times 8\,\mu m^2$. The cantilever orientation is sketched on the left hand side.

To test all these issues, the same location was imaged by PFM before and after etching the electrode. Figures 5.7(a-c) show topography, VPFM phase image and LPFM phase image, respectively, of a corner of a Cu capacitor which was cycled two times and left with an out-of-plane polarization component pointing upwards. Figures 5.7(d-f) on the other hand show topography, VPFM phase image and LPFM phase image, respectively, of the same location after removing the Cu top electrode. Several points can be noticed:

(i) Not the complete capacitor is switched upwards, but roughly half of the film has an out-of-plane component pointing downwards, as the as-grown state. This loss of retention may either be induced by the electrodes [132], or simply by the fact that the positive coercive field is close to 0 V. The latter point leaves the state with polarization pointing upwards rather unstable and may favor a retention loss after switching and before PFM imaging. On the other hand, the retention loss might even be induced by the PFM imaging itself, since the applied AC voltage for PFM read-out might be enough to switch the film partly to the more stable configuration with polarization down.

Therefore, for investigations of the 71° stripe domain out-of-plane switching the film should always be left in the state with polarization pointing downwards. In this case it is ensured that only the switching processes coming from the applied pulses are investigated, and not relaxation processes which are difficult to control.

(ii) The measured piezoelectric amplitude in VPFM with top electrode is about six times bigger than measured solely with the tip directly on the film surface (insets in Figs. 5.7(b) and (e)). The reason for this is probably a higher voltage drop across

the film, resulting from the better interface between evaporated electrode and film compared to the interface between AFM tip and film on the one hand, and from the better electrical connection by the macroscopic needle on the other hand.

(iii) The VPFM image acquired through the top electrode (Fig. 5.7(b)) and after etching (Fig. 5.7(e)) are very similar, but show a few differences though. First, without top electrode a few additional fine details are visible. This is in agreement with a report that the by PFM-measured domain wall width (and therefore the possible resolution) through a top electrode is in the order of the ferroelectric film thickness (here $\approx 150\,\text{nm}$), which results from clamping effects in the ferroelectric material due to the global piezoelectric response [120]. And second, at a few locations some domains with polarization pointing downwards (the stable state) have grown slightly in size. In other words, domains with polarization upwards exhibit slow retention loss under the etching process. In some cases, it is difficult to determine whether the increase of domains with polarization downwards results from the better resolution without top electrode or from the retention loss of domains pointing upwards.

To summarize, imaging the VPFM signal through the top electrode is possible, on cost of a slight loss of resolution. Etching away the Cu electrode leaves the domains with polarization downwards unchanged. The domains with polarization pointing upwards, however, appear to have a light loss of retention.

(iv) The LPFM image acquired with top electrode (Fig. 5.7(c)) is very different from the LPFM image after electrode removal (Fig. 5.7(f)). Since the two VPFM images do not differ so strongly, it can be assumed that the domains have not changed dramatically during the etching process. In addition, the LPFM and VPFM images acquired with top electrode have many common features, which suggests that a cross talk from the VPFM to the LPFM takes place [133]. There are two possible explanations why the cross talk is pronounced only with top electrodes. First, as described in (iii), the VPFM signal with top electrode is larger than without top electrode and therefore the cross talk contribution is larger as well. Second, the LPFM signal might be reduced with top electrode. On the one hand, the lateral movement may be damped due to the top electrode, and on the other hand, some of the explanations for the origin of the lateral PFM signal rely on an inhomogeneous electric field, which is absent with a top electrode.

Hence, reliable LPFM measurements are difficult to be performed with macroscopic top electrodes.

Therefore, all investigations have to be performed by etching away the top electrode first. To ensure that solely the switching due to the applied electric switching pulses is investigated, the film should always be left with an out-of-plane component of the polarization pointing downwards. Otherwise, in case the film is left with polarization pointing upwards, the domain pattern is not completely stable, neither after the voltage is released nor during top electrode removal.
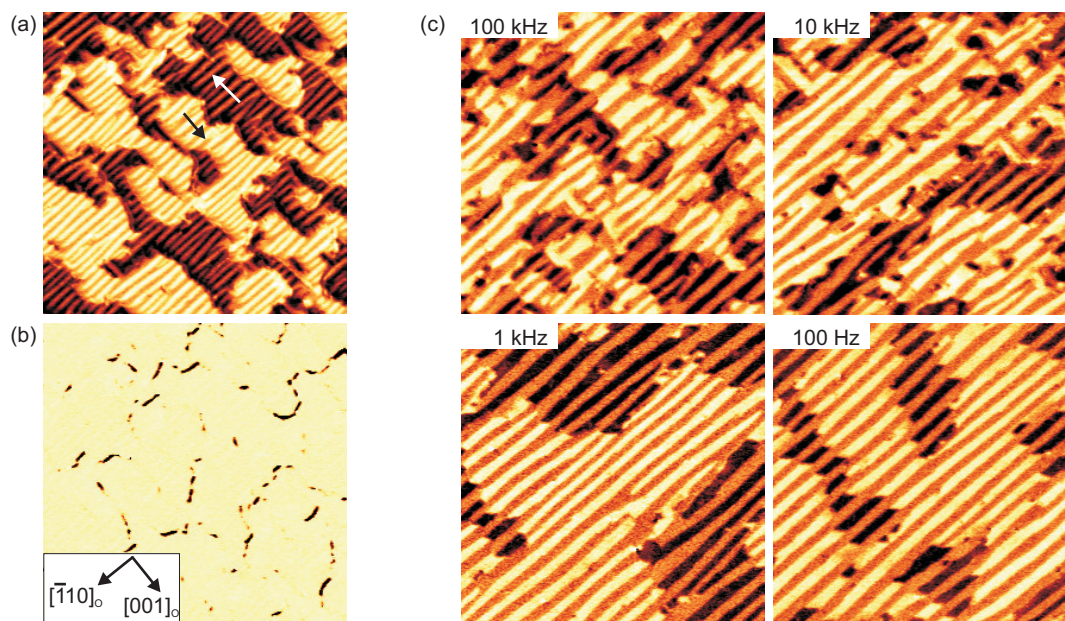
Figure 5.8: (a) LPFM and (b) VPFM image of an as-grown 150 nm thick BFO film grown on SRO buffered DSO, taken from Fig. 4.18(b-c). (c) LPFM images taken at areas where capacitors were cycled 5,000 times at different frequencies. All images are $8 \times 8\,\mu m^2$.

5.2.2 Stability of 71° stripe domains upon repeated out-of-plane switching

It was shown in Sec. 5.1 that the 71° stripe domain pattern is very stable under in-plane switching, for many switching cycles and for switching frequencies up to 100 kHz. In this section it will be shown, that the out-of-plane switching of the 71° stripe domains behaves very differently. First, in Sec. 5.2.2.1, it will be shown that the final domain state depends strongly on the applied switching frequency. The transition to the new domain state is discussed, as well as the ferroelectric switching properties. In Sec. 5.2.2.2, it is shown that the top electrode material influences the switching properties as well.

5.2.2.1 Frequency dependence and evolution of stripe domain width

For the investigation of the 71° stripe domain out-of-plane switching, 150 nm thick BFO films on SRO buffered DSO(110)$_o$ substrates and on SRO buffered STO(001)$_c$ substrates were used (see Sec. 4.3.2.2). The same setup as described in the last section was employed: First, an array of 30 nm thick Cu top electrodes was deposited on top of the films. Then, a macroscopic needle was contacted for electrical measurements, and last, the ferroelectric domains after the switching events were investigated by PFM after removal of the top electrode.

The clearly different behavior compared to the in-plane switching case is shown as example for the BFO film on SRO buffered DSO substrate in Fig. 5.8. LPFM and VPFM images of the as-grown state from Fig. 4.18 are reshown for a direct comparison in Fig. 5.8(a) and 5.8(b), respectively. Several capacitors were cycled for 5,000 times with square pulses of $\pm 4.5\,V$ amplitude and different frequencies, ranging from 0.1 kHz to 100 kHz. Then, after electrode removal, LPFM images were acquired at areas of these capacitors and are shown in Fig. 5.8(c). All VPFM images reveal a completely uniform

polarization downwards (not shown here), without the small lines of opposite polarization direction seen in the as-grown state. Whereas for the in-plane switching, independent of the switching frequency, no change in the domain pattern was visible, here, a transition to a new domain pattern occurred, which is in addition frequency dependent. The domain patterns for 1 kHz switching and 0.1 kHz switching are similar, with relatively large areas of same net in-plane polarization direction (stripe pattern with bright/intermediate contrast and dark/intermediate contrast, respectively). For increasing switching frequencies, these areas become smaller. In general, large areas with the same net in-plane polarization are energetically more favorable, since for domain walls, where different net in-plane polarization directions meet, energetically unfavorable head-to-head or tail-to-tail configurations have to form. This suggests that for the lower switching frequencies the film has the time to relax to the more favorable domain configuration. Because the switching at 1 kHz and 0.1 kHz gives similar results, but the switching at 10 kHz leads to a formation of smaller domains, the timescale per switching cycle which has to be provided to the film in order to maintain the stripe domains is between 0.1 and 1 ms.

Furthermore, it can be noticed, that even for the slow switching cycles, each stripe width has become wider. To get an insight into the transition from the as-grown state to the new domain state, capacitors were switched with increasing number of cycles and the resulting domains patterns were investigated. Figure 5.9 shows PFM images of areas where capacitors of the same sample were cycled with square pulses of ±4.5 V amplitude and 0.1 kHz frequency from 1 cycle up to 10,000 cycles. The average stripe widths were extracted by averaging over 50-100 stripes in the LPFM images and are plotted in Fig. 5.10. The stripe domain width increases rapidly during the first 100 switching cycles and keeps on increasing until 1,000-2,000 cycles. Starting from the as-grown stripe width of approximately 110 nm, a slightly more than double of its value, about 230 nm, is reached and maintained after about 2,000 cycles. From the LPFM images it can be seen, that, although the stripe domain width remains unchanged above 2,000 cycles, still a change in the domain pattern occurs, that is a lateral expansion of areas with the same net in-plane polarization direction.

At the same time, the VPFM images undergo a transition as well. The small black lines, which represent domains with a polarization component upwards, disappear within the first 1,000 switching cycles. For more than 1,000 cycles, the VPFM images reveal a uniform bright contrast and are not shown in Fig. 5.9 anymore. The disappearance of these domains correlate exactly with the final transition of stripe domain width seen in the LPFM images.

Figure 5.11 shows the same kind of investigation performed on a 150 nm thick BFO film deposited on SRO buffered STO substrate. Some properties are very similar compared to the BFO film on DSO substrate discussed above, though here, the frequency dependence is even more dramatic. In Fig. 5.11(a) and (b) are the VPFM image and LPFM image of the as-grown state, respectively, taken from Fig. 4.18 for direct comparison with the switched domain states. In Fig. 5.11(c) are again LPFM images acquired at areas where capacitors were cycled for 5,000 times by square pulses of ±5 V amplitude and frequencies ranging from 10 kHz down to 0.1 kHz. Similar to the BFO film deposited on SRO/DSO, the VPFM images show a uniform bright contrast without black lines and are not shown here. The LPFM images reveal, however, that only for the lowest switching speed, 0.1 kHz, the stripes are maintained. For 1 kHz cycling frequency, the stripes start already to break up, and only a mosaic like pattern consisting of small domains is left over for 10 kHz cycling.
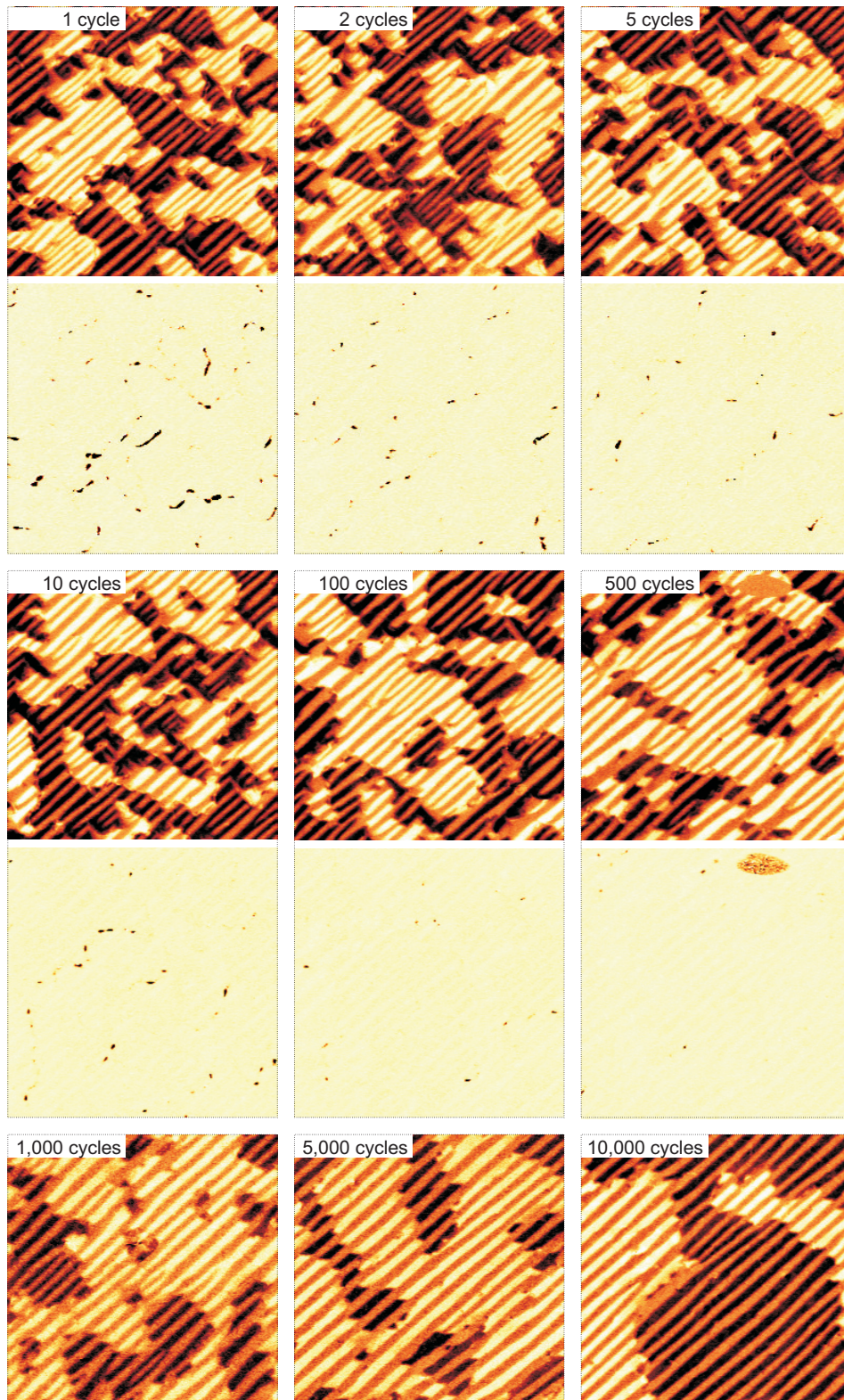
Figure 5.9: LPFM images (top) and VPFM images (bottom) of capacitors switched with increasing number of switching cycles at 0.1 kHz. All images are $8 \times 8 \, \mu m^2$.
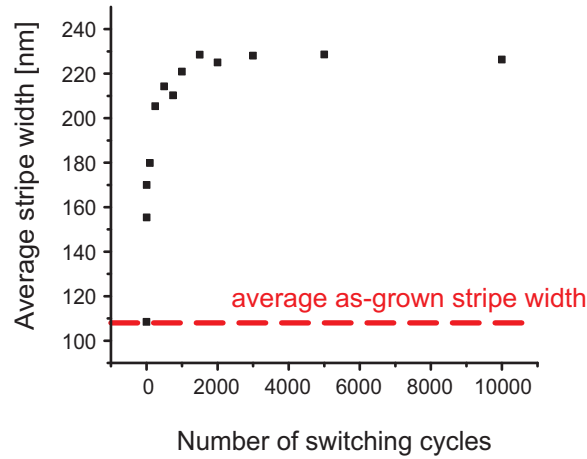
Figure 5.10: Evolution of average 71° stripe domain width with increasing number of out-of-plane switching cycles at 0.1 kHz. The domain widths were extracted from the LPFM images from Fig. 5.9.
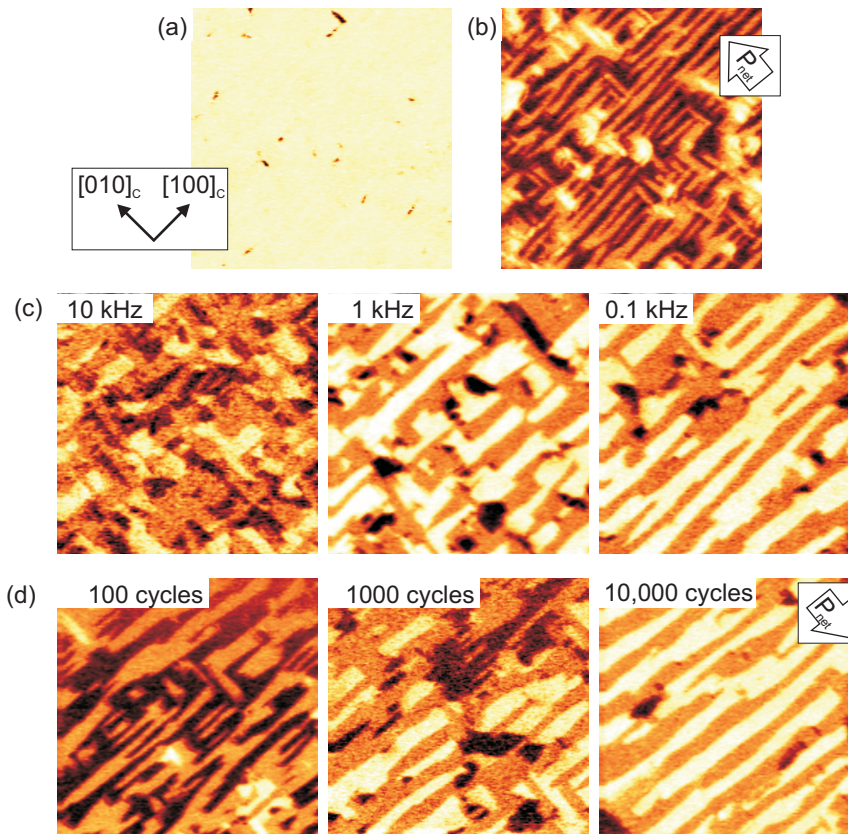
Figure 5.11: (a) VPFM and (b) LPFM image of an as-grown 150 nm thick BFO film grown on SRO buffered STO, taken from Fig. 4.18(e-f). (c) LPFM images taken at areas where capacitors were cycled 5,000 times at different frequencies. (d) LPFM images taken at areas where capacitors were switched by an increasing number of cycles at 0.1 kHz. All images are $6 \times 6\,\mu m^2$.
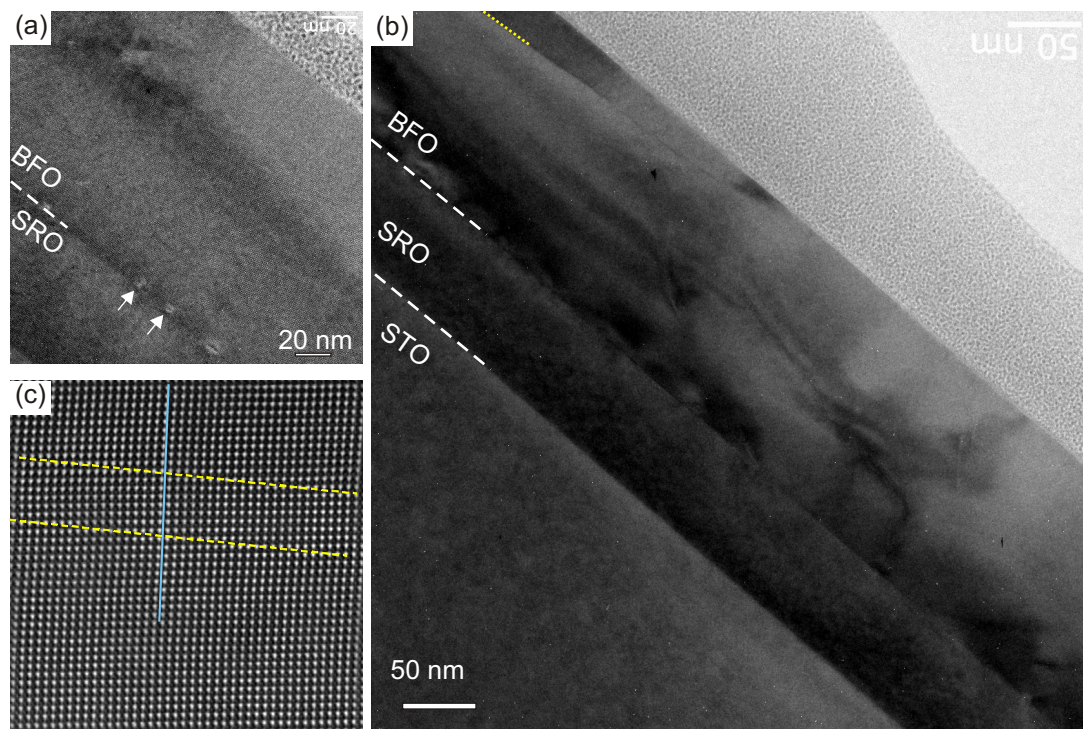
Figure 5.12: HRTEM cross section image close to $[010]_c$ zone axis of capacitors cycled 5,000 times with cycle frequencies (a) 0.1 kHz and (b) 10 kHz, respectively. The yellow line in (b) indicates one of the extended defects present in the film. (c) Close up of one of the defect lines (yellow lines) visible in (b). The blue line is a guide for the eye to see the tilt of the lattice planes.

The as-grown 71° stripe domains have an average stripe width of about 140 nm. This is a higher value than for the BFO film on DSO substrate, resulting presumably from the higher epitaxial in-plane strain performed by the substrate. Interestingly, for the 0.1 kHz cycling, the stripe domain width slightly more than doubles to 320 nm, which is exactly the same behavior as in the case of DSO substrate. On the other hand, here, the as-grown state has a preferred net in-plane polarization direction (dark/intermediate LPFM contrast), which is inverted after cycling (bright/intermediate LPFM contrast). Figure 5.11(d) shows LPFM images of areas where capacitors were cycled at 0.1 kHz, but with different amount of cycles. It can be seen, that a similar amount of switching pulses (1000-2000) is needed for the transition to the new domain state. In summary, despite the stronger frequency dependence on STO substrate, the two films on the different substrates show common behaviors in several aspects.

To get a further insight into the final state of the film after several switching cycles, a TEM specimen was prepared by FIB exactly from the cycled areas of the BFO film on SRO buffered STO shown in Fig. 5.11(c). Figure 5.12(a) and (b) show cross section HRTEM images of the capacitors cycled 5,000 times at 0.1 kHz and 10 kHz, respectively. For the capacitor cycled at 0.1 kHz we observed only misfit dislocations at the BFO/SRO interface (indicated by the arrows), which are also visible for the capacitor cycled at 10 kHz. Since XRD-RSM measurements showed that the thick BFO film on STO substrate is partly relaxed (see Fig. 4.19(a)), misfit dislocations are expected to occur in the film. On the other hand, the HRTEM image of the capacitor cycled at 10 kHz shows also other extended defects within the BFO film. In relation to the TEM image of
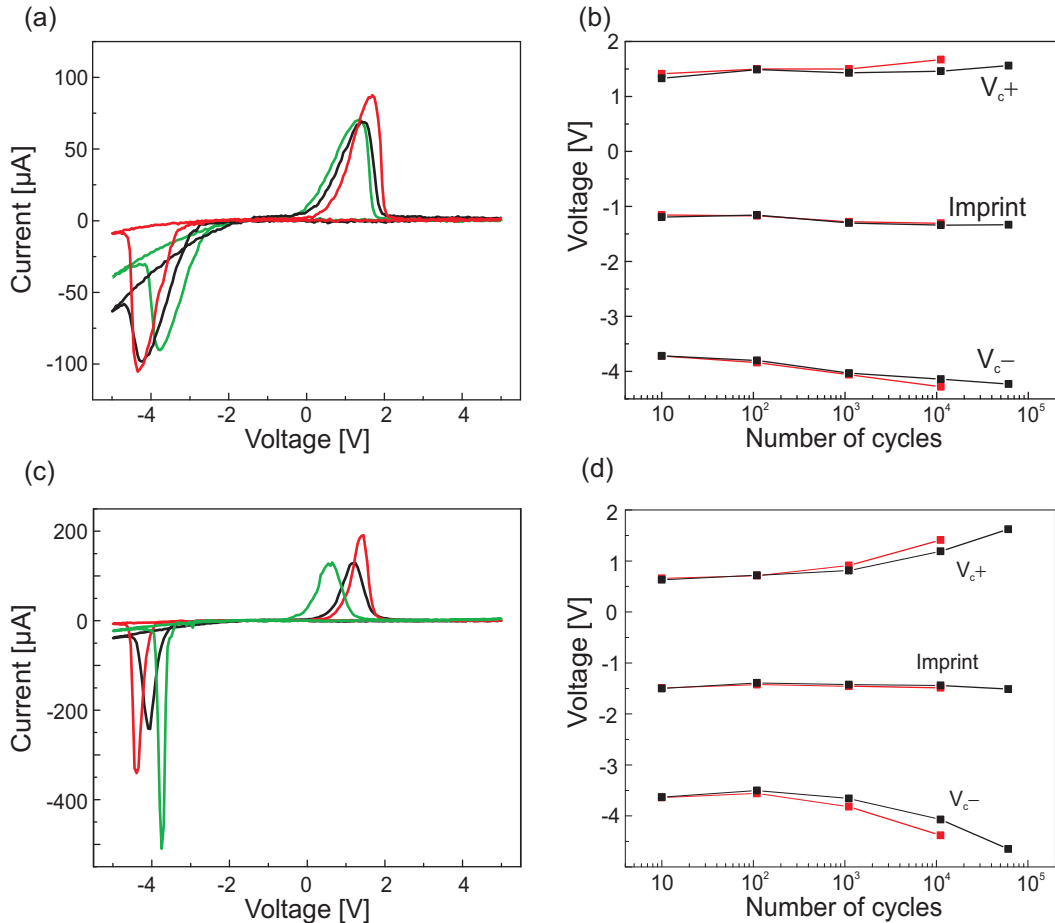
Figure 5.13: Ferroelectric switching current measured at 1 kHz and room temperature for the sample (a) Cu/BFO/SRO/DSO and (c) Cu/BFO/SRO/STO with the as-grown hysteresis (green) and after 1.1×10^4 cycles with 0.1 kHz (red) and 10 kHz (black). The evolution of the positive coercive voltage V_C+ and the negative coercive voltage V_C- as well as the imprint is plotted for the film on (b) DSO substrate and (d) STO substrate.

the as-grown state of a similar film shown in Fig. 4.20 and the slowly cycled film shown in Fig. 5.12(a), which show only few defects and domain boundaries, it can be reasoned that due to the fast switching cycles more defects formed in the film. In particular some horizontal lines are visible (e.g. the yellow line in Fig. 5.12(b)). Figure 5.12(c) shows a higher magnification STEM image of such a horizontal defect, indicated by yellow lines. The blue line as guide to the eye reveals that the two regions above and below the defect line are tilted by approximately 1°. This tilt is in agreement with a peak splitting seen in the diffraction pattern, which can be attributed to a rotation of the diffraction pattern by 1°. In fact, Nelson *et al.* [134] showed by *in situ* TEM investigations that due to the switching process oxygen vacancies may accumulate in ordered planes, often aligned horizontally as well. An unambiguous assignment of the type of defect seen here is not possible, still, the influence of defects will be discussed further down in more detail.

The out-of-plane switching of the 71° stripe domains can be investigated by macroscopic ferroelectric hysteresis measurements as well. Figure 5.13 shows the ferroelectric switching current for the BFO film deposited on both DSO substrate and STO sub-

strate, which were shown in Fig. 5.8 and Fig. 5.11, respectively. The voltage was applied to the copper top electrode by the macroscopic tip while the SRO bottom electrode was grounded. Further, in contrast to the PFM investigations, each set of experiments was performed on one capacitor. Two different switching frequencies were investigated, 10 kHz and 0.1 kHz. In the as-grown state (green curve in Fig. 5.13) the coercive voltages were imprinted by -1.1 V to -1.5 V, indicating a built-in field driving the polarization towards the as-grown direction pointing downwards to the SRO bottom electrode, as already discussed in Sec. 5.2.1. The onset of leakage for negative voltages is seen for both samples as well. With increasing number of switching cycles this onset of leakage improved for 0.1 kHz cycling (red curve), but worsened for 10 kHz (black curve), as shown for example after 1.1×10^4 cycles in Fig. 5.13(a) and (c). The evolution of the coercive voltage and the imprint were extracted from the hysteresis curves and plotted in Fig. 5.13(b) and (d) for DSO substrate and STO substrate, respectively. The coercive voltages increased in both cases, for STO substrate, however, the effect is more pronounced. The imprint, on the other hand, stayed constant.

The out-of-plane switching discussed here and the in-plane switching discussed in Sec. 5.1 show clear differences in the stability upon repeated switching at all frequencies. To understand the differences it is worth to have a closer look at the two configurations, which differ in their geometrical design. The different geometries may influence the switching behavior in a way described in the following. The theory for ferroelectric polarization reversal is generally accepted to follow the Kolmogorov-Avrami-Ishibashi (KAI) model [135, 136]. For BFO films it has been reported though, that slight modifications in the KAI model have to be introduced [137], mainly due to the complex domain structure of BFO. Still, the main idea of this model holds, that the polarization reversal starts at statistically distributed nucleation centers, followed by a sideways growth of the domains. Usually, the nucleation centers are situated at the interface between ferroelectric film and electrode or at defects close to this interface [138]. The domain growth is initiated by spike-shaped domains which rapidly grow to the other electrode [139, 140]. Then, these spike-shaped domains start to grow laterally, but relatively slowly. The amount of nucleation centers should therefore be proportional to the area of the electrode A. Normalized to the film volume V, the two different configurations for in-plane and for out-of-plane switching have the following ratio A/V

$$\left(\frac{A}{V}\right)_{\text{in-plane}} = \frac{l \cdot h}{l \cdot h \cdot d} = \frac{1}{d} = \frac{1}{20\,\mu\text{m}} = 5 \times 10^4\,\text{m}^{-1} \tag{5.1}$$

$$\left(\frac{A}{V}\right)_{\text{out-of-plane}} = \frac{l^2}{l^2 \cdot h} = \frac{1}{h} = \frac{1}{150\,\text{nm}} \approx 7 \times 10^6\,\text{m}^{-1} \tag{5.2}$$

with the in-plane electrode length l, film thickness t, and electrode separation d. In this estimation, the in-plane switching configuration has two orders of magnitude less nucleation centers, even without considering the additional fact that the electrode is just on top of the film and not ranging to the substrate. Furthermore, the spike like domains forming from electrode to electrode can cover much longer distances (20 µm) in the in-plane case, than for the out-of-plane configuration (150 nm). As a consequence, the capacitors in the out-of-plane configuration will have many nucleation centers, where the film is switched independently. When different switched areas meet by sidewise growth, unfavorable domain configurations can occur. In this case, the system may want to relax,
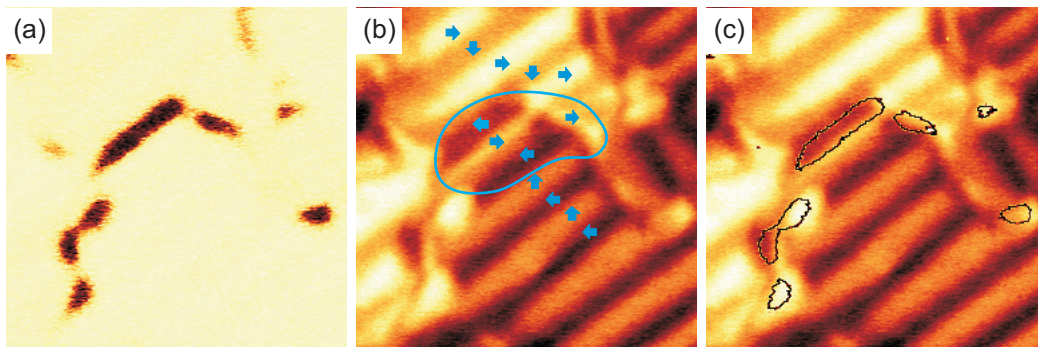
Figure 5.14: (a) VPFM phase image and (b) LPFM image with the direction of polarization indicated by blue arrows. (c) The LPFM images of (b) with the vertical domain walls of (a) superimposed. All images are $1.5 \times 1.5\,\mu m^2$.

probably by a ferroelastic switching, which was reported to demand a certain relaxation time [113], and may introduce a frequency dependence to the system.

In addition, it was shown that the separation distance of the electrodes can influence the switching behavior [112], i.e. that lager electrode distances stand more switching cycles. The electrode separation d differs strongly for the in-plane configuration and out-of-plane configuration considered here. As a result from the scaling of the coercive field of ferroelectrics with thickness [118, 141], much higher electric fields had to be applied in the out-of-plane configuration. This, however, may favor the injection of charges from the electrode into the BFO film, which may influence the switching behavior and can even lead to domain pinning [112]. Therefore, the out-of-plane configuration may be more prone to changes during switching cycles.

A further important role may be played by the defects, in particular by oxygen vacancies, which are difficult to observe, though usually present to a certain extent in oxide thin films [142, 143]. Nelson et al. [134] showed by *in situ* TEM switching investigations of BFO lamella sandwiched between a bottom electrode and a needle, that oxygen vacancies have an impact on the BFO switching characteristics. Due to the switching process, ordered planes of oxygen vacancies can form which act as pinning centers. Often, these planes of oxygen vacancies aligned horizontally, similar to the horizontal lines seen in the TEM images in Fig. 5.12(b). A further proof that the mobility of the oxygen vacancies and their redistribution play a crucial role during the switching of the BFO film was given recently by spatially resolved photodetection [144] and by Kelvin probe microscopy measurements [112]. Moreover, charged domain walls can form during the switching process [112], as well as cation defects, such as Bi substitution by Fe in the vicinity of 180° domain walls [134].

The BFO films discussed here have defects as well. Especially the black lines seen in VPFM with polarization upwards may be stabilized by defects, likely oxygen vacancies. This kind of lines were observed already before and could be influenced by an oxygen plasma [126]. After annealing in vacuum, the lines were reestablished similar to the as-grown state. Figure 5.14 shows a PFM image zoomed to one of those black lines. An unambiguous domain reconstruction is difficult because of the following reason. The VPFM domain walls seen in Fig. 5.14(a) do not match to the domain walls seen in the LPFM image in Fig. 5.14(b), but run right through the middle of the domains seen in LPFM (see superposition in Fig. 5.14(c)). One possibility is, that all of the domain walls,
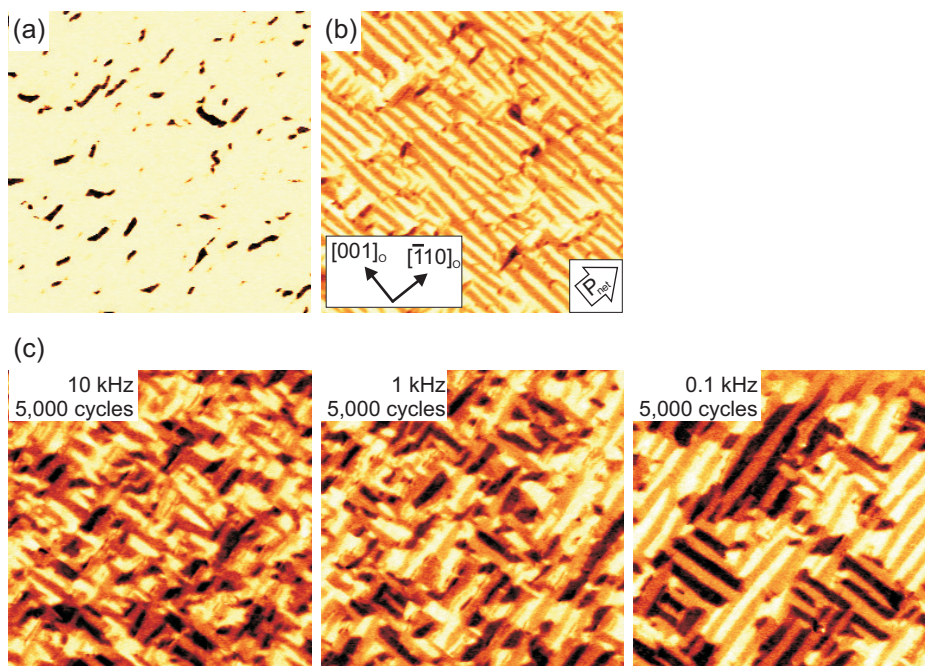
Figure 5.15: (a) VPFM phase image (b) LPFM image of 150 nm thick BFO on SRO/DSO substrate. (c) LPFM images of areas where capacitors were cycles 5,000 times at different frequencies.

the ones from VPFM and the ones from LPFM, are present in the film. This would result in many domain walls confined in a small area, which seems energetically unfavorable and therefore unlikely. Another explanation may lie in the PFM method itself. The space group of BFO is identical to the one of LiNbO$_3$ and allows in general a lateral signal at a vertical domain wall [145]. Though this effect has not been studied for BFO so far, the LPFM domain seen at the VPFM domain wall in Fig. 5.14 may not be existent, but just be an "artifact" of the PFM method. Due to the small domains in this area, the many piezoelectric tensor elements (see Sec. 3.2.1.2), and the complex domain structure of BFO, this issue can not be fully resolved. Despite this issue, for both explanations it can be said that a head-to-head or/and tail-to-tail configuration of the polarization exists. This supports the assumption that charged defects are present to stabilize these lines, which was proven recently by Kelvin probe microscopy measurements [112].

A further evidence that these defects influence the switching behavior is given by another 150 nm thick BFO film grown on SRO buffered DSO, which incorporated more of the lines with polarization upwards in VPFM (Fig. 5.15(a)). The LPFM image in Fig. 5.15(b) reveals as well 71° stripe domains, with a preferred net in-plane polarization direction. LPFM images of areas where capacitors were cycled 5,000 times with square pulses of ±5 V and different frequencies are shown in Fig. 5.15(c). Compared to the BFO film on SRO/DSO with less lines of opposite polarization the frequency dependence is more pronounced. Here, for 1 kHz the stripes start to break up, and for 10 kHz the stripes transformed almost to a mosaic-like pattern already. Under the assumption that the lines of opposite polarization are linked to the amount of defects in the film, the pronounced frequency dependence points to the possible impact of the defects on the switching characteristics.

One point which all films have in common for the out-of-plane switching, independent of the strain state, the number of defects, and the film thickness, is that for low switching frequencies of 0.1 kHz the 71° stripe domains are maintained, but the stripe width increases to about twice its as-grown value. The origin of this effect may only be conjectured here. It may be suggested, that in case enough time is given to the system, the film prefers to relax to the new domain state with double stripe width, presumably because it is energetically more favorable than the as-grown state. Due to the switching process, the film may have the required energy to develop slowly towards the new favorable state. The stripe width for 71° stripe domains has been investigated by Huang *et al.* [101, 104], showing that it depends on the domain wall energy F_w and the elastic energy F_e. The elastic energy F_e depends on the shear modulus G, Piosson's ratio ν, and the magnitude of the strain, i.e. the rhombohedral distortion. One explanation why the stripe domains favor a new width may lie in BFO's high Curie Temperature, which is above the growth temperature. As a result, the BFO film grows directly in the ferroelectric phase forming stripe domains. On cooling down, the lattice parameter, in particular the rhombohedral distortion, the oxygen octahedron rotations, and the ion shifts change [44, 146], which may alter F_w and F_e and ultimately the preferred stripe width. In case the temperature during cooling down is not anymore sufficient to redistribute the stripe domains to the new state, the preferred domain state at elevated temperature directly after growth is frozen. Then, with the help of the switching cycles, the new domain state may be accessible. Another change of the BFO environment comes from the *ex situ* deposited copper top electrode, which introduces a second interface to the BFO film. It is conceivable that this additional interface influences the favored stripe width as well.

5.2.2.2 Influence of the top electrode material

During the investigations of the 71° stripe domain out-of-plane switching it turned out that copper top electrodes gave best switching properties. Nevertheless, in this section the behavior with gold top electrodes is presented, to prove that the top electrode material has a major influence on the switching properties as well. For this, the 150 nm thick BFO film on SRO buffered STO substrate, whose switching properties were already reported for copper top electrodes in the last section, was covered partly with *ex situ* evaporated gold top electrodes as well. Figures 5.16(a) and (b) show a VPFM phase image and LPFM image of this film after cycling 25,000 times at 10 kHz with copper top electrode. As discussed in the last section, this procedure destroys the 71° stripes, and at the same time the lines with polarization pointing upwards disappear. In case gold top electrodes are employed, after the same treatment the VPFM phase image in Fig. 5.16(c) shows several opposite domains, similar to the as grown state (see Fig. 5.11). At an intermediate state, however, these opposite domains were removed from the film, as can be seen for instance after 5,000 cycles in Fig. 5.16(e). In other words, the domains of opposite polarization are first removed, as in the case of copper top electrode, but for increasing number of cycles new domains of opposite polarization are introduced into the film. The LPFM images show for both types of top electrodes that the stripes are destroyed, with the difference that the domains after 25,000 cycles are broken into smaller domains for the gold top electrode, presumably due to the introduction of the opposite domains in the VPFM image.

In addition, the ferroelectric hysteresis with gold top electrodes has a different evolution with increasing number of switching cycles. The hysteresis measurements were performed
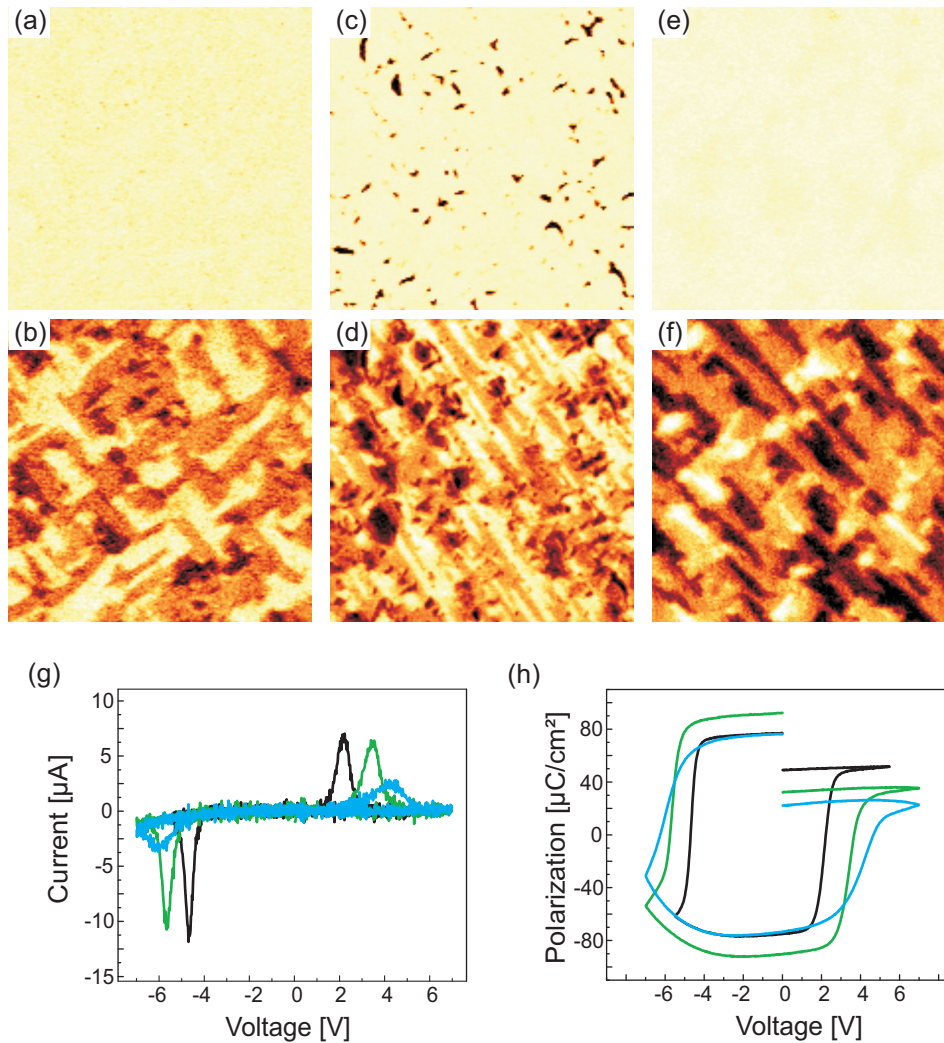
Figure 5.16: VPFM phase image and LPFM image, respectively, (a, b) after 25,000 cycles at 10 kHz for Cu/BFO/SRO/STO and (c, d) after 25,000 cycles and (e, f) after 5,000 cycles for the Au/BFO/SRO/STO sample. All images are $6 \times 6\,\mu m^2$. Ferroelectric hysteresis curves measured at 1 kHz and room temperature, showing (g) current versus voltage and (h) integrated polarization versus voltage after 1,000 cycles (black curve), after 5,000 cycles (green curve), and after 25,000 cycles (blue curve) at 10 kHz.

.

at 1 kHz and room temperature. The cycling was done with the same conditions, namely a pulse frequency of 10 kHz and an amplitude of ± 5 V. The current versus voltage curves are shown after 1,000 (back curve), 5,000 (green curve), and after 25,000 cycles (blue curve) in Fig. 5.16(g). On the one hand the coercive voltages are imprinted in the same way as with copper top electrodes. On the other hand the coercive voltage increased more pronounced with Au top electrode. Furthermore, the area under the switching peaks, which corresponds to the switchable polarization, drops visibly after 25,000 cycles. This can be seen, despite the leakage and the different offset for each curve, as well in the right hand side of the graph showing the integrated polarization, displayed in Fig. 5.16(h). The decrease in switchable polarization coincides with the appearance of the opposite domains in the VPFM image. This suggests that these opposite domains may be pinned, a common origin for a drop in switchable polarization, named fatigue,

which in addition was often reported to depend on the electrode material [147, 148]. One possible explanation for the domain wall pinning was given by charge injection from the electrodes [112], which is likely to be very dependent on the electrode material.

In conclusion, Cu top electrodes have far better properties compared to Au electrodes concerning the fatigue of the BFO films shown here.

5.3 Summary

Recently, many new functionalities at ferroelectric and multiferroic domain walls and of domain patterns were reported, in particular for the 71° stripe domains in BFO. So far, the ferroelectric switching behavior of these 71° stripe domains upon repeated electric switching has not been addressed, though it is an important issue regarding devices. In this chapter the switching properties in two different configurations was discussed for the first time.

Compared to the out-of-plane configuration, in the in-plane configuration, where the in-plane component of the net polarization is switched between two electrodes aligned parallel to the 71° stripes, the domain pattern is very stable. Up to the maximum number of investigated cycles, 5×10^5, and up to the fastest applied frequency, $100\,\mathrm{kHz}$, only very little changes in the domain pattern are visible. Those changes which are visible tend to remove the interruptions present in the as-grown state. The macroscopic electrical measurements reveal a built-in electric field, which is aligned parallel to the as-grown net polarization. Upon repeated switching cycles, the coercive voltages and the imprint are reduced.

In contrast, in the out-of-plane configuration, where the out-of-plane component of the net polarization is switched in plane-parallel capacitors, the domain pattern changes upon repeated switching. For frequencies higher than $\approx 1\,\mathrm{kHz}$ the areas with the same net in-plane polarization decreased clearly, or even a completely different pattern consisting of mosaic domains formed. The degree of sensitivity to the frequency seems to depend on the amount of defects, as well as the strain state in the BFO film. For low switching frequencies (0.1 to $1\,\mathrm{kHz}$) the 71° stripes are maintained in all films, though the stripe width is approximately doubled after about 2,000 cycles. The coherent areas with the same net in-plane polarization expand with increasing switching cycles. With respect to the application of these 71° stripe domains in potential devices this frequency limitation regarding the stability is a severe drawback.

As last point it was shown that BFO with gold top electrodes is more prone to fatigue compared to Cu top electrodes where no domain pinning was visible for the investigated switching cycles.

6

Differential etching of epitaxial BiFeO₃ thin films

Differential etching is a common property of ferroelectric materials and refers to different etch rates or different etch behaviors of ferroelectric domains. It was first discovered in 1955 for BTO by Hooter and Merz [149]. After the exposure of BTO single crystals to hydrochloric acid, the c^+, c^- and a domains exhibited a different surface appearance. A similar behavior has been reported for many other ferroelectric materials, such as YMnO₃ [150] or LiNbO₃ [151]. The main application of differential etching has been the visualization of the ferroelectric domains by subsequent optical microscopy [152]. In case of LiNbO₃ it has been employed for structural fabrication as well, including waveguides [153], micro-cantilevers [154], and photonic microstructures [155], which is enabled by the high differential etch ratio of LiNbO₃ [156].

A general origin of differential etching has not been revealed so far, although this behavior is now known for more than 50 years. In case of LiNbO₃ a model has been proposed, which will be briefly discussed later, however, this model can neither be transferred to other materials nor can it explain all observations on LiNbO₃.

For BFO, so far just one early report about etching of BFO single crystals with diluted nitric acid exists, which focused on the revelation of the ferroelectric domains and proof of BFO's polar nature [157]. In this chapter the differential etch behavior under hydrofluoric acid (HF) is considered. Although no model for an explanation can be given for the differential etch behavior here, a tentative explanation is given that the contribution of charges to the etch process plays a role.

First, in Sec. 6.1 the different etch rates and the etch behavior under exposure to several HF concentrations are determined. Then, in Sec. 6.2 a new phenomenon of differential etching under illumination with light is shown, which has not been considered for other ferroelectric materials so far. In Sec. 6.3 it is shown that differential etching can be employed to fabricate epitaxial submicron structure of BFO. So far not many reports exist about the fabrication of BFO nanostructures. On the one hand, no bottom-up approach was reported yet, which may be a consequence of a difficult growth due to the rather complex phase diagram of BFO (see Fig. 2.3). On the other hand, the most reported top-down approaches employed FIB milling [113, 158, 159], which may introduce defects to the fabricated structures and requires a recovery procedure [159]. Differential etching allows a new top-down approach, for which patterns of any shape can be obtained, in a direct way without the employment of photoresist and a photolithography step for instance. Structures with less than 200 nm in lateral size and good switching properties were achieved. Differential etching can therefore be a good alternative to other structur-
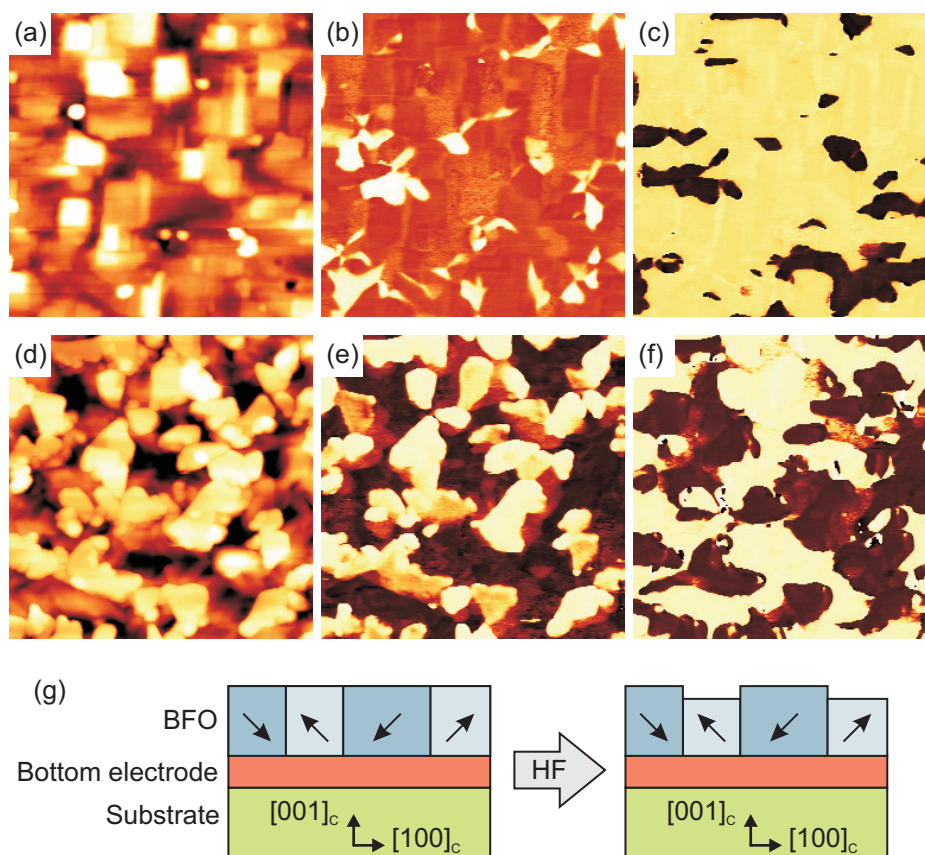
Figure 6.1: (a) Topography (scale 25 nm), (b) VPFM phase image and (c) LPFM phase image of a BFO film on LSMO buffered STO. (d) Topography (scale 70 nm), (e) VPFM image and (f) LPFM image after exposure of the film to a solution of 0.5 % HF for 30 s. (g) Schematics of the differential etch behavior of BFO under HF.

ing methods. Nevertheless, differential etching in BFO has other drawbacks, which will be discussed as well.

Part of the results shown in this chapter are published in Ref. 160.

6.1 Differential etch behavior and determination of the differential etch rate

In this section the differential etch behavior of epitaxial BFO films under the exposure to HF at room temperature is shown and the different etch rates for different HF concentrations determined. In Fig. 6.1, an example of the basic differential etch behavior investigated here is shown. The topography, VPFM phase image and LPFM phase images of the pristine state of an about 200 nm thick BFO film deposited with high laser fluency on LSMO buffered STO is shown in Fig. 6.1(a-c), respectively. As discussed in Sec. 4.3.2.2, as a result of the high laser fluency all eight possible directions occur in the film, i.e. $P^+_{1,...,4}$ ($= P^+$) and $P^-_{1,...,4}$ ($= P^-$). After exposure to HF in an aqueous solution,[1] the topography, VPFM phase image and LPFM phase image are shown in Fig. 6.1(d-f), respectively. It can be seen, that domains with an out-of-plane polarization component

---

[1]In this case for 30 s in 50 ml H_2O and 0.5 ml HF (50 % concentrated) $\approx$ 0.5 % concentrated HF solution.
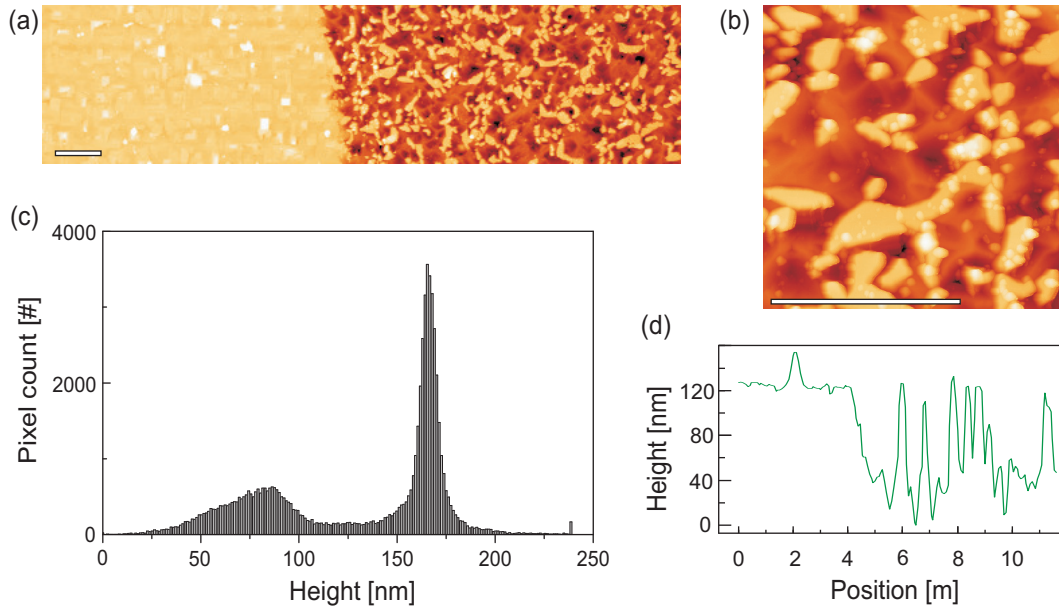
Figure 6.2: AFM topography acquired in tapping mode at (a) the edge of the etch area and (b) in the middle of the etched area after 30 s in 0.5 % HF. Color scale is 200 nm, scale bars are 2.5 μm. (c) Height histogram and (d) scan line across the edge, both taken from the AFM image shown in (a).

pointing upwards (P^+) are now deeper than domains with an out-of-plane polarization component pointing downwards (P^-). A correlation between the topography and the lateral domains, however, can not be drawn. Figure 6.1(g) sketches this behavior. Independent of the lateral domain component, all domains with a polarization component upwards are etched faster than those with an out-of-plane component downwards.

The etch rates for the two different out-of-plane components were determined as follows. Before etching, part of the sample was covered by photoresist, which is inert to HF and protects the film underneath. After the etching procedure the photoresist was dissolved by acetone and the edge of the etched region measured by AFM. In Fig. 6.2(a), the AFM image taken at the edge of the etched area, which was shown in Fig. 6.1 already, is displayed. From the scan line across the edge shown in Fig. 6.2(d), it can be seen that the remaining islands in the etched area, the domains with polarization downwards (P^-), are inert to the acid or at least almost unetched. The etch depth for the domain pointing upwards (P^+) was determined from the height histogram shown in Fig. 6.2(c). Two peaks are visible, one rather sharp peak, corresponding to the unetched area and as well to the domains P^- in the etched area, and one broader peak, corresponding to the etched domains P^+. The etch depth was extracted from the separation of the two peaks. The width of the peak corresponding to the etched domains is a measure for the morphology roughness after etching. The relatively high roughness is seen in AFM topography zoomed to the etched area in Fig. 6.2(b) too, and has been reported for other ferroelectric materials as well [156].

Four different HF concentrations were investigated. For each concentration six to eight different etch times were performed and the resulting etch depth plotted in Fig. 6.3(a). The etch depth was extracted for each data point by the histogram method described above. The error bars drawn in the figure are the corresponding full width at half maximum values of the peaks in the histogram. They correspond therefore to the roughness
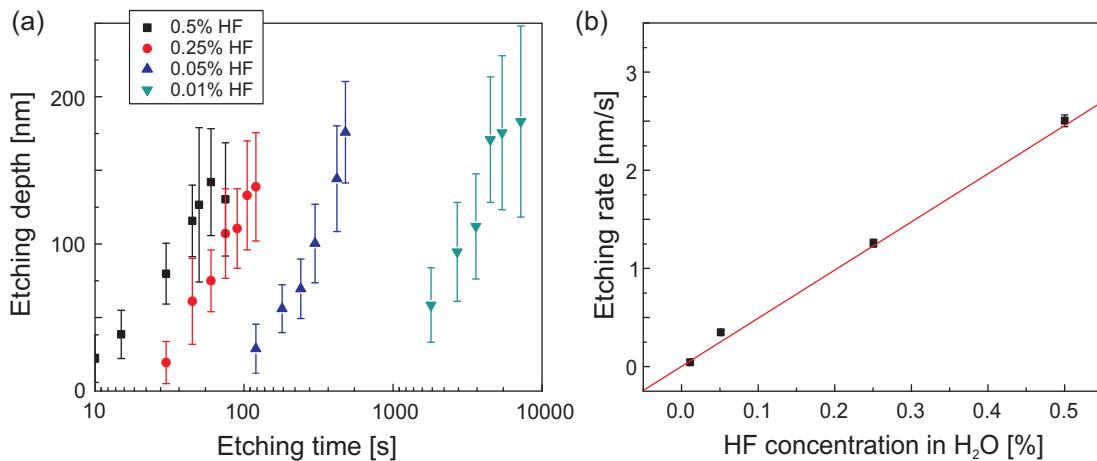
Figure 6.3: (a) Extracted etch depth for domains with an out-of-plane polarization component pointing upwards for various HF concentrations and etch times. (b) Etch rate versus HF concentration, extracted from linear line fits for each set of HF concentration listed in Tab. 6.1.

HF concentration [%]	Etch rate [nm/s]	Error from line fit [nm/s]
0.01	0.04	0.02
0.05	0.34	0.02
0.25	1.25	0.04
0.5	2.49	0.06

Table 6.1: Etch rates for domains with an out-of-plane polarization component pointing upwards for different HF concentrations.

of the etched area rather than an experimental error. For each set of HF concentration the etch rate was obtained by fitting a linear function to the data points. The extracted slopes are listed in Tab. 6.1 and plotted in Fig. 6.3(b). It can be seen, that for the here considered HF concentrations there is a linear relationship between the etch rate r and the HF concentration. This has not necessary to be the case, given that $LiNbO_3$ has a superlinear dependence of the etch rate on the HF concentration, though in general higher HF concentrations for $LiNbO_3$ were considered than here [156]. From the line fit in Fig. 6.3(b), a value for the etch rate r for domains P^+ can be given as

$$r = (5.0 \pm 0.1) \, \frac{\text{nm}}{s} \cdot [\% \, \text{concentration of HF}] \tag{6.1}$$

As already mentioned, the domains P^- are inert or at least almost unetched by the acid. Within the experimental accuracy no impact could be measured. After etching, the surface of the P^- domains is still as flat as before and the limit of the etch rate can be estimated to be at least 40-50 times slower than for the P^+ domains. The applied etch times and concentrations, however, were limited due to the small thickness of the BFO films. For too long times or too high concentrations some areas with domains P^+ or defects were etched completely to the bottom electrode, allowing the acid to attack the interface between BFO and SRO and often remove the complete film as a
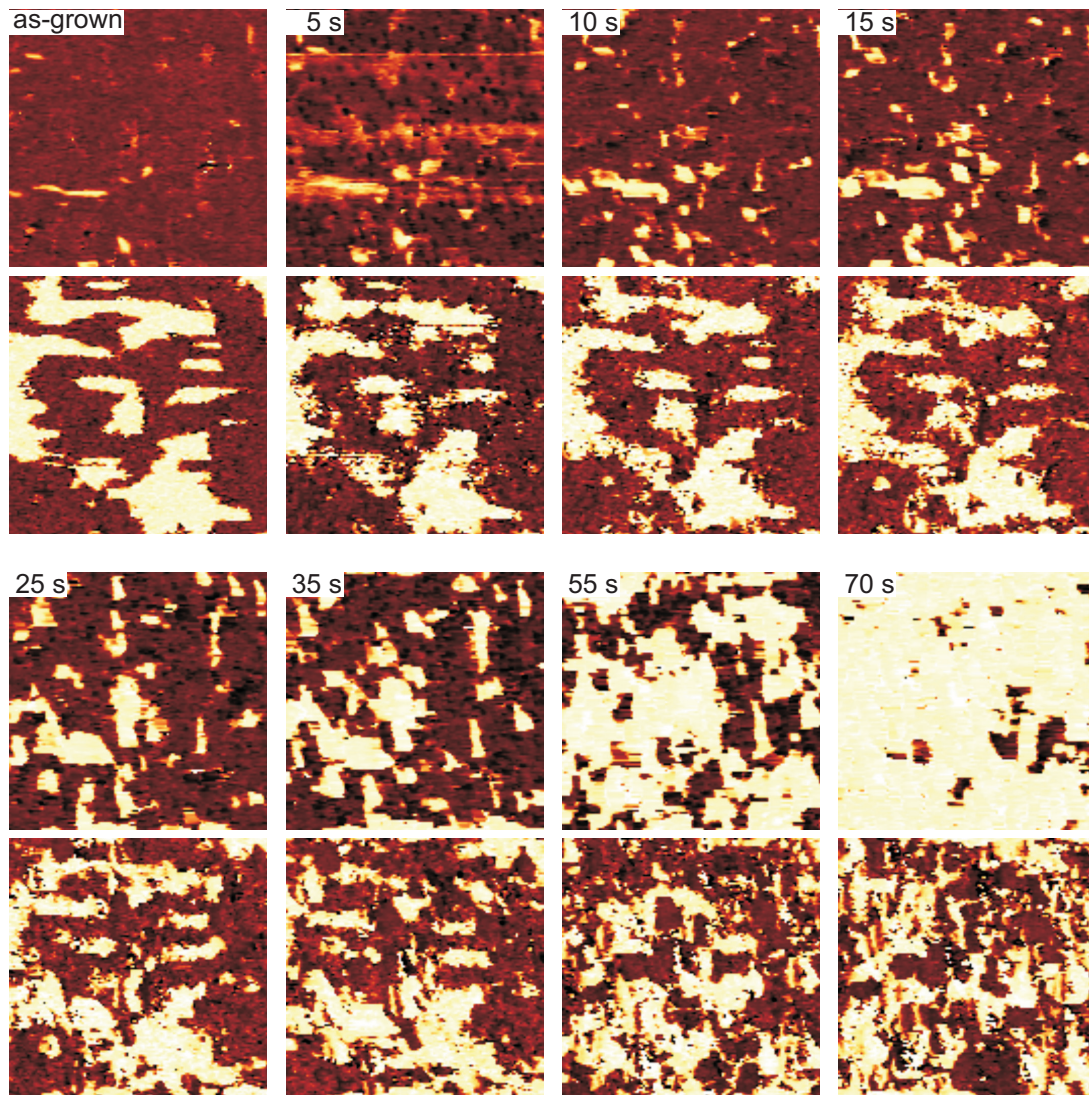
Figure 6.4: Several VPFM phase images (top) and LPFM phase images (bottom) of an approx. 200 nm thick BFO film on SRO buffered DSO acquired successively at the same location after different etch times in 0.5 % HF (the total etch time always given). All images are $2.5 \times 2.5\,\mu\mathrm{m}^2$.

consequence.[2] In the next section, another estimation for the limit of the etch rate of the P^- domains will be given, which will show that the etch ratio is even higher. For the further investigations here, the domains P^- are considered to be inert to HF. For an unambiguous clarification, however, etching investigations on single crystals should be done.

The following additional effect takes place while etching. As already visible in Fig. 6.1, after etching in HF the P^- domains have usually grown in size, that means the film switches under the effect of the acid. This effect is enhanced when the film becomes thinner. To observe the evolution of the down-switching effect the same location was imaged successively by PFM after several short etch times. Figure 6.4 shows VPFM phase images and LPFM phase images before etching and after etching in 0.5 % HF from an etch time of 5 s up to a total etch time of 70 s. It can be seen that the small existing

---

[2]This happened even for films with almost uniform P^- domains.

domains P^- laterally grow rapidly in size, but a few nucleations occurred at places where no P^- domains were visible in the pristine state as well. After about 70 s almost the complete film is switched downwards which terminates the etching.

The occurrence of a ferroelectric switching due to chemical environment has been reported already several times for other systems [126, 127, 161], in particular during etching of MgO-doped LiTaO$_3$ with HF. In the latter case the switching was attributed to a decrease of the compensation of the depolarization field by the etching process [125]. The switching of the BFO film under the HF exposure observed by us is therefore not unconceivable.

BFO and LiNbO$_3$ have a similar etch behavior under HF, which shall be examined a bit closer in the following. LiNbO$_3$ has a hexagonal or rhombohedral symmetry, identical to the one of BFO, although in case of LiNbO$_3$ only 180° domains are allowed due to its high rhombohedral distortion which hinders a ferroelastic switching ($\alpha_{rh}[\text{LiNbO}_3] = 55.87°$ [22] compared to $\alpha_{rh}[\text{BFO}] = 59.35°$). Therefore, in LiNbO$_3$ usually only crystals along the $[111]_c$ direction, which is called the z-axis, are considered. For LiNbO$_3$ the z^- face is etched by HF, whereas the z^+ is inert [156]. The z^- face corresponds to the P^- domains in BFO, and the z^+ face corresponds to the P^+ domains in BFO. Therefore, LiNbO$_3$ and BFO have in common that for both materials one side of the crystal along the direction of polarization is attacked by the acid while the other side is inert; however, it is the opposite side of the polarization with respect to each other.

As already mentioned, a general origin of differential etching has not been revealed so far. In case of LiNbO$_3$ a model has been developed, which relies on the assumption that etching is initiated by surface protonation [156], similar to the HF etching of SiO$_2$ [162]. The differential etch behavior in LiNbO$_3$ is then explained by the different likelihood of surface protonation of the two different domains, due to the positive proton charge and different surface charges in LiNbO$_3$ [156]. With these assumptions the dependence of the etch rate on different concentrations of HF and HNO$_3$ can be explained. However, the model can not be applied in general to all other materials, since the particular surface chemistry of each material system is of importance. In addition, this model can not explain the different etch behavior on the non-polar faces of LiNbO$_3$, and may therefore not be complete.

Another conjecture, which may contribute to the differential etch behavior and which holds for both LiNbO$_3$ and BFO, is, that at the surface the two domains P^- and P^+ have different metal–oxygen binding properties. Due to the different ion shifts, which are sketched for BFO in Fig. 2.5, different bond lengths between the metal ions, i.e. Bi^{3+} and Fe^{+3}, respectively, and the oxygen ions occur for the different domains. For the domains P^+, the Bi^{3+} ion has a short bonding length to the underlying oxygen plane, whereas the Fe^{3+} ion has a longer bonding length to the oxygen ions. For the domains P^-, the situation is the opposite, with a long bonding length for the Bi^{3+} ion and short bonding length for the Fe^{3+} ion. A shorter bonding length is usually a stronger and less reactive bond. Under the assumption that the acid can not break the short Fe^{3+}–oxygen bond, but it is able to break the longer bond as well as both Bi^{3+}–oxygen bonds, a contribution to the differential etch behavior may be attributed to this effect.

Another possible explanation for the differential etch behavior may be given in case a charge of certain polarity has to be provided so that the etch process can take place. At the surface of the ferroelectric material one kind of charge may accumulate due to a energy band bending which may exist for several reasons. One origin for a band bending is given by the ferroelectric polarization itself [163–165]. The different energy levels

at the surface influence the chemical reactivity and electron affinity [166]. It has been shown that this can be utilized for instance to deposit material related to the domain configuration [163,167,168]. In addition, all semiconductors, even non ferroelectric semiconductors, exhibit a band bending at an interface to a liquid phase, which is a result from different electrochemical potentials of the two phases [169]. Independent of the origin, band bending leads to an accumulation of one type of charge carries at the surface. In case one particular type of charge polarity is needed to complete the etch reaction, a differential etch behavior may be introduced. In the next section another evidence is given that charges may play an important role in the etch process.

6.2 Etching under light illumination

In this section the etch behavior of BFO in diluted HF under simultaneous illumination with light is presented. Two different effects were observed, first an etching of the domains P^-, which are inert to HF without light illumination, and in case of 71° stripe domains an enhanced etch rate at the domain walls.

As light source three different lasers were available, a red laser diode ($\lambda = 660\,$nm, $E = 1.88\,$eV, $8\,$mW), a green laser diode ($\lambda = 532\,$nm, $E = 2.33\,$eV, up to $100\,$mW), and a blue laser diode ($\lambda = 405\,$nm, $E = 3.06\,$eV, $< 1\,$mW). The band gap of BFO has been reported to be $2.67\,$eV, however, with an onset of absorption at $2.17\,$eV already [170,171]. The energy of the red laser is therefore below the band gap and onset, the green laser above the onset of absorption, and the blue laser is well above the band gap. The laser light was directed unfocused with an almost perpendicular incidence on the BFO sample in the acid.

The etching of the domains P^- was investigated in a $25\,$nm thin BFO sample on SRO buffered DSO substrate with a domain structure similar to the one shown in Fig. 4.13. In this BFO film a uniform out-of-plane component of polarization pointing downwards and a mosaic like domain pattern was seen in VPFM and LPFM, respectively. The sample was illuminated by the green laser light for which power densities up to $3.4\,$W/cm^2 could be chosen. The etch depth was evaluated in the same manner as the etch depth for the P^+ domains discussed in the last section.

Figure 6.5(a) shows the AFM topography acquired at the edge of the etched area, which was immersed to $0.05\,$% concentrated HF for $52\,$s while illuminated with a power density of $3.3\,$W/cm^2. In the scan line shown in Fig. 6.5(b) as well as in the histogram used for the etch depth determination shown in Fig. 6.5(c) it is apparent that the film with uniform domains P^- was etched, in contrast to the observations in Sec. 6.1. Figure 6.5(d) shows the dependence of the logarithmic etch depth on the applied power density. It can be seen that the points follow a straight line. The etch depth d has therefore an exponential dependence on the applied power density I, and can be expressed after $\approx 53\,$s in $0.05\,$% concentrated HF with the help of the line fit as

$$\ln(d\,[\text{nm}]) = I \times (1.48 \pm 0.09)\,\text{cm}^2/\text{W} + (-2.4 \pm 0.3) \tag{6.2}$$

The line can be extrapolated to zero light intensity to obtain another estimation for the etch rate of the P^- domains without light. In case the highest etch depth within the error is taken, an etch rate of $0.14\,$nm/min for $0.05\,$% concentration of HF is obtained, which is a factor ≈ 150 smaller than the etch rate of P^+ domains at this concentration.

(a)

(c)

(b)

(d)
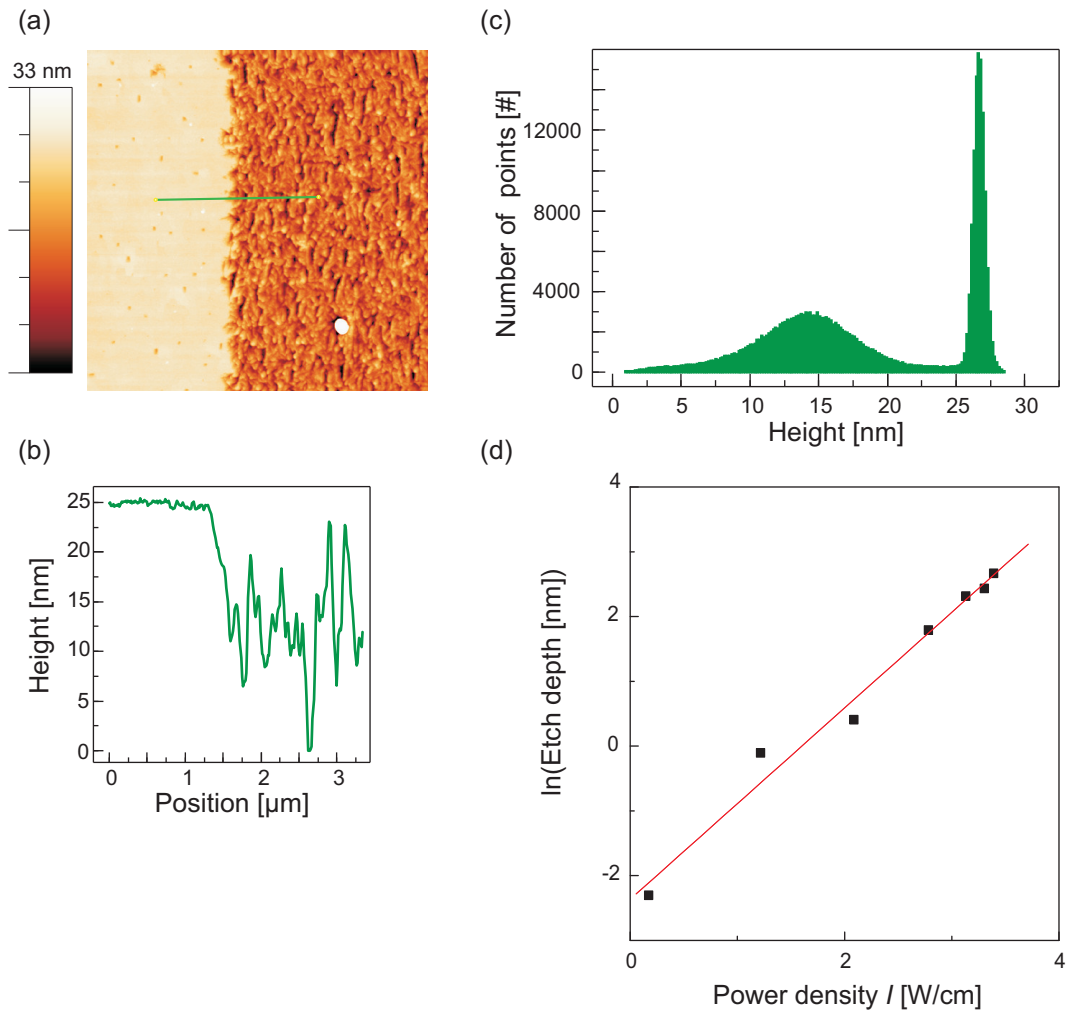
Figure 6.5: (a) Topography of 25 nm thick BFO film on SRO buffered DSO substrate after 52 s in 0.05 % concentrated HF and 3.3 W/cm^2. Image is $7 \times 7\,\mu$m^2. (b) The corresponding scan line and (c) the corresponding height histogram. (d) Dependence of the etch depth of P^- domains in 0.05 % HF for approx. 52-55 s on the power density of 532 nm laser light.

For the highest applied power density of 3.4 W/cm^2 an etch rate of 0.29 nm/s was determined, which is about 85 % of the etching rate measured for P^+ domains in 0.05 % concentration HF without illumination in Sec. 6.1. Therefore, with light illumination a similar efficient etching rate for the P^- domains can be achieved.

A possible origin of the etch behavior under light illumination shall be addressed in the following. The green laser light will be mainly absorbed in the BFO layer by generating of electron-hole pairs. A possible heating of the sample due to the absorption of the laser can be estimated to be less than a few degrees [172], in case a thermal conductivity in the order of other perovskite materials, such as STO or SRO [173, 174], is assumed for BFO. An enhanced etch rate due to elevated temperature can therefore be neglected as origin. However, the electrons and the holes may be separated by the band bending at the surface, which may hinder a direct recombination. This supports the conjectures described in the last section. On the one hand additional charges are now available at the surface which may be needed for the etch process to take place. On the other hand,

even the metal–oxygen bonds at the surface may be influenced, since electrons, which are involved in the covalent bonding, are either released or accumulated.

A further novel effect is seen for etching of BFO samples with 71° stripe domains and simultaneous light illumination. For this investigation a 120 nm thick BFO film on SRO buffered DSO substrate was employed, which had a domain structure similar to the film shown in Fig. 4.18(a). The VPFM image revealed an almost uniform out-of-plane component of the polarization pointing downwards, apart from several lines of opposite polarization direction. In the LPFM image the typical 71° stripe domain pattern was visible. During etching in 0.05 % concentrated HF and simultaneous illumination with a rather low laser power density of 0.17 W/cm^2 at 532 nm for 15 min the etch rate was slightly amplified at the 71° domain walls. The topography in Fig. 6.6(a) and in particular the error image in Fig. 6.6(b) acquired after etching show, apart from the deep holes originating from the domains with polarization component upwards, small grooves of 1-2 nm depth, which match exactly the domain walls of the 71° stripes seen in the LPFM image shown in Fig. 6.6(c). In case the power density is increased, the grooves become deeper as well, as shown for 1.7 W/cm^2 in the topography image in Fig. 6.6(d) and its corresponding scan line in Fig. 6.6(e). The adjacent domains, which have an out-of-plane polarization component pointing downwards, get attacked with the help of the light by the acid as well, according to the investigations shown in Fig. 6.5(d). The average etch depth, extracted from AFM images acquired at the edge of the etched area (not shown here), is about 16 nm, close to the determined depth of 19 nm by Eq. (6.2). The domain walls, as can be seen in the scan line in Fig. 6.6(e), are etched additional 8-10 nm deep, which is in total about 1.5 of the bulk domain etch rate. The etch grooves at the domain walls are seen as well for illumination with red laser light (660 nm) and blue laser light (405 nm). For the red laser light, the topography after etching is shown in Fig. 6.6(f) with the corresponding line scan in Fig. 6.6(g).

The enhanced etch rate at the 71° stripe domain boundaries speaks again for the assumption that charges play an important role in the etch process, since other reports showed that photo-generated electrons and holes accumulate at the 71° domain walls due to their unique properties [175]. It should be pointed out, that the energy of the red laser light is below the band gap of BFO, still the 71° domain walls are attacked by the acid. One possible explanation is that the red light is absorbed by defects, which have energy levels lying in the band gap. It has been reported for instance, that oxygen vacancies act as a double donor with an energy level positioned 0.6 eV below the band gap [176]. The generated charge carriers may still accumulate at the domain walls or more defects may be present in the vicinity of the domain wall in the first place. A further explanation may be given by a lower band gap at the domain wall itself. It has been reported that the conduction band can be lowered by up to 20 %, which may be sufficient to allow the absorption of the red light in the domain wall directly [8, 177, 178].

Summarizing, with simultaneous light illumination a new etch behavior occurs. The initially inert P^- domains get attacked by HF if illuminated by sufficiently high power densities, shown for laser light with a wavelength of 532 nm. In addition, the domain walls in 71° stripe domain patterns show an enhanced etch rate. One example how this new behavior can be utilized is shown in the next section.
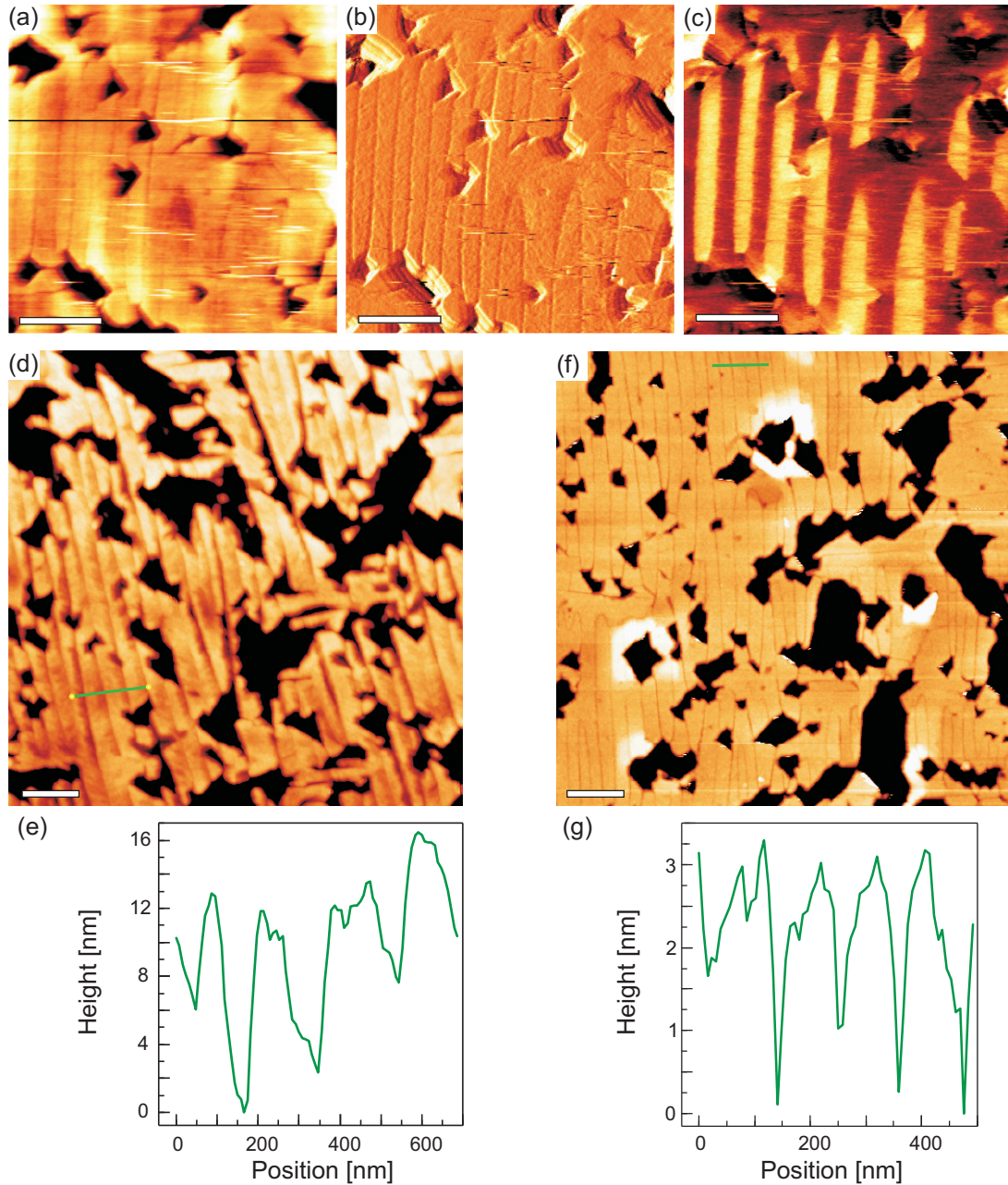
Figure 6.6: Etching of an approximately 120 nm thick BFO film on SRO buffered DSO with 71° stripe domains with simultaneous light illumination. (a) Topography, (b) error image, and (c) LPFM image after 15 min in 0.05 % HF and illumination ($\lambda = 532$ nm, $I \approx 0.17$ W/cm^2). (d) AFM topography acquired in tapping mode and (e) corresponding scan line after 15 min in 0.05 % HF and light illumination ($\lambda = 532$ nm, $I \approx 1.7$ W/cm^2), and (f) topography and (g) scan line after 15 min in 0.05 % HF and light illumination ($\lambda = 660$ nm, $I \approx 0.35$ W/cm^2). All scale bars are 500 nm.

6.3 Fabrication of epitaxial BFO submicron structures

In this section it is shown how the differential etch behavior discussed in Sec. 6.1, and as well the additional etch behavior under light illumination can be employed for submicron structure fabrication.

The most straightforward way to fabricate epitaxial bismuth ferrite structures by differential etching relies on two steps. First, the desired structure has to be poled in an epitaxial BFO film as a pattern consisting of P^- domains surrounded by P^+ domains. Then, the sample is immersed in HF to reproduce the domain structure in the film morphology due to the high differential etch ratio. For instance, the fabrication of a $500 \times 500\,\text{nm}^2$ structure is shown in Figure 6.7. A $200\,\text{nm}$ thick BFO film deposited on SRO buffered DSO was used as a basis. First an area of $2 \times 2\,\mu\text{m}^2$ was poled upwards by scanning this area with the AFM tip while applying a DC voltage of $-8\,\text{V}$ to the tip. Subsequently, a square area of $500 \times 500\,\text{nm}^2$ was poled downwards by applying $+8\,\text{V}$. The final domain state with topography, VPFM image and LPFM image is shown in Fig. 6.7(a-c), respectively. It consists of a $500 \times 500\,\text{nm}^2$ square P^- domain surrounded by P^+ domains. While the out-of-plane component can be controlled by the applied voltage, the in-plane component comes out with arbitrary direction. For the following etch step the in-plane domains play no role though, as discussed in Sec. 6.1. The topography, VPFM image and LPFM image after $45\,\text{s}$ in $0.5\,\%$ concentrated HF are shown in Fig. 6.7(d-f). It can be seen that the poled structure from VPFM is transferred to the morphology. Within the structure, the domain state did not change. On the other hand, around the structure the BFO film has switched after an average etch depth of about $120\,\text{nm}$ completely to P^- domains which terminated the etching. The down-switching is often accompanied by a lateral switching as well, as it was shown in Sec. 6.1 already. The scan line across the fabricated structure, taken at the position indicated by a green line in Fig. 6.7(d), is shown in Fig. 6.7(g). One drawback of this fabrication method is, that due to the backswitching, the film was not etched down to the bottom electrode. Consequently, the obtained BFO structure is not free-standing, but incorporated in a thinner BFO film as sketched schematically in Fig. 6.7(h).

Nonetheless, a nice property of this fabrication method lies in the possibility to achieve structures with shapes of any kind, in a direct manner without the employment of any optical lithography for instance. Two examples are given in Fig. 6.8. The irregular shape of the logo of the Max Planck Institute of Microstructure Physics ($\mu\Phi$) was poled as domain structure into the BFO film, as shown in Fig. 6.8(a). Subsequently, the domain pattern was transferred into the film morphology by differential etching (Fig. 6.8(b)). Another example given is an array of nanostructures, as seen in topography after etching in Fig. 6.8(d), which was achieved by previously applying voltage pulses to the BFO film (see Fig. 6.8(c)).

One of the smallest achieved nano structures is shown in Fig. 6.9. The structure was fabricated by first poling a $200 \times 200\,\text{nm}^2$ domain in the BFO film and subsequent etching for $45\,\text{s}$ in $0.5\,\%$ concentrated HF. Figure 6.9(a) shows the obtained topography image with the corresponding scan line in Fig. 6.9(d). It can be seen that the top of the structure is not flat anymore, but it has a rounded profile due to uncontrolled side wall etching. The full width at half maximum is about $170\,\text{nm}$. In case this value is taken to evaluate the aspect ratio of the structure, a value of ≈ 0.7 is obtained. Remanent piezoelectric hysteresis loops were measured on top of the nanostructure. A comparison with a hysteresis loop acquired on the untreated film is shown in Fig. 6.9(e). It is
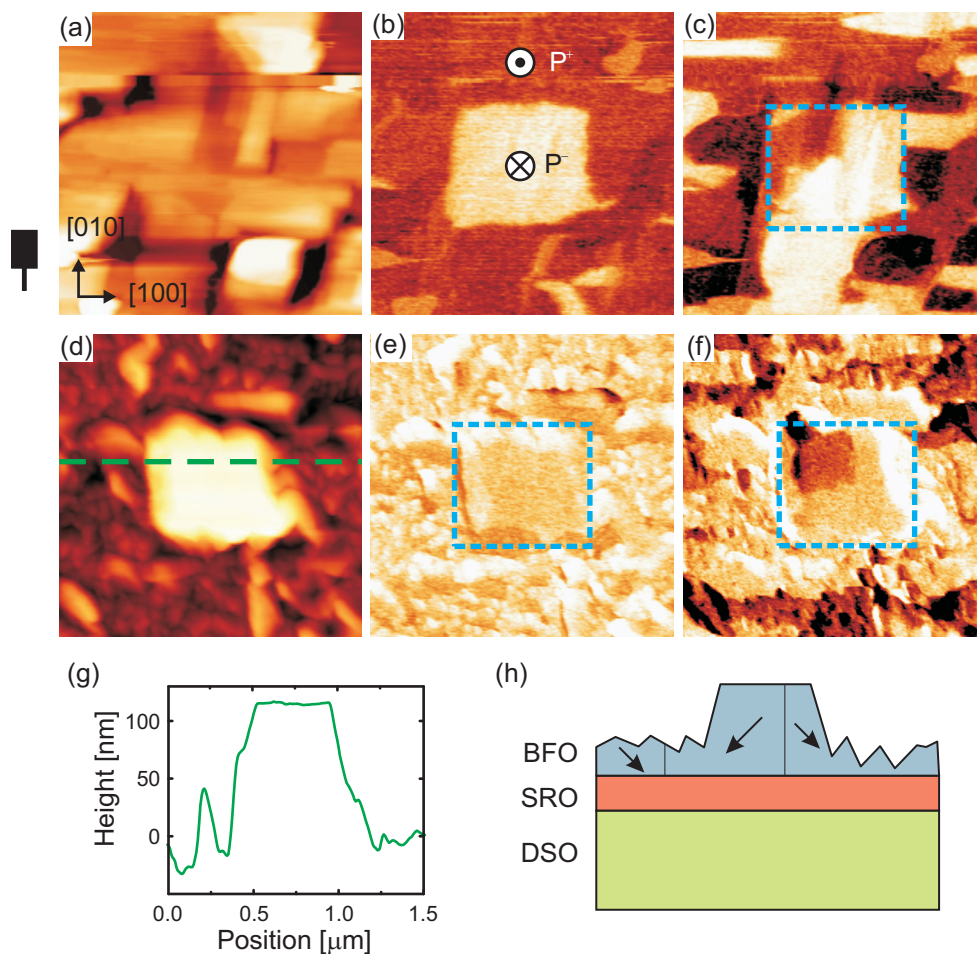
Figure 6.7: (a) Topography (color scale is 20 nm), (b) VPFM image and (c) LPFM image of a 200 nm thick BFO film grown on SRO/DSO(110)$_o$ after poling with the AFM tip. (d) Topography (color scale is 180 nm), (e) VPFM image and (f) LPFM image after etching for 45 s in 0.5 % concentrated HF. (g) Scan line taken across the structure as indicated in (d) by the green line. (h) Cross section sketch of the final structure. All images are $1.5 \times 1.5\,\mu m^2$.
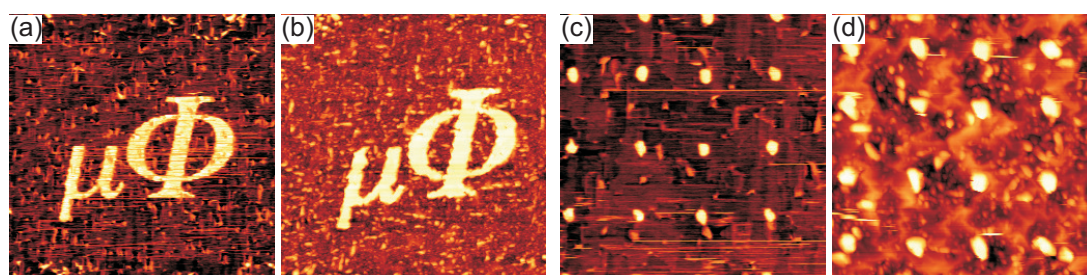
Figure 6.8: Variety of shapes achievable for structures fabricated by differential etching. (a) VPFM image after poling and (b) resulting topography after etching for 45 s in 0.5 % HF, showing the logo of the institute. Image sizes are $10 \times 10\,\mu m^2$. (c) VPFM image and (d) resulting topography after etching for 30 s in 0.5 % HF, showing an array of nanostructures. Image sizes are $4 \times 4\,\mu m^2$.
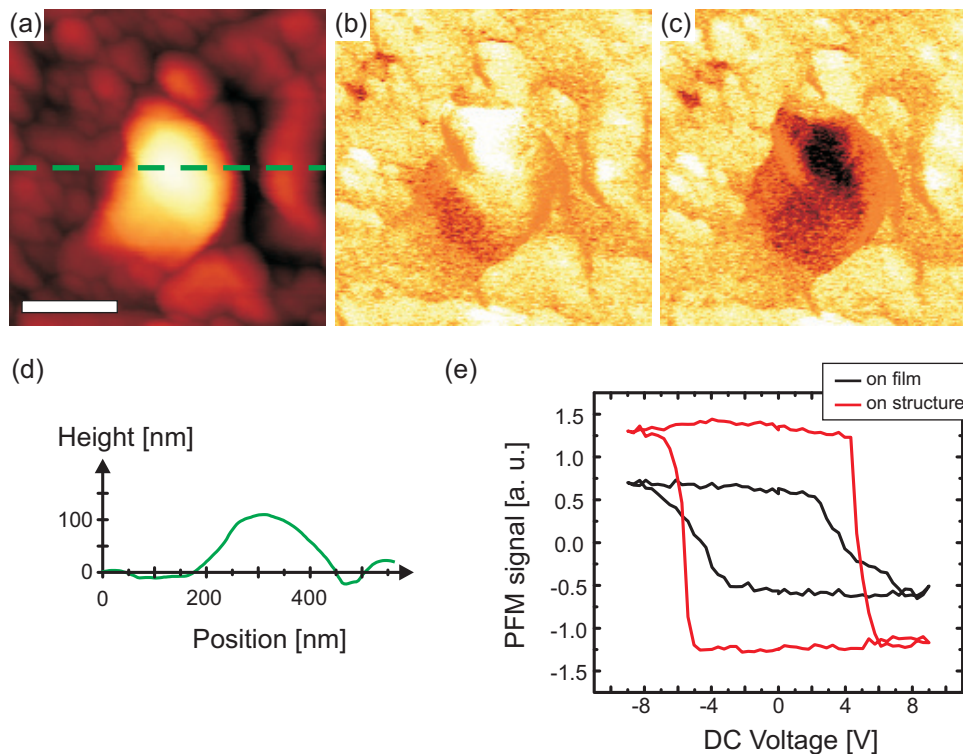
Figure 6.9: (a) Topography, (b) VPFM image before and (c) after poling of smallest achieved nanostructure. (d) Scan line corresponding to the green line shown in (a), shown with same x and y scale. (e) Piezoelectric hysteresis measurement measured in the middle of the structure and on the untreated film.

apparent that the nanostructure has good switching characteristics with similar switching voltages as in the film. The piezoelectric response, however, is enhanced. An enhanced piezoelectric response has been reported already on $Pb(Zr,Ti)O_3$ nanostructures [179, 180], and was attributed to two effects: (i) an enhanced mobility of the $90°$ domain walls in $Pb(Zr,Ti)O_3$ [181] and (ii) a removal of the clamping effect of the surrounding material [182]. The calculations done for $Pb(Zr,Ti)O_3$ in Ref. 182 predict an increase of piezoelectric response for aspect ratios above 0.1. It is therefore reasonable to argue, that the enhanced piezoelectric response in the BFO structure here is due to the removed clamping effect as well.

Figures 6.9(b) and (c) show the VPFM image before and after the performed hysteresis measurement, respectively. The hysteresis measurement left the film in the opposite state. It can be seen that the complete nanostructure was switched. Even after one week no retention loss could be detected, proving the good switching and retention properties of the fabricated nanostructure.

A further approach for structure fabrication, which is suited for large-scale patterning as well, was carried out employing the etch behavior of BFO under simultaneous light illumination. The idea relies on a BFO film with P^- domains, hence technically inert to HF alone, and a mask which protects the intended structure. The BFO film is then exposed to the acid with light illumination, resulting in removal of material at the unprotected locations. Figure 6.10 shows as example the fabrication of an array of epitaxial submicron structures. As mask an array of 20 nm thick gold dots was thermally evaporated through 800 nm wide silicon nitride stencils [183,184], which are commercially
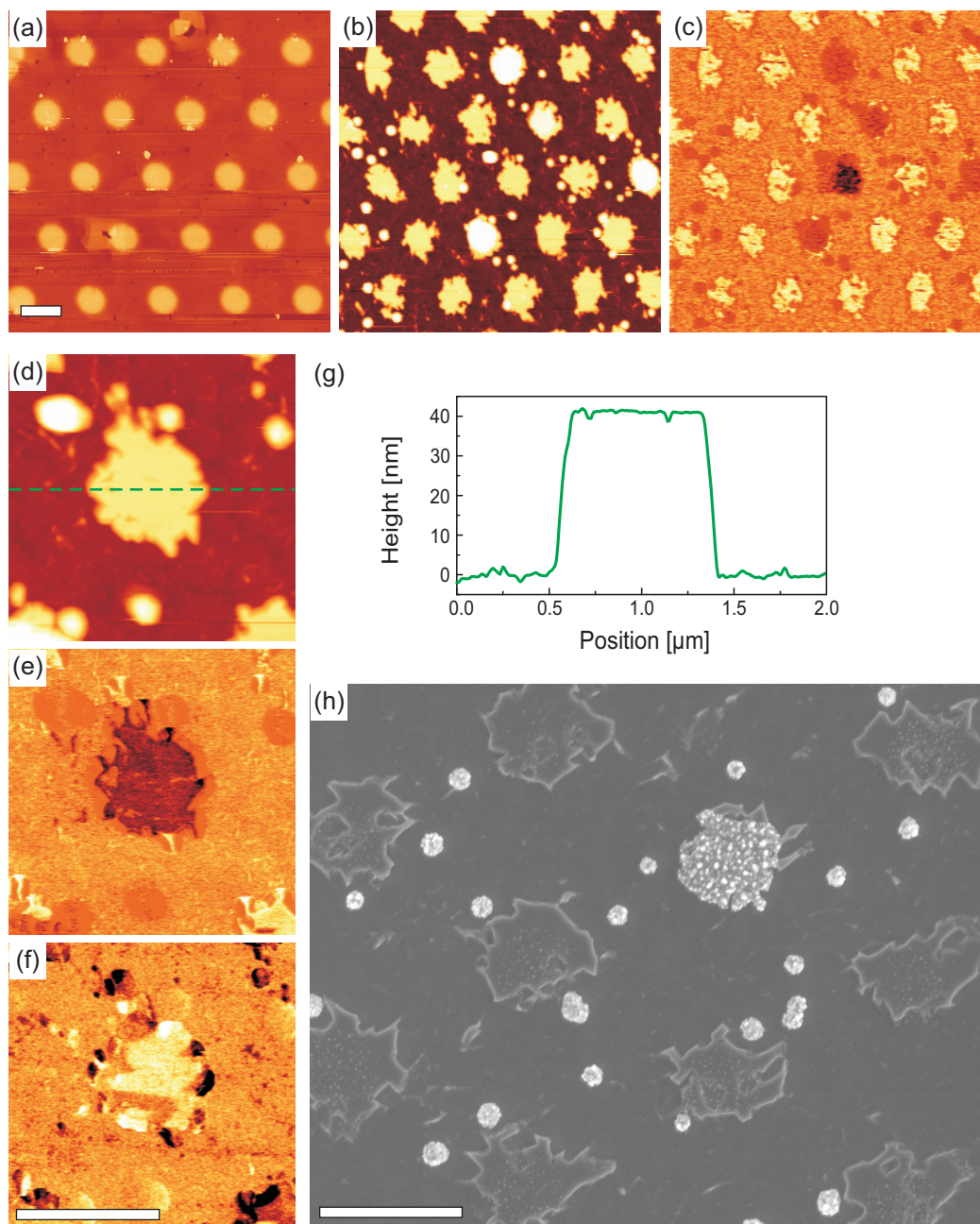
Figure 6.10: (a) Topography of BFO film with an array of 20 nm high and 800 wide Au dots. (b) Topography (c) VPFM image after light assisted etching. (d) Topography with corresponding scan line in (g), and (e) VPFM image and (f) LPFM of the switched structure. (g) SEM image of the fabricated structures. All scale bars are 1 μm.

available from Aquamarijn BV, Netherlands. The resulting surface morphology of the Au dots on the BFO film is shown in Fig. 6.10(a). As next step, the sample was etched for 8 min in 0.05 % concentrated HF with illumination (3.4 W/cm² at 532 nm). As final step, the gold dots were removed by a gold etch solution from Alpha Aesar. Figures 6.10(b) and (c) show the topography and VPFM image of the final structures, respectively. In a few cases the gold dots were not removed by the gold etching solution, which can be seen as brighter dots in topography and reduced PFM signal in the VPFM image. Most dots, however, give a good piezoresponse with an out-of-plane component of the polarization

still pointing downwards, except for one structure which has been poled upwards before. This fabrication method has the advantage, that the complete film is etched down to the bottom electrode, which is inert to the acid. The scan line across the structures shown in Fig. 6.10(g) reveals that the top of the structure is maintained very flat, which holds for the etched region as well, since the film was etched completely to the bottom electrode. The disadvantage, however, are limitations in the minimal lateral size. A zoom to the poled structure with topography, VPFM image and LPFM in Fig. 6.10(d-f), respectively, shows that the structure is non-uniformly shaped. The irregular shapes of the BFO structures are even better seen in the SEM image shown in Fig. 6.10(h). In addition, one unetched gold dot is clearly visible together with a few gold particles which have not been removed. The irregular shapes of the BFO structures speak for an uncontrolled sidewise etching under the gold protection mask, which prevents the fabrication of much smaller structures by this method.

6.4 Summary

In this chapter the differential etch behavior of epitaxial thin BFO films under exposure to diluted HF was discussed. The P^- domains are inert to the acid, whereas the P^+ domains are etched by approximately $5\,\mathrm{nm}\,\mathrm{s}^{-1}[\%\,\mathrm{HF}]$ for the considered HF concentrations of up to $0.5\,\%$. It was shown that the P^+ domains experience a loss of retention while exposed to the acid and switch gradually to P^- domains, which happens more dramatically for thinner BFO films. The differential etch behavior can be employed to fabricate submicron sized epitaxial BFO structures, by first poling the desired shape into the BFO film and subsequently transferring the domain pattern to the film morphology by differential etching. One drawback is that the films switch to uniform P^- domains after a certain etch depth which prevents the fabrication of free-standing structures. In addition, the aspect ratio of the structure is limited to values < 1 due to rounding of the top and sidewall etching.

A further etch behavior occurs in case the sample is illuminated with light during etching. For sufficiently high power densities, with an energy higher than the onset of absorption in BFO, the P^- domains get etched with a similar efficiency as the P^+ domains without illumination. For BFO samples with 71° stripe domains a further amplified etch rate at the domain walls is seen. The latter effect is even seen for red laser light, whose energy is below the band gap of BFO. This points to a possible role of defects, such as oxygen vacancies, or a reduced band gap at the domain wall. The additional etch behavior with light illumination can be employed for structure fabrication as well. A protective mask is deposited on a BFO sample with P^- domains and the unprotected film can be removed by light-assisted etching. A proof of concept is given by the fabrication of an array of approx. 800 nm wide BFO structures. With this method free-standing structures on a large scale can be achieved, though the lateral size of each structure is limited due to a sidewise etching under the gold protection mask.

7

Summary and outlook

Bismuth ferrite is one of the most studied multiferroic materials, owing to its strong ferroelectricity and its antiferromagnetic ordering at room temperature. In the recent years not only the bulk domain properties of BFO were investigated, but the focus of research moved towards the investigation of its domain walls and domain patterns. It has been observed that particular domain patterns, in particular the 71° and 109° stripe domains, can exhibit functional properties which either are absent in the surrounding bulk domains or rely on the special domain configuration.

In this thesis three different topics were addressed. First, the influence of different boundary conditions on the domain formation in epitaxial BFO thin films deposited by PLD was investigated. Due to the eight possible ferroelectric domains in BFO many complex domain patterns can form. It was shown to what extent the domain pattern can be controlled by the boundary conditions in order to achieve a desired domain pattern. Second, the switching properties of the 71° stripe domains in BFO, which is one of the domain patterns showing new functionalities, were examined. The reliability of these domain patterns upon electric switching is an important issue with respect to a potential utilization in future devices. Last, the differential etching of BFO under HF was addressed. A new etch behavior under light illumination and the possibility of structure fabrication were reported. A detailed summary of all results and an outlook to possible further investigations are given in the following.

Influence of boundary conditions on the domain formation in epitaxial BFO thin films

Epitaxial BFO thin films were grown by PLD on low miscut $STO(001)_c$, $DSO(110)_o$, $GSO(110)_o$, and $SSO(110)_o$ substrates. Depending on the desired configuration, the BFO film was deposited directly on the substrate, or a conductive SRO bottom electrode was deposited first. The BFO growth mode and domain structure differed whether or not a SRO bottom layer was present.

In case the BFO film was grown directly on the substrate, the substrate symmetry and surface termination had the main effect on the domain formation. On all substrates a 3D growth was observed. In case of STO substrate the BFO domain pattern consisted of all four structural variants, preferably with an out-of-plane polarization compo-

nent pointing upwards.[1] The ferroelectric domains exhibited a cubic mosaic-like pattern which coincided with the features seen in topography. In contrast, the BFO films on all REScO$_3$ substrates showed a selection of only two structural variants. It was shown by XRD-RSMs that the structural variants r_3 and r_4 were imposed by the orthorhombic symmetry of the substrates, whose orthorhombic unit cells consist of monoclinically distorted pseudocubes. In case the REScO$_3$ substrates were annealed in air prior to BFO film deposition 109° domains formed, which were built up by the mentioned structural variants and aligned along the $[1\bar{1}0]_o$ axis. In addition, for the tensile strained BFO films a rotation of the pseudocubic unit cell was observed with increasing film thickness, which showed a transition from an "unbonded" configuration to a "parallel" alignment. In case the DSO substrate was annealed in O$_2$ atmosphere, instead of 109° stripe domains, 71° stripe domains formed, which were built up from the same structural variants and are rotated by 90° in the sample plane with respect to the 109° stripe domains, in agreement with the theory of Streiffer. The transition was attributed to a different surface termination of DSO due to the different annealing procedure, which, however, should be subject of further studies with the possibility to determine the surface termination for an unambiguous proof. In addition, the effect of annealing in O$_2$ atmosphere on the other REScO$_3$ substrates was not investigated and may give further insight in the mechanisms behind the domain formation.

In case the substrates were buffered with SRO first, the growth mode of the BFO films changed to a step-flow growth, which may be a result of a higher surface diffusivity on the A-site terminated SRO layer. For all films an out-of-plane polarization component of BFO pointing towards the SRO bottom electrode was observed, which is in agreement with the valence mismatch model. On STO and DSO substrates similar domain patterns were visible. For thin BFO films a mosaic-like domain pattern formed, built up with two preferential structural variants. The selection is in this case driven by the substrate miscut direction, which imposes the epitaxial orientation of the SRO layer. For thicker BFO films the domain wall energy becomes more important and 71° stripe domains form. The direction of the 71° stripes may again be a result of the substrate miscut direction. For BFO films on SRO buffered GSO and SSO substrates, however, a completely mosaic-like domain pattern formed, which originated from the bad surface morphology of the SRO films on these substrates.

In conclusion, the BFO domain formation depends on many boundary conditions which compete against each other. The substrate symmetry, the substrate miscut direction, the substrate surface termination, the type of interface and its properties, the growth mode, and the domain wall compatibility all influence the domain formation and may be utilized to a certain extent to achieve a desired domain structure.

Stability of 71° stripe domains of BFO upon repeated electrical switching

The 71° stripe domain patterns have a net polarization which has a component in the sample plane and a component perpendicular to the sample plane. Both components can be switched, either the in-plane component between in-plane electrodes, or the out-of-plane component in plane-parallel capacitors. For this, two different types of samples were needed, a BFO film with 71° stripes without bottom electrode and a BFO film with 71° stripes with bottom electrode. With the help of the boundary conditions discussed

---

[1]Though it should be noted that other groups reported a polarization downwards and a transition to two structural variants for thicker films [185].

before, BFO films on DSO substrate for the in-plane configuration and BFO films on both SRO buffered DSO substrate and SRO buffered STO substrate were grown.

The two configurations showed very different behavior in the stability upon repeated electrical switching. In the in-plane configuration the domain pattern did hardly change upon switching, even after 5×10^5 cycles and independent of the applied pulse frequencies up to 100 kHz. In addition, the macroscopic ferroelectric switching properties tended to improve with increasing number of switching cycles.

In contrast, in the out-of-plane configuration a transition to a new domain pattern took place successively. For frequencies ≤ 1 kHz the 71° stripe domain pattern was maintained, though the stripe width doubled within the first 1,000 to 2,000 cycles and the coherent areas with the same net in-plane polarization grew laterally. For higher switching frequencies these coherent areas first shrank and then the stripe domains were destroyed completely, leaving a mosaic-like domain pattern. The critical frequency seemed to depend on the strain state in the film and the amount of defects, but was in the order of 0.1 kHz to 1 kHz. The macroscopic electrical properties worsened with increasing switching cycles, i.e. the coercive voltages increased.

The differences in the two configurations were explained partly by their different geometrical design, which results in different amount of nucleation centers and therefore a different switching kinetics. Further evidence that the electrode separation plays an important role in the switching process, for instance by charge injection, was reported and may add to the differences seen for the two different configurations. The role of point defects, in particular oxygen vacancies, was discussed in relation to the frequency dependence of the out-of-plane configuration, since the oxygen vacancies were reported to play a crucial role in the switching process.

For a further insight, time resolved investigations would be of interest, which were not done here. The usual way to obtain time resolved information with PFM is based on the application of short voltage pulses with different length and subsequent imaging of the domain evolution, which is challenging to access here: In case of the in-plane configuration the film was switched already completely for the shortest available pulse width, and in case of out-of-plane measurements the domain state after releasing the voltage was not stable enough to draw reliable conclusions. In case shorter pulse widths are available, or by spending effort to stabilize the domain state in the out-of-plane configuration (for instance with an adjusted top electrode), further conclusions may be drawn.

Differential etch behavior of BFO and fabrication of epitaxial submicron structures

It was shown that BFO exhibits a differential etch behavior under exposure to HF, which is similar to the one of $LiNbO_3$. Domains P^-, which have an out-of-plane component of the polarization pointing downwards, are inert to HF, whereas the opposite domains P^+ are attacked by HF. The etch rate was determined to be 5 nm s^{-1}[% HF] at the considered HF concentration of up to 0.5 %. This behavior was employed to fabricate epitaxial submicron structures, which was shown to be an easy and direct fabrication method. The drawbacks, however, are a maximum aspect ratio of < 1 and the loss of retention of P^+ domains in the acid.

A new etch behavior was found for simultaneous illumination with light. For sufficiently high power densities the P^- domains were attacked by HF with a similar etch

rate as the P^+ domains experienced without light illumination. The possible role of charges, which may accumulate at the surface due to an energy band bending, in the etch process was discussed. In addition, BFO samples with 71° stripe domains exhibited enhanced etch rates at the domain walls, proving once again the unique properties of these domain patterns. It was shown how this new etch behavior can be applied to fabricate structures by depositing a protection mask first and subsequent light assisted etching.

Experiments which may give further insight into the etch behavior may include the application of a voltage during etching. This voltage alters the bend bending at the surface of the BFO film in contact with the acid and may allow to control the type and amount of charges at the surface. In addition, it seems feasible to stabilize the P^+ domains by the application of a voltage and therefore improve the etch behavior. Furthermore, different acid compositions, such as a mixture of HF and HNO_3 which is often used for $LiNbO_3$, may improve the etch behavior as well, though a huge parameter space of many possible combinations of acids and concentrations exist.

Although BFO has been investigated intensively in the last decades, new effects keep being revealed, including the discoveries presented in the thesis here. In particular, the new functionalities found in domain walls and domain patterns may be promising for new devices. The research of the ferroelectric/ferroelastic domain walls and patterns has just begun in the last years, and it can be expected that further unique properties will be discovered in the future. Nevertheless, several challenges, such as the full control of the domain patterns, the stability upon switching and further miniaturization, have to be overcome and will assumedly be topics of further research.

Bibliography

[1] W. Eerenstein, N. D. Mathur, and J. F. Scott, "Multiferroic and magnetoelectric materials", *Nature* **442**, 759 (2006).

[2] R. Ramesh and N. A. Spaldin, "Multiferroics: progress and prospects in thin films", *Nat. Mater.* **6**, 21 (2007).

[3] M. Fiebig, "Revival of the magnetoelectric effect", *J. Phys. D: Appl. Phys.* **38**, R123 (2005).

[4] N. A. Spaldin and M. Fiebig, "Materials science: The renaissance of magnetoelectric multiferroics", *Science* **309**, 391 (2005).

[5] N. A. Hill, "Why are there so few magnetic ferroelectrics?", *J. Phys. Chem. B* **104**, 6694 (2000).

[6] G. Catalan and J. F. Scott, "Physics and applications of bismuth ferrite", *Adv. Mater.* **21**, 2463 (2009).

[7] J. Seidel, L. W. Martin, Q. He, Q. Zhan, Y. H. Chu, A. Rother, M. E. Hawkridge, P. Maksymovych, P. Yu, M. Gajek, N. Balke, S. V. Kalinin, S. Gemming, F. Wang, G. Catalan, J. F. Scott, N. A. Spaldin, J. Orenstein, and R. Ramesh, "Conduction at domain walls in oxide multiferroics", *Nat. Mater.* **8**, 229 (2009).

[8] J. Seidel, P. Maksymovych, Y. Batra, A. Katan, S.-Y. Yang, Q. He, A. P. Baddorf, S. V. Kalinin, C.-H. Yang, J.-C. Yang, Y.-H. Chu, E. K. H. Salje, H. Wormeester, M. Salmeron, and R. Ramesh, "Domain wall conductivity in La-doped $BiFeO_3$", *Phys. Rev. Lett.* **105**, 197603 (2010).

[9] S. Farokhipoor and B. Noheda, "Conduction through 71° domain walls in $BiFeO_3$ thin films", *Phys. Rev. Lett.* **107**, 127601 (2011).

[10] Q. He, C.-H. Yeh, J.-C. Yang, G. Singh-Bhalla, C.-W. Liang, P.-W. Chiu, G. Catalan, L. W. Martin, Y.-H. Chu, J. F. Scott, and R. Ramesh, "Magnetotransport at domain walls in $BiFeO_3$", *Phys. Rev. Lett.* **108**, 067203 (2012).

[11] S. Y. Yang, J. Seidel, S. J. Byrnes, P. Shafer, C.-H. Yang, M. D. Rossell, P. Yu, Y.-H. Chu, J. F. Scott, J. W. Ager III., L. W. Martin, and R. Ramesh, "Above-bandgap voltages from ferroelectric photovoltaic devices.", *Nat. Nanotechnol.* **5**, 143 (2010).

[12] J. T. Heron, M. Trassin, K. Ashraf, M. Gajek, Q. He, S. Y. Yang, D. E. Nikonov, Y.-H. Chu, S. Salahuddin, and R. Ramesh, "Electric-field-induced magnetization reversal in a ferromagnet-multiferroic heterostructure", *Phys. Rev. Lett.* **107**, 217202 (2011).

[13] G. Catalan, J. Seidel, R. Ramesh, and J. F. Scott, "Domain wall nanoelectronics", *Rev. Mod. Phys.* **84**, 119 (2012).

[14] E. Salje and H. Zhang, "Domain boundary engineering", *Phase Transit.* **82**, 452 (2009).

[15] E. K. H. Salje, "Multiferroic domain boundaries as active memory devices: Trajectories towards domain boundary engineering", *ChemPhysChem* **11**, 940 (2010).

[16] S. Farokhipoor and B. Noheda, "Local conductivity and the role of vacancies around twin walls of (001)-BiFeO$_3$ thin films", *J. Appl. Phys.* **112**, 052003 (2012).

[17] R. E. Newnham, *Properties of materials*, Oxford University Press, New York, 2005.

[18] P. Curie and J. Curie, "Crystal physics: development of polar electricity in hemihedral crystals with inclined faces", *C. R. Acad. Sci.* **91**, 294 (1880).

[19] P. Curie and J. Curie, "Contractions et dilatations produites par des tensions électriques dans les cristaux hémièdres à faces inclines", *C. R. Acad. Sci.* **93**, 1137 (1881).

[20] F. U. T. Aepinus, "Tentamen Theoriae Electricitatis et Magnetismi." St Petersburg, 1759.

[21] J. Valasek, "Piezo-electric and allied phenomena in Rochelle salt", *Phys. Rev.* **17**, 475 (1921).

[22] R. S. Weis and T. K. Gaylord, "Lithium Niobate: Summary of Physical Properties and Crystal Structure", *Appl. Phys. A* **37**, 191 (1985).

[23] H. F. Kay, "Preparation and properties of crystals of barium titanate, BaTiO$_3$", *Acta Crystallogr.* **1**, 229 (1948).

[24] H. T. Evans, "The crystal structure of tetragonal barium titanate", *Acta Crystallogr.* **4**, 377 (1951).

[25] H. Schmid, "Multi-ferroic magnetoelectrics", *Ferroelectrics* **162**, 317 (1994).

[26] D. Pantel, S. Goetze, D. Hesse, and M. Alexe, "Reversible electrical switching of spin polarization in multiferroic tunnel junctions", *Nat. Mater.* **11**, 289 (2012).

[27] J. P. Velev, S. S. Jaswal, and E. Y. Tsymbal, "Multi-ferroic and magnetoelectric materials and interfaces", *Philos. T. Roy. Soc. A* **369**, 3069 (2011).

[28] W. Eerenstein, M. Wiora, J. L. Prieto, J. F. Scott, and N. D. Mathur, "Giant sharp and persistent converse magnetoelectric effects in multiferroic epitaxial heterostructures", *Nat. Mater.* **6**, 348 (2007).

[29] V. J. Folen, G. T. Rado, and E. W. Stalder, "Anisotropy of the magnetoelectric effect in Cr_2O_3", *Phys. Rev. Lett.* **6**, 607 (1961).

[30] R. Palai, R. S. Katiyar, H. Schmid, P. Tissot, S. J. Clark, J. Robertson, S. A. T. Redfern, G. Catalan, and J. F. Scott, "β phase and $\gamma - \beta$ metal-insulator transition in multiferroic $BiFeO_3$", *Phys. Rev. B* **77**, 014110 (2008).

[31] A. M. Glazer, "Classification of tilted octahedra in perovskites", *Acta Crystallogr. B* **28**, 3384 (1972).

[32] J. M. Moreau, C. Michel, R. Gerson, and W. J. James, "Ferroelectric $BiFeO_3$ x-ray and neutron diffraction study", *J. Phys. Chem. Solids* **32**, 1315 (1971).

[33] F. Kubel and H. Schmid, "Structure of a ferroelectric and ferroelastic monodomain crystal of the perovskite $BiFeO_3$", *Acta Crystallogr. B* **46**, 698 (1990).

[34] J. B. Neaton, C. Ederer, U. V. Waghmare, N. A. Spaldin, and K. M. Rabe, "First-principles study of spontaneous polarization in multiferroic $BiFeO_3$", *Phys. Rev. B* **71**, 014113 (2005).

[35] R. Seshadri and N. A. Hill, "Visualizing the role of Bi 6s lone pairs in the off-center distortion in ferromagnetic $BiMnO_3$", *Chem. Mater.* **13**, 2892 (2001).

[36] J. Wang, J. B. Neaton, H. Zheng, V. Nagarajan, S. B. Ogale, B. Liu, D. Viehland, V. Vaithyanathan, D. G. Schlom, U. V. Waghmare, N. A. Spaldin, K. M. Rabe, M. Wuttig, and R. Ramesh, "Epitaxial $BiFeO_3$ multiferroic thin film heterostructures", *Science* **299**, 1719 (2003).

[37] D. Lebeugle, D. Colson, A. Forget, and M. Viret, "Very large spontaneous electric polarization in $BiFeO_3$ single crystals at room temperature and its evolution under cycling fields", *Appl. Phys. Lett.* **91**, 022907 (2007).

[38] V. V. Shvartsman, W. Kleemann, R. Haumont, and J. Kreisel, "Large bulk polarization and regular domain structure in ceramic $BiFeO_3$", *Appl. Phys. Lett.* **90**, 172115 (2007).

[39] K. J. Choi, M. Biegalski, Y. L. Li, A. Sharan, J. Schubert, R. Uecker, P. Reiche, Y. B. Chen, X. Q. Pan, V. Gopalan, L. Q. Chen, D. G. Schlom, and C. B. Eom, "Enhancement of ferroelectricity in strained $BaTiO_3$ thin films", *Science* **306**, 1005 (2004).

[40] D. H. Kim, H. N. Lee, M. D. Biegalski, and H. M. Christen, "Effect of epitaxial strain on ferroelectric polarization in multiferroic $BiFeO_3$ films", *Appl. Phys. Lett.* **92**, 012911 (2008).

[41] H. W. Jang, S. H. Baek, D. Ortiz, C. M. Folkman, R. R. Das, Y. H. Chu, P. Shafer, J. X. Zhang, S. Choudhury, V. Vaithyanathan, Y. B. Chen, D. A. Felker, M. D. Biegalski, M. S. Rzchowski, X. Q. Pan, D. G. Schlom, L. Q. Chen, R. Ramesh, and

C. B. Eom, "Strain-induced polarization rotation in epitaxial (001) BiFeO$_3$ thin films", *Phys. Rev. Lett.* **101**, 107602 (2008).

[42] M. D. Biegalski, D. H. Kim, S. Choudhury, L. Q. Chen, H. M. Christen, and K. Dörr, "Strong strain dependence of ferroelectric coercivity in a BiFeO$_3$ film", *Appl. Phys. Lett.* **98**, 142902 (2011).

[43] C. Ederer and N. A. Spaldin, "Effect of epitaxial strain on the spontaneous polarization of thin film ferroelectrics", *Phys. Rev. Lett.* **95**, 257601 (2005).

[44] P. Fischer, M. Polomska, I. Sosnowska, and M. Szymanski, "Temperature dependence of the crystal and magnetic structures of BiFeO$_3$", *J. Phys. C Solid State* **13**, 1931 (1980).

[45] H. Toupet, F. Le Marrec, C. Lichtensteiger, B. Dkhil, and M. G. Karkut, "Evidence for a first-order transition from monoclinic α to monoclinic β phase in BiFeO$_3$ thin films", *Phys. Rev. B* **81**, 140101 (2010).

[46] A. Kadomtseva, A. Zvezdin, Y. Popov, A. Pyatakov, and G. Vorobev, "Space-time parity violation and magnetoelectric interactions in antiferromagnets", *JETP Lett.* **79**, 571 (2004).

[47] D. Lebeugle, D. Colson, A. Forget, M. Viret, A. M. Bataille, and A. Gukasov, "Electric-field-induced spin flop in BiFeO$_3$ single crystals at room temperature", *Phys. Rev. Lett.* **100**, 227602 (2008).

[48] F. Zavaliche, P. Shafer, R. Ramesh, M. P. Cruz, R. R. Das, D. M. Kim, and C. B. Eom, "Polarization switching in epitaxial BiFeO$_3$ films", *Appl. Phys. Lett.* **87**, 252902 (2005).

[49] Y.-H. Chu, L. W. Martin, M. B. Holcomb, M. Gajek, S.-J. Han, Q. He, N. Balke, C.-H. Yang, D. Lee, W. Hu, Q. Zhan, P.-L. Yang, A. Fraile-Rodriguez, A. Scholl, S. X. Wang, and R. Ramesh, "Electric-field control of local ferromagnetism using a magnetoelectric multiferroic", *Nat. Mater.* **7**, 478 (2008).

[50] S. K. Streiffer, C. B. Parker, A. E. Romanov, M. J. Lefevre, L. Zhao, J. S. Speck, W. Pompe, C. M. Foster, and G. R. Bai, "Domain patterns in epitaxial rhombohedral ferroelectric films. I. geometry and experiments", *J. Appl. Phys.* **83**, 2742 (1998).

[51] A. Okazaki and M. Kawamina, "Lattice-constant of strontium-titanate at low-temperatures", *Mater. Res. Bull.* **8**, 545 (1973).

[52] S. Geller, "Crystal structure of gadolinium orthoferrite, GdFeO$_3$", *J. Chem. Phys.* **24**, 1236 (1956).

[53] R. Uecker, B. Velickov, D. Klimm, R. Bertram, M. Bernhagen, M. Rabe, M. Albrecht, R. Fornari, and D. G. Schlom, "Properties of rare-earth scandate single crystals (Re = Nd-Dy)", *J. Cryst. Growth* **310**, 2649 (2008).

[54] F. C. Frank and J. H. v. d. Merwe, "One-dimensional dislocations. ii. misfitting monolayers and oriented overgrowth", *Proc. R. Soc. Lond. Ser. A* **198**, 216 (1949).

[55] R. J. Bouchard and J. L. Gillson, "Electrical properties of $CaRuO_3$ and $SrRuO_3$ singlecrystals", *Mater. Res. Bull.* **7**, 873 (1972).

[56] A. Callagha, C. W. Moeller, and R. Ward, "Magnetic interactions in ternary ruthenium oxides", *Inorg. Chem.* **5**, 1572 (1966).

[57] C. W. Jones, P. D. Battle, P. Lightfoot, and W. T. A. Harrison, "The structure of $SrRuO_3$ by time-of-flight neutron powder diffraction", *Acta Crystallogr. C* **45**, 365 (1989).

[58] A. Vailionis, H. Boschker, W. Siemons, E. P. Houwman, D. H. A. Blank, G. Rijnders, and G. Koster, "Misfit strain accommodation in epitaxial ABO_3 perovskites: Lattice rotations and lattice modulations", *Phys. Rev. B* **83**, 064101 (2011).

[59] A. Vailionis, W. Siemons, and G. Koster, "Room temperature epitaxial stabilization of a tetragonal phase in $ARuO_3$ (A = Ca and Sr) thin films", *Appl. Phys. Lett.* **93**, 051909 (2008).

[60] P. G. Radaelli, G. Iannone, M. Marezio, H. Y. Hwang, S.-W. Cheong, J. D. Jorgensen, and D. N. Argyriou, "Structural effects on the magnetic and transport properties of perovskite $A_{1-x}A'_x MnO_3$ (x = 0.25, 0.30)", *Phys. Rev. B* **56**, 8265 (1997).

[61] H. Watanabe, "Magnetic properties of perovskites containing strontium, II. lanthanum-strontium manganites.", *J. Phys. Soc. Jpn.* **16**, 433 (1961).

[62] G. H. Jonker and J. H. Vansanten, "Ferromagnetic compounds of manganese with perovskite structure", *Physica* **16**, 337 (1950).

[63] H. Y. Hwang, S.-W. Cheong, N. P. Ong, and B. Batlogg, "Spin-polarized intergrain tunneling in $La_{2/3}Sr_{1/3}MnO_3$", *Phys. Rev. Lett.* **77**, 2041 (1996).

[64] A. Urushibara, Y. Moritomo, T. Arima, A. Asamitsu, G. Kido, and Y. Tokura, "Insulator-metal transition and giant magnetoresistance in $La_{1-x}Sr_xMnO_3$", *Phys. Rev. B* **51**, 14103 (1995).

[65] H. Boschker, M. Huijben, A. Vailionis, J. Verbeeck, S. van Aert, M. Luysberg, S. Bals, G. van Tendeloo, E. P. Houwman, G. Koster, D. H. A. Blank, and G. Rijnders, "Optimized fabrication of high-quality $La_{0.67}Sr_{0.33}MnO_3$ thin films considering all essential characteristics", *J. Phys. D: Appl. Phys.* **44**, 205001 (2011).

[66] D. B. Chrisey and G. K. Hubler, eds., *Pulsed laser deposition of thin films*, J. Wiley, New York, 1994.

[67] R. Eason, ed., *Pulsed laser deposition of thin films: applications-led growth of functional materials*, Wiley-Interscience, Hoboken, 2007.

[68] G. Rijnders and D. H. A. Blank, "Materials science: Build your own superlattice", *Nature* **433**, 369 (2005).

[69] L. Martin, Y.-H. Chu, and R. Ramesh, "Advances in the growth and characterization of magnetic, ferroelectric, and multiferroic oxide thin films", *Mater. Sci. Eng. R* **68**, 89 (2010).

[70] Y. S. Jeong, S. Y. Lee, H. K. Jang, I.-S. Yang, S.-H. Moon, and B. Oh, "Surface modification of laser ablated YBCO target", *Appl. Surf. Sci.* **109-110**, 424 (1997).

[71] D. B. Geohegan, "Fast intensified-CCD photography of $YBa_2Cu_3O_{7-x}$ laser ablation in vacuum and ambient oxygen", *Appl. Phys. Lett.* **60**, 2732 (1992).

[72] G. Binnig, C. F. Quate, and C. Gerber, "Atomic force microscope", *Phys. Rev. Lett.* **56**, 930 (1986).

[73] G. Binnig, C. Gerber, E. Stoll, T. R. Albrecht, and C. F. Quate, "Atomic resolution with atomic force microscope", *Europhys. Lett.* **3**, 1281 (1987).

[74] Y. Martin, D. W. Abraham, and H. K. Wickramasinghe, "High-resolution capacitance measurement and potentiometry by force microscopy", *Appl. Phys. Lett.* **52**, 1103 (1988).

[75] P. Maivald, H. Butt, S. Gould, C. Prater, B. Drake, J. Gurley, V. Elings, and P. Hansma, "Using force modulation to image surface elasticities with the atomic force microscope", *Nanotechnology* **2**, 103 (1991).

[76] G. Leatherman, E. N. Durantini, D. Gust, T. A. Moore, A. L. Moore, S. Stone, Z. Zhou, P. Rez, Y. Z. Liu, and S. M. Lindsay, "Carotene as a molecular wire: Conducting atomic force microscopy", *J. Phys. Chem. B* **103**, 4006 (1999).

[77] J. J. Saenz, N. Garcia, P. Grutter, E. Meyer, H. Heinzelmann, R. Wiesendanger, L. Rosenthaler, H. R. Hidber, and H.-J. Güntherodt, "Observation of magnetic forces by the atomic force microscope", *J. Appl. Phys.* **62**, 4293 (1987).

[78] E. Soergel, "Piezoresponse force microscopy (PFM)", *J. Phys. D: Appl. Phys.* **44**, 464003 (2011).

[79] T. Jungk, Á. Hoffmann, M. Fiebig, and E. Soergel, "Electrostatic topology of ferroelectric domains in $YMnO_3$", *Appl. Phys. Lett.* **97**, 012904 (2010).

[80] T. Jungk, Á. Hoffmann, and E. Soergel, "Impact of the tip radius on the lateral resolution in piezoresponse force microscopy", *New J. Phys.* **10**, 013019 (2008).

[81] T. Jungk, Á. Hoffmann, and E. Soergel, "Influence of the inhomogeneous field at the tip on quantitative piezoresponse force microscopy", *Appl. Phys. A - Mater.* **86**, 353 (2007).

[82] T. Jungk, Á. Hoffmann, and E. Soergel, "Contrast mechanisms for the detection of ferroelectric domains with scanning force microscopy", *New J. Phys.* **11**, 033029 (2009).

[83] F. Zavaliche, R. R. Das, D. M. Kim, C. B. Eom, S. Y. Yang, P. Shafer, and R. Ramesh, "Ferroelectric domain structure in epitaxial $BiFeO_3$ films", *Appl. Phys. Lett.* **87**, 182912 (2005).

[84] F. Zavaliche, S. Y. Yang, T. Zhao, Y. H. Chu, M. P. Cruz, C. B. Eom, and R. Ramesh, "Multiferroic $BiFeO_3$ films: domain structure and polarization dynamics", *Phase Transit.* **79**, 991 (2006).

[85] J. B. Nelson and D. P. Riley, "An experimental investigation of extrapolation methods in the derivation of accurate unit-cell dimensions of crystals", *Proc. R. Soc. Lond.* **57**, 160 (1945).

[86] D. B. Williams and C. B. Carter, *Transmission Electron Microscopy*, Springer, New York, 1996.

[87] L. Reimer and G. Pfefferkorn, *Raster-Elektronenmikroskopie*, Springer, Berlin, 1977.

[88] H. W. Jang, D. Ortiz, S. H. Baek, C. M. Folkman, R. R. Das, P. Shafer, Y. Chen, C. T. Nelson, X. Pan, R. Ramesh, and C. B. Eom, "Domain engineering for enhanced ferroelectric properties of epitaxial (001) $BiFeO_3$ thin films", *Adv. Mater.* **21**, 817 (2009).

[89] P. Yu, W. Luo, D. Yi, J. X. Zhang, M. D. Rossell, C.-H. Yang, L. You, G. Singh-Bhalla, S. Y. Yang, Q. He, Q. M. Ramasse, R. Erni, L. W. Martin, Y. H. Chu, S. T. Pantelides, S. J. Pennycook, and R. Ramesh, "Interface control of bulk ferroelectric polarization", *P. Natl. Acad. Sci. USA* **109**, 9710 (2012).

[90] Y. H. Chu, Q. He, C. H. Yang, P. Yu, L. W. Martin, P. Shafer, and R. Ramesh, "Nanoscale control of domain architectures in $BiFeO_3$ thin films", *Nano Lett.* **9**, 1726 (2009).

[91] C. M. Folkman, S. H. Baek, H. W. Jang, C. B. Eom, C. T. Nelson, X. Q. Pan, Y. L. Li, L. Q. Chen, A. Kumar, V. Gopalan, and S. K. Streiffer, "Stripe domain structure in epitaxial (001) $BiFeO_3$ thin films on orthorhombic $TbScO_3$ substrate", *Appl. Phys. Lett.* **94**, 251911 (2009).

[92] Y.-H. Chu, Q. Zhan, L. Martin, M. Cruz, P.-L. Yang, G. Pabst, F. Zavaliche, S.-Y. Yang, J.-X. Zhang, L.-Q. Chen, D. Schlom, I.-N. Lin, T.-B. Wu, and R. Ramesh, "Nanoscale domain control in multiferroic $BiFeO_3$ thin films", *Adv. Mater.* **18**, 2307 (2006).

[93] F. Johann, A. Morelli, D. Biggemann, M. Arredondo, and I. Vrejoiu, "Epitaxial strain and electric boundary condition effects on the structural and ferroelectric properties of $BiFeO_3$ films", *Phys. Rev. B* **84**, 094105 (2011).

[94] F. Johann, A. Morelli, and I. Vrejoiu, "Stability of 71° stripe domains in epitaxial $BiFeO_3$ films upon repeated electrical switching", *Phys. Status Solidi B* DOI: 10.1002/pssb.201248329 (2012).

[95] M. Kawasaki, K. Takahashi, T. Maeda, R. Tsuchiya, M. Shinohara, O. Ishiyama, T. Yonezawa, M. Yoshimoto, and H. Koinuma, "Atomic control of the $SrTiO_3$ crystal surface", *Science* **266**, 1540 (1994).

[96] G. Koster, B. L. Kropman, G. J. H. M. Rijnders, D. H. A. Blank, and H. Rogalla, "Quasi-ideal strontium titanate crystal surfaces through formation of strontium hydroxide", *Appl. Phys. Lett.* **73**, 2920 (1998).

[97] J. E. Kleibeuker, G. Koster, W. Siemons, D. Dubbink, B. Kuiper, J. L. Blok, C.-H. Yang, J. Ravichandran, R. Ramesh, J. E. ten Elshof, D. H. A. Blank, and G. Rijnders, "Atomically defined rare-earth scandate crystal surfaces", *Adv. Funct. Mater.* **20**, 3490 (2010).

[98] R. Dirsyte, J. Schwarzkopf, G. Wagner, R. Fornari, J. Lienemann, M. Busch, and H. Winter, "Thermal-induced change in surface termination of $DyScO_3(110)$", *Surf. Sci.* **604**, L55 (2010).

[99] I. C. Infante, S. Lisenkov, B. Dupé, M. Bibes, S. Fusil, E. Jacquet, G. Geneste, S. Petit, A. Courtial, J. Juraszek, L. Bellaiche, A. Barthélémy, and B. Dkhil, "Bridging multiferroic phase transitions by epitaxial strain in $BiFeO_3$", *Phys. Rev. Lett.* **105**, 057601 (2010).

[100] N. Nakagawa, H. Y. Hwang, and D. A. Muller, "Why some interfaces cannot be sharp", *Nat. Mater.* **5**, 204 (2006).

[101] C. W. Huang, Z. H. Chen, J. Wang, T. Sritharan, and L. Chen, "Stability and crossover of 71° and 109° domains influenced by the film thickness and depolarization field in rhombohedral ferroelectric thin films", *J. Appl. Phys.* **110**, 014110 (2011).

[102] J. M. Rondinelli, S. J. May, and J. W. Freeland, "Control of octahedral connectivity in perovskite oxide heterostructures: An emerging route to multifunctional materials discovery", *MRS Bulletin* **37**, 261 (2012).

[103] J. M. Rondinelli and C. J. Fennie, "Octahedral rotation-induced ferroelectricity in cation ordered perovskites", *Adv. Mater.* **24**, 1961 (2012).

[104] C. W. Huang, L. Chen, J. Wang, Q. He, S. Y. Yang, Y. H. Chu, and R. Ramesh, "Phenomenological analysis of domain width in rhombohedral $BiFeO_3$ films", *Phys. Rev. B* **80**, 140101 (2009).

[105] P. Maksymovych, S. Jesse, P. Yu, R. Ramesh, A. P. Baddorf, and S. V. Kalinin, "Polarization control of electron tunneling into ferroelectric surfaces", *Science* **324**, 1421 (2009).

[106] J. E. Kleibeuker, B. Kuiper, S. Harkema, D. H. A. Blank, G. Koster, G. Rijnders, P. Tinnemans, E. Vlieg, P. B. Rossen, W. Siemons, G. Portale, J. Ravichandran, J. M. Szepieniec, and R. Ramesh, "Structure of singly terminated polar $DyScO_3$ (110) surfaces", *Phys. Rev. B* **85**, 165413 (2012).

[107] W. Hong, H. N. Lee, M. Yoon, H. M. Christen, D. H. Lowndes, Z. Suo, and Z. Zhang, "Persistent step-flow growth of strained films on vicinal substrates", *Phys. Rev. Lett.* **95**, 095501 (2005).

[108] G. Rijnders, D. H. A. Blank, J. Choi, and C.-B. Eom, "Enhanced surface diffusion through termination conversion during epitaxial $SrRuO_3$ growth", *Appl. Phys. Lett.* **84**, 505 (2004).

VIII

[109] Q. Gan, R. A. Rao, and C. B. Eom, "Control of the growth and domain structure of epitaxial $SrRuO_3$ thin films by vicinal (001) $SrTiO_3$ substrates", *Appl. Phys. Lett.* **70**, 1962 (1997).

[110] J. W. Park, S. H. Baek, P. Wu, B. Winchester, C. T. Nelson, X. Q. Pan, L. Q. Chen, T. Tybell, and C. B. Eom, "Origin of suppressed polarization in $BiFeO_3$ films", *Appl. Phys. Lett.* **97**, 212904 (2010).

[111] Y.-H. Chu, T. Zhao, M. P. Cruz, Q. Zhan, P. L. Yang, L. W. Martin, M. Huijben, C. H. Yang, F. Zavaliche, H. Zheng, and R. Ramesh, "Ferroelectric size effects in multiferroic $BiFeO_3$ thin films", *Appl. Phys. Lett.* **90**, 252906 (2007).

[112] X. Zou, L. You, W. Chen, H. Ding, D. Wu, T. Wu, L. Chen, and J. Wang, "Mechanism of polarization fatigue in $BiFeO_3$", *ACS Nano* DOI: 10.1021/nn303090k (2012).

[113] S. H. Baek, H. W. Jang, C. M. Folkman, Y. L. Li, B. Winchester, J. X. Zhang, Q. He, Y. H. Chu, C. T. Nelson, M. S. Rzchowski, X. Q. Pan, R. Ramesh, L. Q. Chen, and C. B. Eom, "Ferroelastic switching for nanoscale non-volatile magneto-electric devices", *Nat. Mater.* **9**, 309 (2010).

[114] S.-H. Baek, C. M. Folkman, J.-W. Park, S. Lee, C.-W. Bark, T. Tybell, and C. B. Eom, "The nature of polarization fatigue in $BiFeO_3$", *Adv. Mater.* **23**, 1621 (2011).

[115] N. Balke, M. Gajek, A. K. Tagantsev, L. W. Martin, Y.-H. Chu, R. Ramesh, and S. V. Kalinin, "Direct observation of capacitor switching using planar electrodes", *Adv. Funct. Mater.* **20**, 3466 (2010).

[116] N. Balke, S. Choudhury, S. Jesse, M. Huijben, Y. H. Chu, A. P. Baddorf, L. Q. Chen, R. Ramesh, and S. V. Kalinin, "Deterministic control of ferroelastic switching in multiferroic materials", *Nat. Nanotechnol.* **4**, 868 (2009).

[117] P. Shafer, F. Zavaliche, Y. H. Chu, P. L. Yang, M. P. Cruz, and R. Ramesh, "Planar electrode piezoelectric force microscopy to study electric polarization switching in $BiFeO_3$", *Appl. Phys. Lett.* **90**, 202909 (2007).

[118] L. You, E. Liang, R. Guo, D. Wu, K. Yao, L. Chen, and J. Wang, "Polarization switching in quasiplanar $BiFeO_3$ capacitors", *Appl. Phys. Lett.* **97**, 062910 (2010).

[119] C. M. Folkman, S. H. Baek, C. T. Nelson, H. W. Jang, T. Tybell, X. Q. Pan, and C. B. Eom, "Study of defect-dipoles in an epitaxial ferroelectric thin film", *Appl. Phys. Lett.* **96**, 052903 (2010).

[120] T. Jungk, A. Hoffmann, and E. Soergel, "Impact of elasticity on the piezoresponse of adjacent ferroelectric domains investigated by scanning force microscopy", *J. Appl. Phys.* **102**, 084102 (2007).

[121] E. Colla, I. Stolichnov, P. Bradely, and N. Setter, "Direct observation of inversely polarized frozen nanodomains in fatigued ferroelectric memory capacitors", *Appl. Phys. Lett.* **82**, 1604 (2003).

[122] J. S. Liu, S. R. Zhang, L. S. Dai, and Y. Yuan, "Domain evolution in ferroelectric thin films during fatigue process", *J. Appl. Phys.* **97**, 104102 (2005).

[123] G. W. Pabst, L. W. Martin, Y.-H. Chu, and R. Ramesh, "Leakage mechanisms in BiFeO$_3$ thin films", *Appl. Phys. Lett.* **90**, 072902 (2007).

[124] L. Pintilie, I. Vrejoiu, D. Hesse, G. LeRhun, and M. Alexe, "Ferroelectric polarization-leakage current relation in high quality epitaxial Pb(Zr,Ti)O$_3$ films", *Phys. Rev. B* **75**, 104103 (2007).

[125] V. Y. Shur, A. I. Lobov, A. G. Shur, S. Kurimura, Y. Nomura, K. Terabe, X. Y. Liu, and K. Kitamura, "Rearrangement of ferroelectric domain structure induced by chemical etching", *Appl. Phys. Lett.* **87**, 022905 (2005).

[126] Y. Kim, I. Vrejoiu, D. Hesse, and M. Alexe, "Reversible plasma switching in epitaxial BiFeO$_3$ thin films", *Appl. Phys. Lett.* **96**, 202902 (2010).

[127] D. D. Fong, A. M. Kolpak, J. A. Eastman, S. K. Streiffer, P. H. Fuoss, G. B. Stephenson, C. Thompson, D. M. Kim, K. J. Choi, C. B. Eom, I. Grinberg, and A. M. Rappe, "Stabilization of monodomain polarization in ultrathin PbTiO$_3$ films", *Phys. Rev. Lett.* **96**, 127601 (2006).

[128] A. Gruverman, B. J. Rodriguez, C. Dehoff, J. D. Waldrep, A. I. Kingon, R. J. Nemanich, and J. S. Cross, "Direct studies of domain switching dynamics in thin film ferroelectric capacitors", *Appl. Phys. Lett.* **87**, 082902 (2005).

[129] Y. Kim, H. Han, W. Lee, S. Baik, D. Hesse, and M. Alexe, "Non-Kolmogorov-Avrami-Ishibashi switching dynamics in nanoscale ferroelectric capacitors", *Nano Lett.* **10**, 1266 (2010).

[130] Y. Kim, A. Kumar, O. Ovchinnikov, S. Jesse, H. Han, D. Pantel, I. Vrejoiu, W. Lee, D. Hesse, M. Alexe, and S. V. Kalinin, "First-order reversal curve probing of spatially resolved polarization switching dynamics in ferroelectric nanocapacitors", *ACS Nano* **6**, 491 (2011).

[131] J. Allibe, S. Fusil, K. Bouzehouane, C. Daumont, D. Sando, E. Jacquet, C. Deranlot, M. Bibes, and A. Barthélémy, "Room temperature electrical manipulation of giant magnetoresistance in spin valves exchange-biased with BiFeO$_3$", *Nano Lett.* **12**, 1141 (2012).

[132] A. Gruverman and M. Tanaka, "Polarization retention in SrBi$_2$Ta$_2$O$_9$ thin films investigated at nanoscale", *J. Appl. Phys.* **89**, 1836 (2001).

[133] A. Hoffmann, T. Jungk, and E. Soergel, "Cross-talk correction in atomic force microscopy", *Rev. Sci. Instrum.* **78**, 016101 (2007).

[134] C. T. Nelson, P. Gao, J. R. Jokisaari, C. Heikes, C. Adamo, A. Melville, S.-H. Baek, C. M. Folkman, B. Winchester, Y. Gu, Y. Liu, K. Zhang, E. Wang, J. Li, L.-Q. Chen, C.-B. Eom, D. G. Schlom, and X. Pan, "Domain dynamics during ferroelectric switching", *Science* **334**, 968 (2011).

[135] Y. Ishibashi and Y. Takagi, "Note on ferroelectric domain switching", *J. Phys. Soc. Jpn.* **31**, 506 (1971).

[136] Y. Ishibashi, "Theory of polarization reversals in ferroelectrics based on Landau-type free energy", *Jpn. J. Appl. Phys.* **31**, 2822 (1992).

[137] M. Iwanowska, I. Stolichnov, E. Colla, A. Tagantsev, P. Muralt, and N. Setter, "Polarization reversal in $BiFeO_3$ capacitors: Complex behavior revealed by PFM", *Ferroelectrics* **421**, 54 (2011).

[138] G. Gerra, A. K. Tagantsev, and N. Setter, "Surface-stimulated nucleation of reverse domains in ferroelectrics", *Phys. Rev. Lett.* **94**, 107602 (2005).

[139] W. J. Merz, "Domain formation and domain wall motions in ferroelectric $BaTiO_3$ single crystals", *Phys. Rev.* **95**, 690 (1954).

[140] R. Landauer, "Electrostatic considerations in $BaTiO_3$ domain formation during polarization reversal", *J. Appl. Phys.* **28**, 227 (1957).

[141] P. Chandra, M. Dawber, P. B. Littlewood, and J. F. Scott, "Scaling of the coercive field with thickness in thin-film ferroelectrics", *Ferroelectrics* **313**, 7 (2004).

[142] R. Merkle and J. Maier, "How is oxygen incorporated into oxides? A comprehensive kinetic study of a simple solid-state reaction with $SrTiO_3$ as a model material", *Angew. Chem. Int. Edit.* **47**, 3874 (2008).

[143] G. Pacchioni, "Oxygen vacancy: The invisible agent on oxide surfaces", *ChemPhysChem* **4**, 1041 (2003).

[144] W.-M. Lee, J. H. Sung, K. Chu, X. Moya, D. Lee, C.-J. Kim, N. D. Mathur, S.-W. Cheong, C.-H. Yang, and M.-H. Jo, "Spatially resolved photodetection in leaky ferroelectric $BiFeO_3$", *Adv. Mater.* **24**, OP49 (2012).

[145] F. Johann, T. Jungk, M. Lilienblum, A. Hoffmann, and E. Soergel, "Lateral signals in piezoresponse force microscopy at domain boundaries of ferroelectric crystals", *Appl. Phys. Lett.* **97**, 102902 (2010).

[146] J. D. Bucci, B. K. Robertson, and W. J. James, "The precision determination of the lattice parameters and the coefficients of thermal expansion of $BiFeO_3$", *J. Appl. Crystallogr.* **5**, 187 (1972).

[147] A. K. Tagantsev, I. Stolichnov, E. L. Colla, and N. Setter, "Polarization fatigue in ferroelectric films: Basic experimental findings, phenomenological scenarios, and microscopic features", *J. Appl. Phys.* **90**, 1387 (2001).

[148] X. J. Lou, "Polarization fatigue in ferroelectric thin films and related materials", *J. Appl. Phys.* **105**, 024101 (2009).

[149] J. A. Hooton and W. J. Merz, "Etch patterns and ferroelectric domains in $BaTiO_3$ single crystals", *Phys. Rev.* **98**, 409 (1955).

[150] N. Niizeki, T. Yamada, and H. Toyoda, "Growth ridges etched hillocks and crystal structure of lithium niobate", *Jpn. J. Appl. Phys.* **6**, 318 (1967).

[151] K. Nassau, H. J. Levinste, and G. M. Loiacono, "Ferroelectric lithium niobate. 1. growth, domain structure, dislocations, and etching", *J. Phys. Chem. Solids* **27**, 983 (1966).

[152] E. Soergel, "Visualization of ferroelectric domains in bulk single crystals", *Appl. Phys. B-Lasers O.* **81**, 729 (2005).

[153] I. E. Barry, G. W. Ross, P. G. R. Smith, R. W. Eason, and G. Cook, "Microstructuring of lithium niobate using differential etch-rate between inverted and non-inverted ferroelectric domains", *Mater. Lett.* **37**, 246 (1998).

[154] C. Sones, S. Mailis, V. Apostolopoulos, I. E. Barry, C. Gawith, P. G. R. Smith, and R. W. Eason, "Fabrication of piezoelectric micro-cantilevers in domain-engineered $LiNbO_3$ single crystals", *J. Micromech. Microeng.* **12**, 53 (2002).

[155] C. Y. J. Ying, C. L. Sones, A. C. Peacock, F. Johann, E. Soergel, R. W. Eason, M. N. Zervas, and S. Mailis, "Ultra-smooth lithium niobate photonic microstructures by surface tension reshaping", *Opt. Express* **18**, 11508 (2010).

[156] C. L. Sones, S. Mailis, W. S. Brocklesby, R. W. Eason, and J. R. Owen, "Differential etch rates in z-cut $LiNbO_3$ for variable HF/HNO_3 concentrations", *J. Mater. Chem.* **12**, 295 (2002).

[157] F. Kubel and H. Schmid, "Growth, twinning and etch figures of ferroelectric ferroelastic dendritic $BiFeO_3$ single domain crystals", *J. Cryst. Growth* **129**, 515 (1993).

[158] S. Hong, J. A. Klug, M. Park, A. Imre, M. J. Bedzyk, K. No, A. Petford-Long, and O. Auciello, "Nanoscale piezoresponse studies of ferroelectric domains in epitaxial $BiFeO_3$ nanostructures", *J. Appl. Phys.* **105**, 061619 (2009).

[159] A. Morelli, F. Johann, N. Schammelt, and I. Vrejoiu, "Ferroelectric nanostructures fabricated by focused-ion-beam milling in epitaxial $BiFeO_3$ thin films", *Nanotechnology* **22**, 265303 (2011).

[160] F. Johann, A. Morelli, and I. Vrejoiu, "Epitaxial $BiFeO_3$ nanostructures fabricated by differential etching of $BiFeO_3$ films", *Appl. Phys. Lett.* **99**, 082904 (2011).

[161] R. V. Wang, D. D. Fong, F. Jiang, M. J. Highland, P. H. Fuoss, C. Thompson, A. M. Kolpak, J. A. Eastman, S. K. Streiffer, A. M. Rappe, and G. B. Stephenson, "Reversible chemical switching of a ferroelectric film", *Phys. Rev. Lett.* **102**, 047601 (2009).

[162] D. M. Knotter, "Etching mechanism of vitreous silicon dioxide in HF-based solutions", *J. Am. Chem. Soc.* **122**, 4345 (2000).

[163] D. Conklin, T.-H. Park, S. Nanayakkara, M. J. Therien, and D. A. Bonnell, "Controlling polarization dependent reactions to fabricate multi-component functional nanostructures", *Adv. Funct. Mater.* **21**, 4598 (2011).

[164] N. V. Burbure, P. A. Salvador, and G. S. Rohrer, "Influence of dipolar fields on the photochemical reactivity of thin titania films on $BaTiO_3$ substrates", *J. Am. Ceram. Soc.* **89**, 2943 (2006).

[165] P. M. Jones and S. Dunn, "Photo-reduction of silver salts on highly heterogeneous lead zirconate titanate", *Nanotechnology* **18**, 185702 (2007).

[166] W.-C. Yang, B. J. Rodriguez, A. Gruverman, and R. J. Nemanich, "Polarization-dependent electron affinity of LiNbO$_3$ surfaces", *Appl. Phys. Lett.* **85**, 2316 (2004).

[167] S. V. Kalinin, D. A. Bonnell, T. Alvarez, X. Lei, Z. Hu, J. H. Ferris, Q. Zhang, and S. Dunn, "Atomic polarization and local reactivity on ferroelectric surfaces: A new route toward complex nanostructures", *Nano Lett.* **2**, 589 (2002).

[168] M. H. Zhao, D. A. Bonnell, and J. M. Vohs, "Effect of ferroelectric polarization on the adsorption and reaction of ethanol on BaTiO$_3$", *Surf. Sci.* **602**, 2849 (2008).

[169] M. X. Tan, P. E. Laibinis, S. T. Nguyen, J. M. Kesselman, C. E. Stanton, and N. S. Lewis, "Principles and applications of semiconductor photoelectrochemistry", *Prog. Inorg. Chem.* **41**, 21 (1994).

[170] S. R. Basu, L. W. Martin, Y. H. Chu, M. Gajek, R. Ramesh, R. C. Rai, X. Xu, and J. L. Musfeldt, "Photoconductivity in BiFeO$_3$ thin films", *Appl. Phys. Lett.* **92**, 091905 (2008).

[171] S. J. Clark and J. Robertson, "Band gap and Schottky barrier heights of multiferroic BiFeO$_3$", *Appl. Phys. Lett.* **90**, 132903 (2007).

[172] M. Lax, "Temperature rise induced by a laser beam", *J. Appl. Phys.* **48**, 3919 (1977).

[173] D.-W. Oh, J. Ravichandran, C.-W. Liang, W. Siemons, B. Jalan, C. M. Brooks, M. Huijben, D. G. Schlom, S. Stemmer, L. W. Martin, A. Majumdar, R. Ramesh, and D. G. Cahill, "Thermal conductivity as a metric for the crystalline quality of SrTiO$_3$ epitaxial layers", *Appl. Phys. Lett.* **98**, 221904 (2011).

[174] S. Yamanaka, T. Maekawa, H. Muta, T. Matsuda, S. Kobayashi, and K. Kurosaki, "Thermophysical properties of SrHfO$_3$ and SrRuO$_3$", *J. Solid State Chem.* **177**, 3484 (2004).

[175] J. Seidel, D. Fu, S.-Y. Yang, E. Alarcón-Lladó, J. Wu, R. Ramesh, and J. W. Ager III., "Efficient photovoltaic current generation at ferroelectric domain walls", *Phys. Rev. Lett.* **107**, 126805 (2011).

[176] S. J. Clark and J. Robertson, "Energy levels of oxygen vacancies in BiFeO$_3$ by screened exchange", *Appl. Phys. Lett.* **94**, 022902 (2009).

[177] A. Lubk, S. Gemming, and N. A. Spaldin, "First-principles study of ferroelectric domain walls in multiferroic bismuth ferrite", *Phys. Rev. B* **80**, 104110 (2009).

[178] Y.-P. Chiu, Y.-T. Chen, B.-C. Huang, M.-C. Shih, J.-C. Yang, Q. He, C.-W. Liang, J. Seidel, Y.-C. Chen, R. Ramesh, and Y.-H. Chu, "Atomic-scale evolution of local electronic structure across multiferroic domain walls", *Adv. Mater.* **23**, 1530 (2011).

[179] S. Bühlmann, B. Dwir, J. Baborowski, and P. Muralt, "Size effect in mesoscopic epitaxial ferroelectric structures: Increase of piezoelectric response with decreasing feature size", *Appl. Phys. Lett.* **80**, 3195 (2002).

[180] V. Nagarajan, A. Stanishevsky, L. Chen, T. Zhao, B.-T. Liu, J. Melngailis, A. L. Roytburd, R. Ramesh, J. Finder, Z. Yu, R. Droopad, and K. Eisenbeiser, "Realizing intrinsic piezoresponse in epitaxial submicron lead zirconate titanate capacitors on Si", *Appl. Phys. Lett.* **81**, 4215 (2002).

[181] V. Nagarajan, A. Roytburd, A. Stanishevsky, S. Prasertchoung, T. Zhao, L. Chen, J. Melngailis, O. Auciello, and R. Ramesh, "Dynamics of ferroelastic domains in ferroelectric thin films", *Nat. Mater.* **2**, 43 (2003).

[182] V. Nagarajan, "Scaling of the piezoelectric response in ferroelectric nanostructures: An effective clamping stress model", *Appl. Phys. Lett.* **87**, 242905 (2005).

[183] C.-V. Cojocaru, R. Nechache, C. Harnagea, A. Pignolet, and F. Rosei, "Nanoscale patterning of functional perovskite-type complex oxides by pulsed laser deposition through a nanostencil", *Appl. Surf. Sci.* **256**, 4777 (2010).

[184] P. te Riele, *Direct patterning of oxides by pulsed laser stencil deposition.* PhD thesis, Universiteit Twente, 2008.

[185] C. J. M. Daumont, S. Farokhipoor, A. Ferri, J. C. Wojdeł, J. Íñiguez, B. J. Kooi, and B. Noheda, "Tuning the atomic and domain structure of epitaxial films of multiferroic BiFeO$_3$", *Phys. Rev. B* **81**, 144115 (2010).

Acknowledgments

Ich möchte mich herzlich bei allen bedanken, die mich bei der Arbeit in den letzten drei Jahren unterstützt haben. Ohne die perfekten wissenschaftlichen Bedingungen und die freundschaftliche Atmosphäre am Max-Planck-Institut wäre die Arbeit nicht möglich gewesen. Insbesondere möchte ich danken:

Prof. Dr. Dietrich Hesse für die unkomplizierte und sofortige Bereitschaft meine Arbeit zu betreuen, sowie für die sorgfältige und gründliche Auseinandersetzung mit der Dissertation.

Dr. Ionela Vrejoiu for the excellent direct supervision of my thesis, for giving me the exciting BFO as topic of my research, and for giving me the opportunity to present my work on many international conferences. Moreover, I wish you all the best for the upcoming new and for sure joyful challenges.

Dr. Daniel Biggemann, Dr. Miryam Arredondo, Dr. Hakan Deniz and Dr. Eckhard Pippel for acquiring many TEM images of my films. Lorenz Bießmann für seinen hilfreichen Beitrag sowie seine Geduld und Motivation bei etlichen Ätzversuchen während seines Praktiums hier am MPI. Eleftherios Andritsos for help in the preparation of substrates during his stay at the MPI.

Dr. Marin Alexe für die Hilfe bei technischen Fragestellungen und Messungen im elektronischen Labor.

My office colleagues: Dr. Daniel Pantel für die geduldige und gute Einführung in mehrere Geräte, seine Hilfsbereitschaft und die sehr hilfreichen wissenschaftlichen Diskussionen. Dr. Alessio Morelli for many discussions and help about BFO, PFM and the AFM, for his sense of humor which helped taking things more lightly, and for teaching me several Italian cusses.

Norbert Schammelt für seine schnellen Lösungen bei Problemen im PLD Labor sowie die Präparation einiger TEM-Proben mittels FIB. Mareike Hermann und Martin Gottschalk für die Präparation einiger TEM-Proben. Julia Ducke und Dr. Jochen Barthel für die Beschaffung mehrerer Publikationen. Den Mitarbeitern der mechanischen Werkstatt für die Herstellung verschiedener Bauteile. Und natürlich

List of Publications

1   F. Johann, Y. J. Ying, T. Jungk, Á. Hoffmann, C. L. Sones, R. W. Eason, S. Mailis, and E. Soergel, *"Depth resolution of piezoresponse force microscopy"*, Appl. Phys. Lett. **94**, 172904 (2009)

2   F. Johann, T. Jungk, S. Lisinski, Á. Hoffmann, L. Ratke, E. Soergel, *"Sol-gel derived ferro-electric nanoparticles investigated by piezoresponse force microscopy"*, Appl. Phys. Lett. **95**, 202901 (2009)

3   F. Johann and E. Soergel, *"Quantitative Measurement of the Surface Charge Density"*, Appl. Phys. Lett. **95**, 232906 (2009)

4   C. Y. J. Ying, C. L. Sones, A. C. Peacock, F. Johann, E. Soergel, R. W. Eason, M. N. Zervas, and S. Mailis *"Ultra-smooth lithium niobate single crystal photonic micro-structures"*, Optics Express **11**, 11508 (2010)

5   F. Johann, Á. Hoffmann, E. Soergel, *"Impact of electrostatic forces in contact-mode scanning force microscopy"*, Phys. Rev. B **81**, 094109 (2010)

6   F. Johann, T. Jungk, M. Lilienblum, Á Hoffmann, and E. Soergel, *"Lateral signals in piezore-sponse force microscopy at domain boundaries of ferroelectric crystals"*, Appl. Phys. Lett. **97**, 102902 (2010)

7   F. Johann, A. Morelli, D. Biggemann, M. Arredondo, and I. Vrejoiu, *"Epitaxial strain and electric boundary condition effects on the structural and ferroelectric properties of $BiFeO_3$ films"*, Phys. Rev. B **84**, 094105 (2011)

8   F. Johann, A. Morelli, and I. Vrejoiu, *"Epitaxial $BiFeO_3$ nanostructures fabricated by differ-ential etching of $BiFeO_3$ films"*, Appl. Phys. Lett. **99**, 082904 (2011)

9   A. Morelli, F. Johann, N. Schammelt and I. Vrejoiu, *"Ferroelectric nanostructures fabricated by focused-ion-beam milling in epitaxial $BiFeO_3$ thin films"*, Nanotechnology **22**, 265303 (2011)

10 I. Vrejoiu, A. Morelli, F. Johann, and D. Biggemann, *"Ordered 180° ferroelectric domains in epitaxial submicron structures"*, Appl. Phys. Lett. **99**, 082906 (2011)

11 F. Johann, A. Morelli, and I. Vrejoiu, *"Stability of 71° stripe domains in epitaxial $BiFeO_3$ films upon repeated electrical switching"*, Phys. Status Solidi B, DOI: 10.1002/pssb.201248329

Curriculum vitae

Name	Florian Johann
Date of birth	December 21, 1982
Place of birth	Kirchheimbolanden, Germany
Nationality	German
Civil status	Single

Education

Period	Institution
08/1993 – 02/1994	**Secondary school Eltville, Germany**
02/1994 – 03/2002	**Secondary school Dierdorf, Germany**
	Degree: "Allgemeine Hochschulreife"
04/2002 – 01/2003	**Alternative civilian service**
	LVA Nordseeklinik Borkum, Germany
04/2003 – 06/2009	**University of Bonn, Germany**
	Degree: "Diplom-Physiker"
08/2006 – 05/2007	**NTNU Trondheim, Norway**
	Erasmus exchange program
06/2009 – 09/2009	**University of Bonn, Germany**
	Research assistant
from 11/2009	**Martin-Luther-Universität Halle-Wittenberg**
	Halle(Saale), Germany
	PhD student at the
	Max Planck Institute of Microstructure Physics

Halle an der Saale, Oktober 2012 Florian Johann

Eidesstattliche Erklärung

Hiermit erkläre ich eidesstattlich, dass ich meine Dissertation selbständig und ohne fremde Hilfe verfasst und keine anderen als die von mir angegebenen Quellen und Hilfsmittel zur Erstellung meiner Dissertation verwendet habe. Die wörtlich und inhaltlich entnommenen Stellen habe ich als solche gekennzeichnet und den entnommen Werken zugeordnet. Die Arbeit ist in vorliegender oder ähnlicher Form bei keiner anderen Prüfungsbehörde zur Erlangung eines Doktorgrades eingereicht worden.

Halle an der Saale, Oktober 2012   Florian Johann